UNIVERSITY OF CALIFORNIA SAN DIEGO

Physics and Applications of Plasmonic Exceptional Points

A dissertation submitted in partial satisfaction of the

requirements for the degree of Doctor of Philosophy

in

Electrical Engineering (Photonics)

by

Junhee Park

Committee in charge:

Professor Boubacar Kanté, Chair
Professor Richard Averitt
Professor Yeshaiahu Fainman
Professor Eric Fullerton
Professor Yu-Hwa Lo

2020

The Dissertation of Junhee Park is approved, and is acceptable in quality and form for publication on microfilm and electronically:

_____

_____

_____

_____

_____

Chair

University of California San Diego

2020

DEDICATION

To my family

TABLE OF CONTENTS

LIST OF FIGURES

ACKNOWLEDGEMENTS

I would like to thank my advisor Prof. Boubacar Kanté for his guidance, support, enthusiasm, and advice, for making things possible and the opportunity to get valuable input at numerous conferences and meetings. I could not complete my doctoral work without his support. I would also like to thank my dissertation committee members, Prof. Richard Averitt. Prof. Shaya Fainman, Prof. Eric Fullerton, and Prof. Yu-Hwa Lo for their time, interest, and valuable comments.

I am grateful to all my colleagues, Ashok Kodigala, LiYi Hsu, Babak Bahari, Wanwoo Noh, Jeongho Ha, Zehtao Jia, Rushin Contractor, Mutasem Odeh, Ricardo Tellez-Limon, Matthieu Dupré, Hadiseh Nasari, Quynh LeVan, and Kevin Han for their help and discussion. Thanks to Abdoulaye Ndao for the excellent teamwork in the plasmonic exceptional point project and for many valuable discussions and encouragement. Thanks to Wei Cai for everything concerned with biosensing. I would also like to thank the nano3 staff for their help in the cleanroom. A special thanks to Maribel for the electron beam lithography of the plasmonic samples.

I would like to say thanks to my friends, Dongwon Park, Namsuk Park, Woojin Choi, Hongseok Oh, Yikyung Yu, Taewoo Kim, and KGSA-UCSD, for their moral and emotional support to complete my doctoral work. Most of all, I would like to express my thanks to my family, Jiyeon Lee, Yeonjun Klay Park, and my parents, for their unconditional love and support. My life and doctoral studies would not have been ever started without their devotion.

Chapter 2, in part, is a reprinted of the materials as it appears in J.-H. Park, A. Kodigala, A. Ndao, and B. Kanté “Hybridized Metamaterial Platform for Nano-Scale Sensing”, *Opt. Express*, **25**, 15590 (2017). This work was co-authored by the dissertation author was the primary researcher and author of this paper.

Chapter 3, in part, is a reprinted of the materials as it appears in J.-H. Park, A. Kodigala, A. Ndao, and B. Kanté "Hybridized Metamaterial Platform for Nano-Scale Sensing", *Opt. Express*, **25**, 15590 (2017). This work was co-authored by the dissertation author was the primary researcher and author of this paper.

Chapter 4, in part, is a reprinted of the materials as it appears in J.-H. Park, A. Kodigala, A. Ndao, and B. Kanté "Hybridized Metamaterial Platform for Nano-Scale Sensing", *Opt. Express*, **25**, 15590 (2017). This work was co-authored by the dissertation author was the primary researcher and author of this paper.

Chapter 5, in part, is a reprinted of the materials as it appears in J.-H. Park, A. Ndao, W. Cai, L.Y. Hsu, A. Kodigala, T. Lepetit, Y.-H. Lo, and B. Kanté, "Symmetry-breaking-induced plasmonic exceptional points and nanoscale sensing", *Nat. Phys*, **16**, 462 (2020). This work was co-authored by the dissertation author was the primary researcher and author of this paper.

Chapter 6, in part, is a reprinted of the materials as it appears in J.-H. Park, A. Ndao, W. Cai, L.Y. Hsu, A. Kodigala, T. Lepetit, Y.-H. Lo, and B. Kanté, "Symmetry-breaking-induced plasmonic exceptional points and nanoscale sensing", *Nat. Phys*, **16**, 462 (2020). This work was co-authored by the dissertation author was the primary researcher and author of this paper.

VITA

2020 Ph.D. Electrical Engineering (Photonics)

University of California San Diego, La Jolla, CA

Dissertation: Physics and Applications of Plasmonic Exceptional Points

Advisor: Professor Boubacar Kanté

2011 M.S. Electrical and Computer Engineering

University of Seoul, Seoul, Korea (ROK)

2009 B.S. Electrical and Computer Engineering

University of Seoul, Seoul, Korea (ROK)

PUBLICATIONS

R. Tellez-Limon, B. Bahari, L.Y. Hsu, **J.-H. Park**, A. Kodigala, and B. Kanté, "Integrated metaphotonics: symmetries and confined excitation of LSP resonances in a single metallic nanoparticle", *Opt. Express*, **24**, 15590 (2016).

J.-H. Park, A. Kodigala, A. Ndao, and B. Kanté, "Hybridized Metamaterial Platform for Nano-Scale Sensing", *Opt. Express*, **25**, 15590 (2017).

J. Ha, A. Ndao, L.Y. Hsu, **J.-H. Park**, and B. Kanté, "Planar dielectric cylindrical lens at 800 nm and the role of fabrication imperfections", *Opt. Express*, **26**, 23178 (2018).

J.-H. Park*, A. Ndao*, W. Cai, L.Y. Hsu, A. Kodigala, T. Lepetit, Y.-H. Lo, and B. Kanté, "Symmetry-breaking-induced plasmonic exceptional points and nanoscale sensing", *Nat. Phys*, **16**, 462 (2020). *Contributed Equally

A. Ndao*, L.Y. Hsu*, J. Ha, **J.-H. Park**, C. Chang-Hasnain, and B. Kanté "Octave bandwidth photonic fishnet-achromatic-metalens", *Nat. Commun.*, **11**, 3205 (2020). *Contributed Equally

A. Ndao, L.Y. Hsu, W. Cai, J. Ha, **J.-H. Park**, Y.-H. Lo, and B. Kanté "Differentiating and quantifying exosomes secretion from a single cell using quasi-bound states in the continuum", *Nanophotonics*, 9, 1081 (2020).

ABSTRACT OF DISSERTATION

Physics and Applications of Plasmonic Exceptional Points

by

Junhee Park

Doctor of Philosophy in Electrical Engineering (Photonics)

University of California San Diego, 2020

.
Professor Boubacar Kanté, Chair

This dissertation provides a comprehensive study of non-Hermitian systems and applications. The coupling phenomena occur in three-dimensional plasmonic nanostructure lead to a peculiar spectral response. Modification of near-field coupling in nanorod pairs enables to invert plasmon hybridization scheme, which offers engineering resonance. The first half of this dissertation investigates the optical properties of the plasmon hybridization system based on the multilayered structure. The proposed hybridized sensing platforms can improve sensing capabilities than a standard single plasmonic resonance system.

In the second half of this dissertation, we propose a novel approach to exceptional points (EPs) where eigenvalues and eigenvectors coalesce simultaneously. The plasmonic EPs are based on the hybridization of detuned resonances in multilayered plasmonic structures to reach a critical

complex coupling rate between nanoantenna arrays, resulting in the simultaneous coalescence of the resonances and loss rates. The hybridization of optically dissimilar resonators, however, led to two-hybrid modes with crossing and avoided crossing of both the resonances and loss rates, unambiguously demonstrating the existence of a plasmonic EP where resonances and loss rates become simultaneously degenerate. By breaking the symmetry (that is, making the bars optically different) the hybridized modes are no longer purely symmetric or anti-symmetric, making interference via radiation possible. Therefore, the interplay between near-field Coulomb interactions (mostly controlled by d_x) and radiative coupling via interferences (enabled by symmetry breaking and mostly controlled by P_y) enables the coalescence of the hybrid modes, i.e., lead to the existence of EP. The exceptional points are used as sensors of anti-immunoglobulin G, the most abundant immunoglobulin isotype in human serum. We demonstrated, for the first time, a new type of sensors that are 267 more sensitive than the current states of the art of nanosensors.

CHAPTER 1: INTRODUCTION

1.1 Motivation

In 1902, since the first observations variations of intensity in the reflection and transmission spectra of white light diffracted by a metalized grating by Wood [1], [2]. He noticed a surprising phenomenon: “I was astounded to find that under certain conditions, the drop from maximum illumination to a minimum, a drop certainly of from 10 to 1, occurred within a range of wavelengths not greater than the distance between the sodium lines”. The first theoretical treatment of these anomalies was by Lord Rayleigh in 1907 [3]. He based his "dynamical theory of the grating" on an expansion of the scattered electromagnetic field in terms of outgoing waves only. With this assumption, he found that the scattered field was singular at wavelengths for which one of the spectral orders emerged from the grating at the grazing angle.

In the same context, in 1941, U. Fano presented a first vector explanation of the diffraction phenomenon and introduces the concept of surface waves propagating on the surface of metallic gratings [4]. It was only in 1957 that Ritchie [5] first spoke of a surface plasmon and showed the possibility of guiding light along with an interface between a metal and a dielectric. In 1968, optical excitation of surface plasmons by means of attenuated total reflection was demonstrated using two different methods [4], [5]. These two methods were developed in parallel by A. Otto [4] on the one hand and E. Kretschmann and H. Raether on the other.

Since then, surface plasmons studies in periodic structure continues to fascinate the scientific world. The physical understanding of the influence of geometry and dielectric environments, in a broad and general sense, has led to a new paradigm in plasmonics – plasmon hybridization [6]. The plasmons of many non-trivial nanostructures can be understood as the interaction of simpler coupled plasmons. The plasmon hybridization paradigm, in addition to

advancing our understanding of the basic physics of nanostructure plasmons, has become a design tool for designing nanostructures with plasmons for specific applications. Moreover, recent advances made in photonics, both in understanding physical phenomena and in the control of fabrication processes, have contributed to improved detection capabilities in terms of, high stability, and miniaturization of interfaces or system integration. In this thesis, we will explore new types of plasmonic systems that can enhance sensitivity.

1.2 Dissertation Outline

In this dissertation, plasmonic exceptional points are proposed, fabricated, and characterized using a hybridized plasmonic nanostructure platform. In Chapter 2, we show the fundamental investigation of plasmonic arrays and their properties. We also show a simple and intuitive method, namely, plasmon hybridization for understanding the optical properties of coupled plasmonic nanostructures. In Chapter 3, we present the fabrication recipes of three-dimensional plasmonic nanostructure using a multilayer technique. Especially, we introduce a fabrication process employing polymer planarization, precise alignment, stacking. Chapter 4, we investigate the sensing capabilities of the hybridized platform with details on numerical simulation and experimental characterization. Magnetic dipolar modes in hybridized systems exhibit four-fold improved resolution sensing performance.

In Chapter 5, first, we introduce the non-Hermitian singularities exceptional points (EPs) where both eigenvalues and eigenstates coalesce. We investigate a symmetry-dependent hybridization structure to implement plasmonic EPs. The mode identification and engineering of optical loss in the non-Hermitian plasmonic system are studied to reach EPs. Subsequently, the breaking-symmetry induced EP in the plasmonic hybridization platform is experimentally

demonstrated. In Chapter 6, we investigate the enhanced sensitivity of plasmonic EP sensors compared to conventional plasmonic sensors. The EP sensor shows square-rood dependence on the refractive index variation in the cladding layer. This validates the existence of EP in plasmonic systems. Anti-immunoglobulin G, the most abundant immunoglobulin isotype in human serum, is evaluated in EP sensors. An attomolar level concentration of anti-IgG detection is performed using EP sensors. Finally, in Chapter 7, we summarize the significant contribution of this work and discuss the future research direction.

CHAPTER 2: Coupling in Plasmonic Nanostructure

2.1 Introduction

In this chapter, we will introduce the coupling effect of the plasmonic nanostructure. The unique optical properties of plasmon resonant nanostructure are determined by the collective oscillations of their conduction electrons. Surface plasmons are electromagnetic modes trapped on a metal-dielectric interface. In contrast, non-propagating surface plasmons usually referred to localized plasmons, which can be excited in subwavelength scales.

The plasmonic nanostructure can be coupled via their near-field when particles are located close to each other and whose distance is substantially lower than the plasmon resonance wavelength of the nanostructures. It has been experimentally demonstrated by previous works, plasmon hybridization [6] such as stacked dimer [7], [8], ring-disk dimer structures [9]–[11], plasmonic oligomers [12]–[14], and hybrid material dimers [15]. All near-field coupled plasmonic structures have in common that the fundamental localized plasmon resonance is shifted or hybridized due to the interaction of particles.

This chapter includes an analysis of simple plasmonic nanorod array and the complex coupled plasmonic structure such as nanorod pairs. The coupling strength is investigated in the plasmon hybridization configuration with various geometrical parameters.

2.2 Numerical Method

Numerical simulations are performed using commercial software package CST Microwave Studio [16] to calculate the complex scattering parameters of the periodic structure. CST Microwave Studio is a general-purpose electromagnetic simulator based on the Finite Element

Method (FEM). This numerical method provides a universal scheme, application to various electromagnetic problem ranging from static, low to high frequency applications in frequency

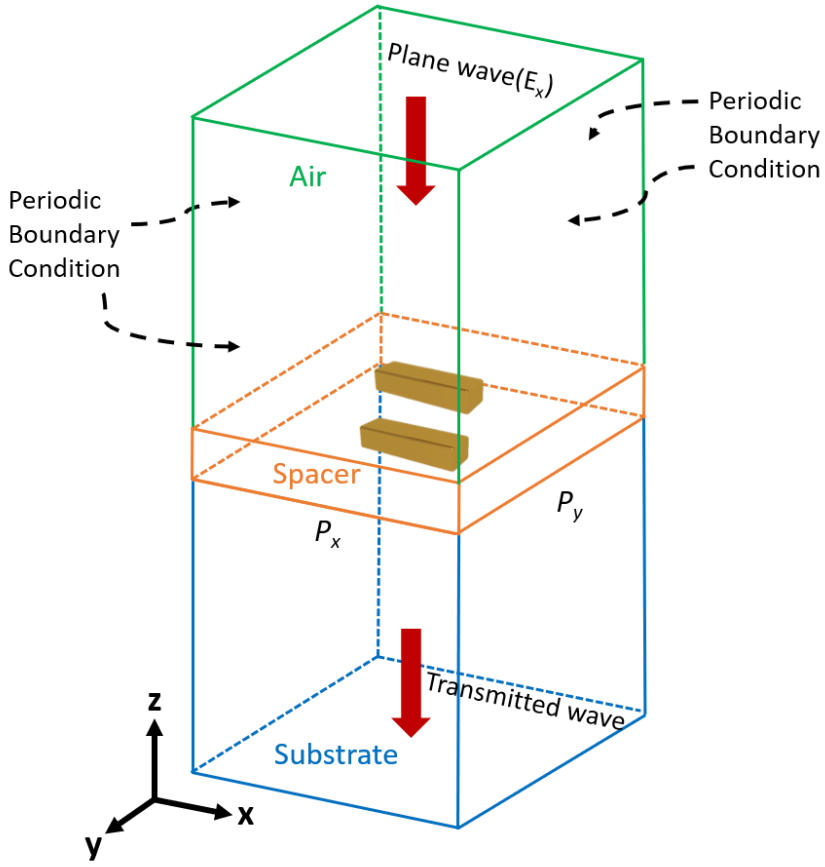

Figure 2.1 Schematic of the unit-cell of hybridized plasmonic resonators with periodic boundary conditions in the XY plane. The system is infinite in the XY plane and made of two metallic resonators in the Z direction.

domain. The frequency-domain solver is a powerful multi-purpose 3D full-wave solver that offers excellent simulation performance for many types of components such as high-frequency applications using small-to-medium-sized models and resonant structure at subwavelength scale.

The periodic systems are modeled using unit-cells with periodic boundary conditions in Figure 2.1. The system in a metallo-dielectric photonic crystal (plasmonic crystal), infinite in the XY plane and made of two metallic layers in the Z-direction (thus, finite in Z-direction). In the

propagation direction, the unit-cell has open boundary conditions and is terminated with input and output ports. The input and output ports are excited with a plane wave, and polarization is defined. The amplitude and the phase of the transmitted and reflected waves are calculated after propagation through unit-cell. The permittivity of the composed materials of the metallo-dielectric elements is assigned individually. Electric (*E*) and magnetic (*H*) field distributions can be obtained during scattering parameter simulation. The permittivity of gold in the infrared spectral regime is described using a Drude model [17]:

$$\varepsilon(\omega) = 1 - \frac{\omega_p^2}{\omega(\omega + i\omega_c)} \quad (1)$$

with a plasma frequency $\omega_p = 1.367 \times 10^{16}$ [rad/s] and a collision frequency $\omega_c = 6.478 \times 10^{13}$ [rad/s]. The optical parameters were refractive index of SU-8 $n_{SU\text{-}8} = 1.57$ and the SiO_2 substrate refractive index $n_{SiO2} = 1.50$.

2.3 Plasmonic Array

Figure 2.2 shows a schematic of a unit-cell of a gold nanorod on the SiO_2 substrate. The fundamental geometry parameters, a nanorod with a length (*L*), a width (*W*) and a thickness (*t*) are considered to investigate resonant plasmonic modes at the different spectral position. The geometry parameters can be controlled during the fabrication process, and modeling can be used to select target geometries that will resonate at the desired frequency. The incident electromagnetic waves are polarized in X-direction along the nanorod. The system is infinite in the XY plane, and P_x and P_y indicate the periodicity of each direction, respectively. The resonant plasmonic mode can be tuned to the visible and near-infrared regime with wavelengths between 500 to 2000 nm with a nanorod length variation.

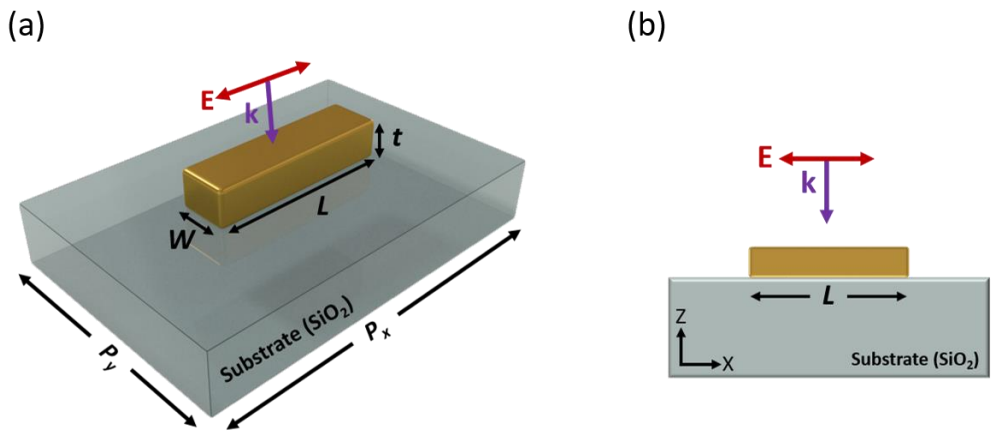

Figure 2.2 Schematic of a unit-cell of a gold nanorod on SiO_2 substrate. (a) Geometrical parameters: nanorod width (W), length (L), and thickness (t). The system is infinite in the XY plane, and P_x and P_y indicate the periodicity of each direction, respectively. (b) Cross-section view of the unit-cell of a gold nanorod.

Figure 2.3 shows the calculated transmission spectra in changing the fundamental geometric parameters of a nanorod. An increase in the length of a nanorod shifts the resonance to low frequency (redshift), as seen in Figure 2.3 (a). A resonance can be observed at around 160 THz (W = 50 nm, L = 500 nm, t = 40 nm) in the spectrum (yellow line) in Figure 2.3 (b). This resonance is the excitation of an electric dipole moment in the nanorod extending from the negative to the positive charges along the longer axis. The width variation for fixed length and thickness of a nanorod shifts resonant plasmonic mode to high frequency (blueshift) in Figure 2.3 (c). As the aspect ratio (L/W) of a nanorod is increased, the longitudinal resonance is redshifted [18]. The spectral broadening of the localized surface plasmon resonance mode is observed. For the width of 60 nm and below, the shifts are pronounced than the width of 100 nm and wider, as shown in Figure 2.3 (d). The thickness varied, keeping the length and width of a nanorod fixed at 450 nm and 50 nm, respectively. Increasing the thickness leads to a very pronounced blueshift due to the top and bottom plasmons decoupling for large thickness, as seen in Figure 2.3 (e), accompanied by a strong increase of the spectral width. The thickness of 20 nm (blue line) and 90 nm (purple

line) shows very different spectral linewidth. For the higher thicknesses, the plasmon resonance shifts become smaller, and the plasmon resonance approached a limiting value. In addition, the

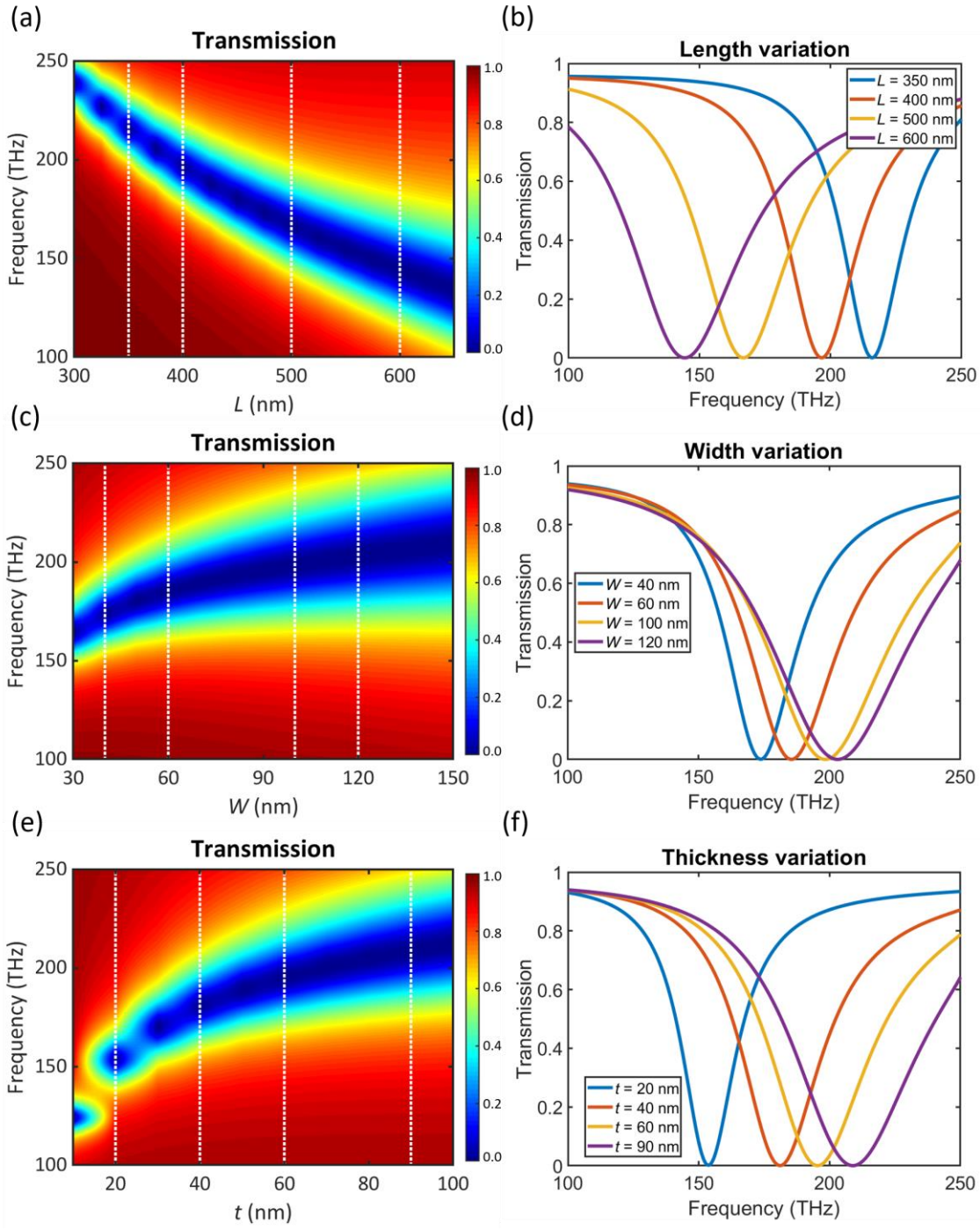

Figure 2.3 Transmission spectra for different parameters, lengths (*L*), widths (*W*), and thicknesses (*t*). (a) Variation of *W* for fixed *L* = 450 nm, *t* = 40 nm. (c) Variation of *L* for fixed *W* = 50 nm, *t* = 40 nm. (e) Variation of *t* for fixed *W* = 50 nm, *L* = 450 nm.

plasmon modes are dominated by the dipole mode of the surface charges; those are well distributed on the surface of the nanorod [19]. The surface charges are not strongly confined. For the smaller thickness, the resonance includes higher modes along with the dipole mode.

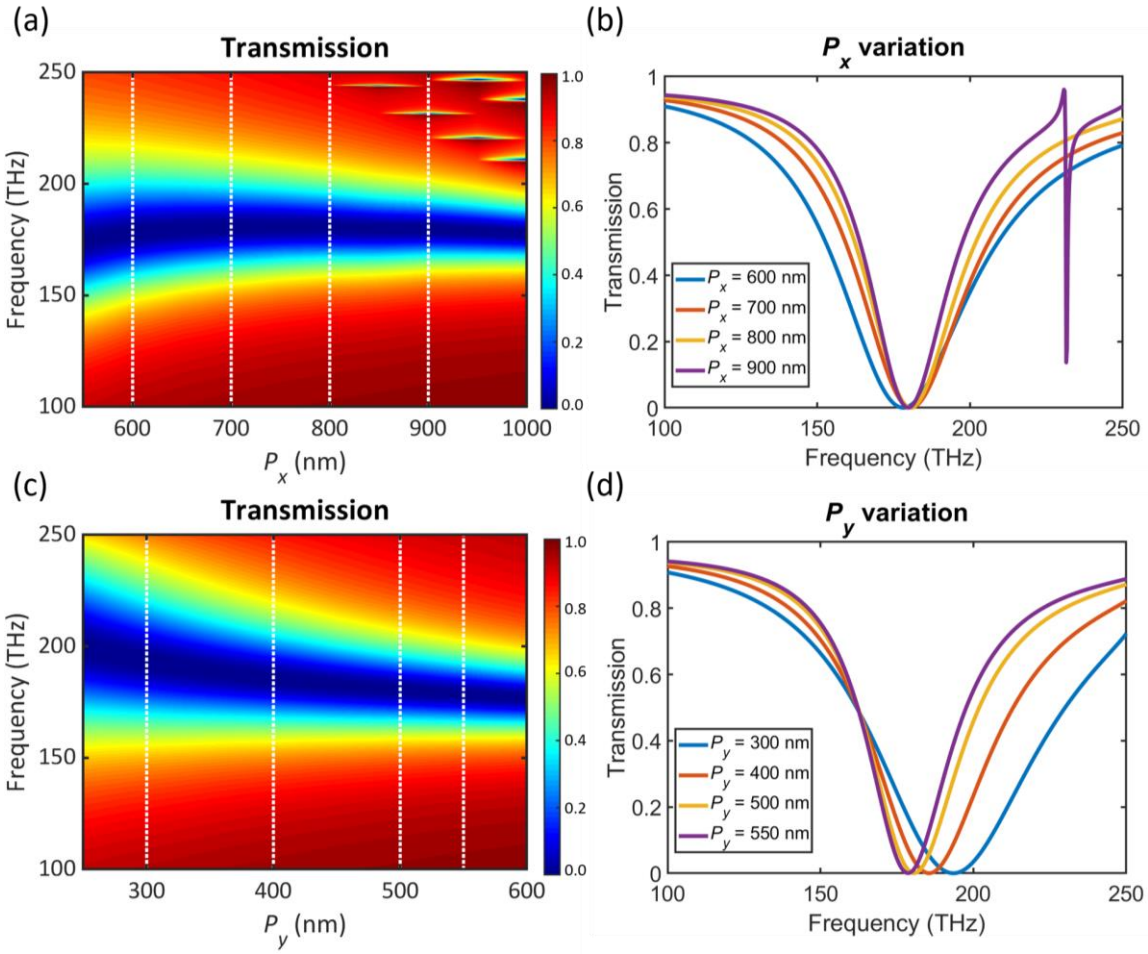

Figure 2.4 Calculated transmission of different periodicities for each direction, P_x and P_y. (a) Variation of P_x for fixed L = 450 nm, W = 50 nm, t = 40 nm, and P_y = 500 nm. (c) Variation of P_y for fixed L = 450 nm, W = 50 nm, t = 40 nm, and P_x = 800 nm. The spectra in (a), (c) correspond to vertical cross-sections of the color plot in (b), (d) indicated by dashed white lines, respectively.

The effect of tuning the unit-cell periods in X- and Y-direction is investigated below. Figure 2.4 shows the calculated transmission spectra for each period variation, P_x and P_y, for fixed geometry parameters, L = 450 nm, W = 50 nm, and t = 40 nm, respectively. Change in the period in x-direction does not affect the spectral position of resonances unless the distance between two nanorods is less than 150 nm, P_x = 600 nm. In contrast, the change in the period in Y-direction has a significant effect on the system's resonance. By tuning P_y from 250 nm to 600 nm, the resonance frequency shifts to the low frequency, which means redshift. This phenomenon can be explained by dipolar radiative coupling between the nanorods [20], as illustrated in Figure 2.5. When the nanorods form an array, they will couple with each other through the dipolar radiative interaction, leading to significant spectral shifts of the plasmonic resonances. Thus, in rectangle arrays, the resonant plasmonic modes depend only on one dimension. The radiative direction is orthogonal to polarization. Therefore, an increase in density in Y-direction means a decrease in P_y gives rise to interaction to neighboring nanorods because most radiation is emitted perpendicular to the nanorod. In contrast, due to the charge oscillation direction (X-direction), the variation of P_x will not have radiative coupling between nanorods.

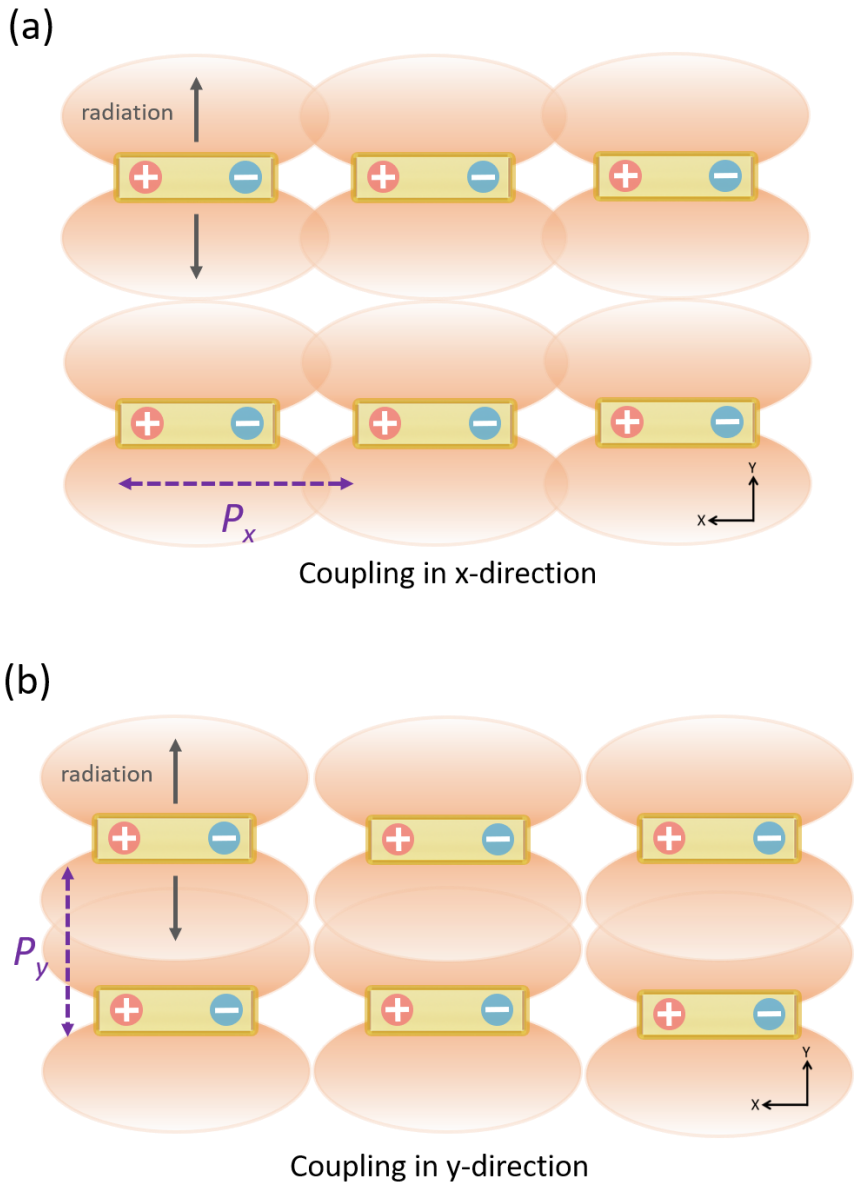

Figure 2.5 The dipole radiative coupling between the nanorods. The electromagnetic fields related to the localized surface plasmon mode of one nanorod act to influence the response of neighboring nanorods. (a) Coupling in x-direction changing in P_x (b) Coupling in y-direction changing in P_y.

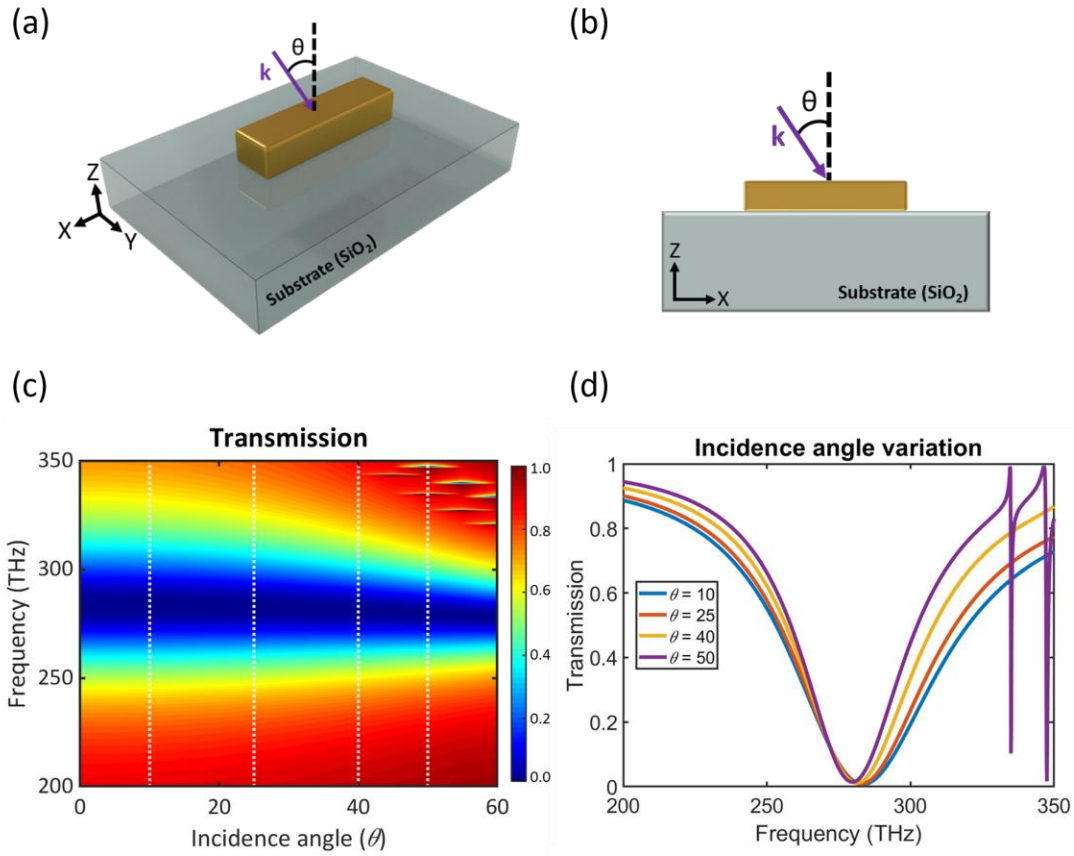

Figure 2.6 Schematic setup with incidence angle (θ) and calculated transmission of incidence angle variation. (a) Unit-cell with incidence angle (b) Cross-section view, (c) Simulated results of transmission spectra. The spectra in (c) correspond to vertical cross-sections of the color plot in (d) indicated by dashed white lines.

Optical characterizations allow us to control the properties of the incident light. Here, the resonance behavior on the incidence angle of light (θ) is investigated for fixed geometry parameters, L = 250 nm, W = 50 nm, t = 40 nm, and $P_x = P_y$ = 400 nm. Figure 2.6 (a, b) shows the schematic illustration with the incidence angle. For an incidence angle of less than 40°, no significant changes in resonance are observed in Figure 2.6 (c). An increase in the incidence angle leads to narrow the linewidth of resonance. For an incidence angle of more than 50°, one relatively broad appearing at the frequency of 280 THz, and another narrow dispersive resonance like Wood anomalies [21] are seen in Figure 2.6 (d) at frequencies of 335 THz and 347 THz, respectively.

Another property of incident light is the polarization angle, which can be simply controlled in optical characterization. To explore the effect of polarization angle on nanorods array, the simulation with different polarization angles was performed on the periodic structure with the same parameters as incidence angle investigation. Figure 2.7 (a) shows transmission spectra with varying polarization angle. For the smaller angle, less than 10^{o}, which means that light polarization is parallel with the long axis of the nanorod. For the larger angle, more than 50^{o}, incoming light does not efficiently couple to resonant plasmonic mode. The transmission spectrum at an angle of 70^{o} in Figure 2.7 (b), red line, represents much weaker, and the drop in transmission at the resonance position is 20 % compared to almost 100 % at the angle of 10^{o}. It is worth noting that matching the polarization angle to resonant plasmonic mode is crucial during optical characterization to obtain a strong resonance response.

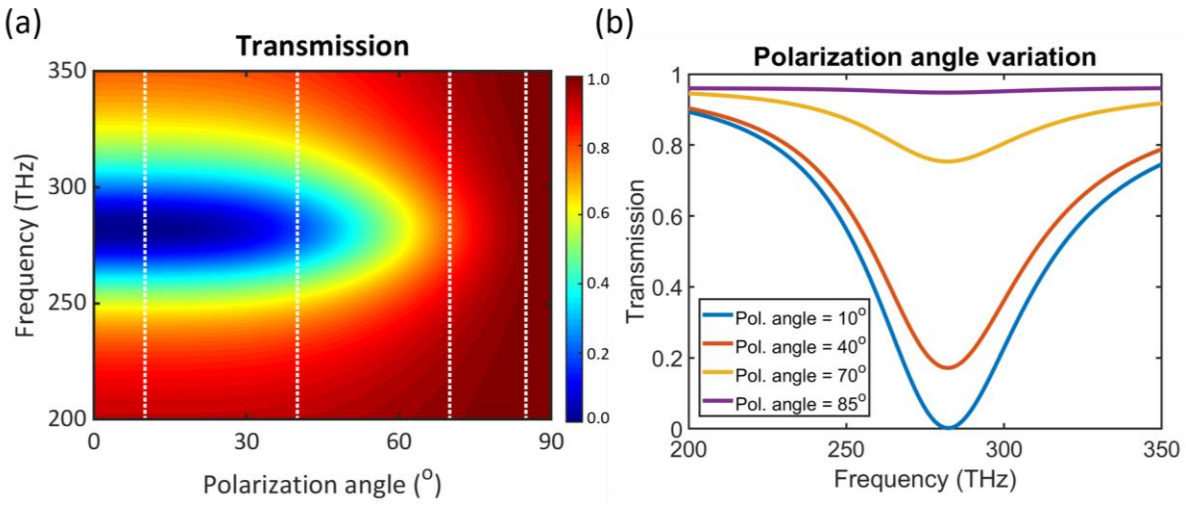

Figure 2.7 Calculated transmission spectra on the difference polarization angle. The spectra in (a) correspond to vertical cross-sections of the color plot in (b) indicated by dashed white lines.

2.4 Plasmon Hybridization

If two or more metallic nanoparticles are placed in proximity to one another, the optical spectra response of the composite structure can be altered. This concept has recently been

described in terms of the hybridization of plasmon modes supported by the individual parts of those structures [22]–[24]. Figure 2.8 depicts the plasmon hybridization scheme for a nanoparticle dimer consisting of two equally sized metallic nanorods. The coupling leads to the lifting of the degeneracy of the plasmonic mode of the individual nanorod and gives rise to two new hybrid modes as a result of plasmon hybridization. One mode shows a symmetric alignment of the two electric dipoles and is termed the symmetric mode, $|\omega_+>$. The charge oscillations inside the two nanorods move in phase. This mode is located at higher energy as the induced dipole moments repel each other. In contrast, the other mode displays an antiparallel alignment of the dipole moments and is referred to as the antisymmetric mode, $|\omega_->$. This mode is lowered in resonance energy due to the attractive interaction between two induced dipole moments in the nanorods. The charge oscillates with a phase shift of 180°. The antisymmetric mode would be an optically dark mode, since the net dipole moment of the plasmons is zero for identical nanorods. Nevertheless,

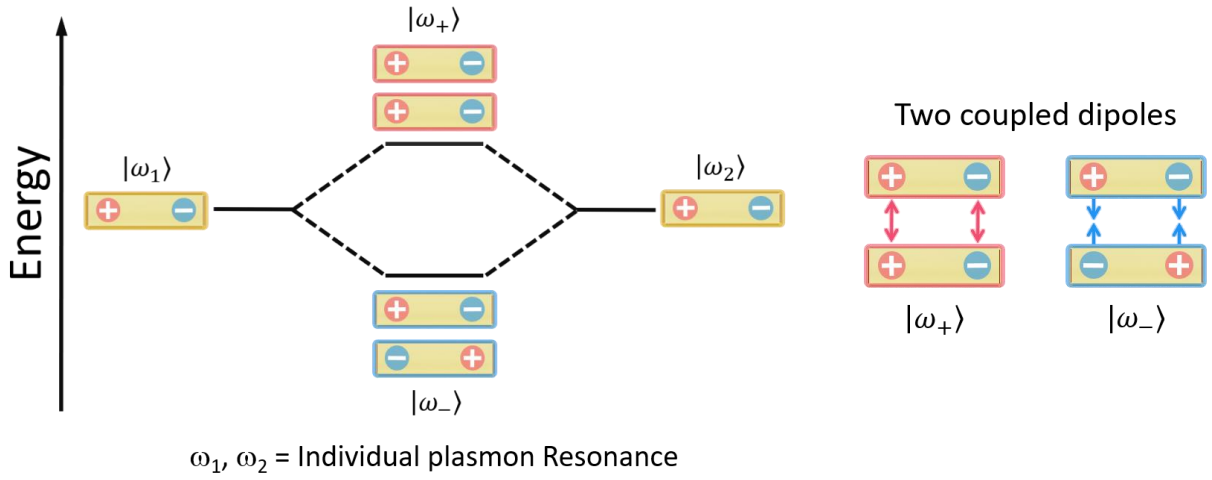

Figure 2.8 Schematic illustration for plasmon hybridization in two coupled nanorods. ω_1 and ω_2 represent individual plasmon resonance.

the system can be excited by an external electromagnetic wave due to the phase retardation effect induced by the spatial variation of the electric field in the propagation direction. In addition, the

antisymmetric mode of the two nanorods in the transverse configuration also exhibits a magnetic moment due to the opposite electric current direction in each nanorod. In this respect, the symmetric mode, $|\omega_+>$, is referred to as electric dipole mode and antisymmetric mode, $|\omega_->$ is referred to magnetic dipole mode giving rise to a magnetic response in the system.

Figure 2.9 displays numerical simulation results of electric current density and the absolute value of the out-of-plane component of the magnetic field distribution in the system. The system consists of two stacked nanorods with a separation of 20 nm, and two nanorods are embedded in the dielectric slab (n_{slab} = 1.4). The opposite current of antisymmetric mode produces a strongly confined magnetic field between two stacked nanorods. On the other hand, the symmetry current charges oscillate in phase, of symmetric mode exhibits a mere magnetic field between nanorods.

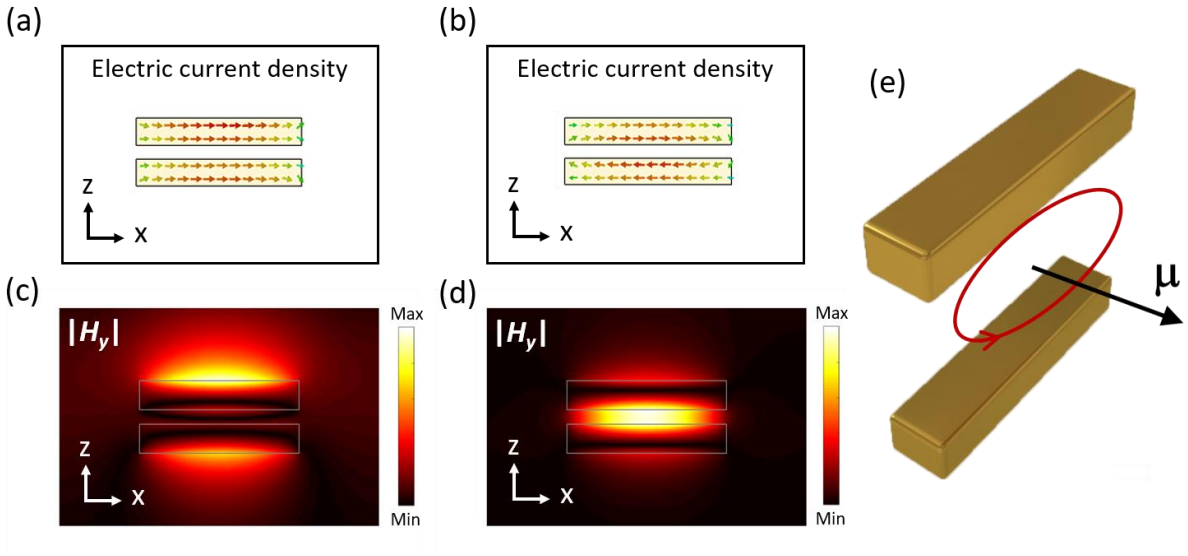

Figure 2.9 Numerical simulation results of the electric current density (a, b) and the absolute value of magnetic field distribution ($|H_y|$) for symmetric (c) and antisymmetric mode (d), respectively. (e) The configuration of two stacked nanorods behaves as a magnetic "atom."

Strongly confined magnetic either on the top or bottom of a nanorod indicate electric dipole modes. The configuration in Figure 2.9 (e) describes the behavior of the magnetic atom in two stacked nanorods [25], [26].

Next, the two stacked nanorods configuration is considered to accomplish the plasmon hybridization scheme in the experiment. The unit-cell of the multilayered structure is introduced in Figure 2.10. The structure consists of two aligned and vertically spaced identical gold nanorod array. A bottom nanorod is fully embedded in dielectric spacer (n_{spacer} = 1.57). The thickness of

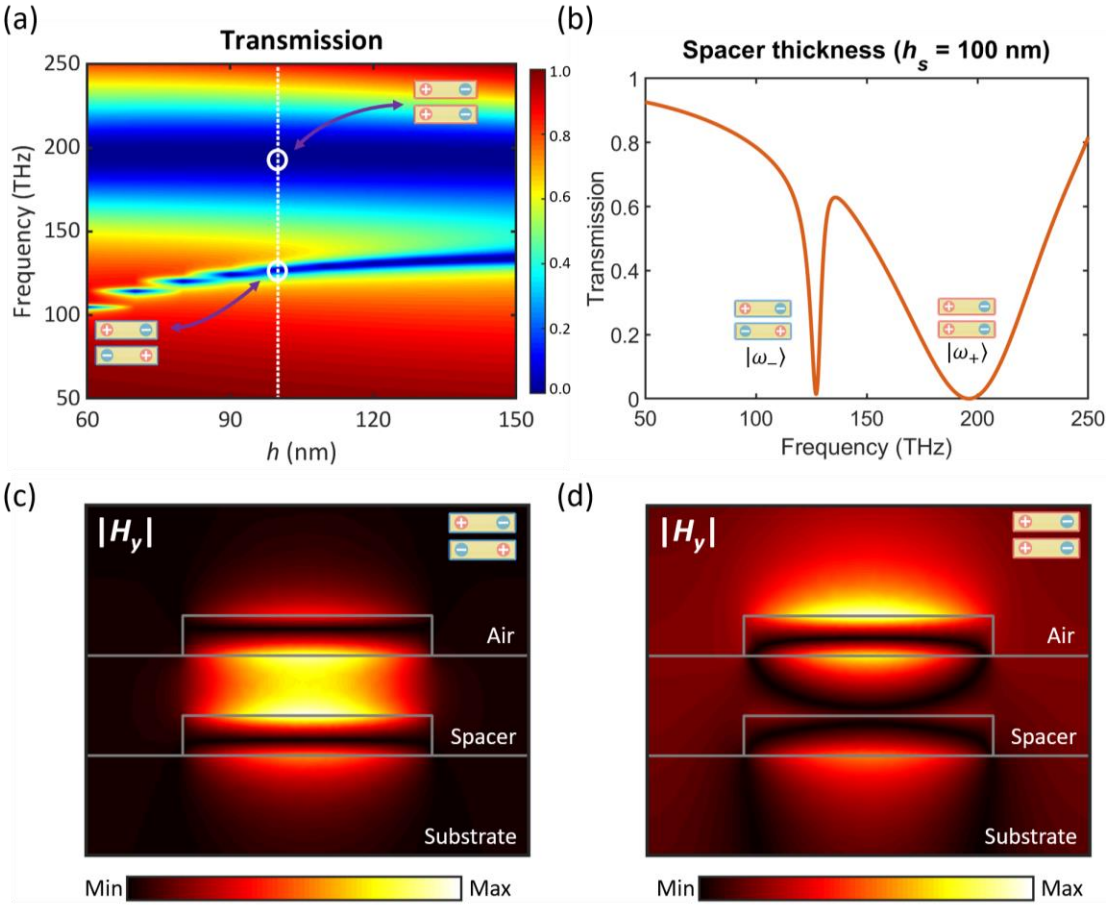

Figure 2.10 Transmission spectra on varying spacer thickness (h_s) and magnetic field distribution. Two pronounced modes are observed. The transmission spectra in (a) correspond to vertical cross-sections of the color plot in (b), h_s = 100 nm indicated by dashed white lines. (c, d) The absolute value of magnetic field distribution ($|H_y|$) for antisymmetric (ω_-) and symmetric (ω_+) modes.

dielectric spacer can be controlled in the fabrication process. The multilayered nanorods structure exhibits a more geometrical degree of freedom than a single nanorod. The incident electromagnetic waves are polarized in X-direction along the nanorods, which excite two nanorods at the same

polarization state. Following the calculation, geometric parameters of the nanorod, L = 450 nm, W = 50 nm, and t = 40 nm are kept in constant, respectively and the size of unit-cell, P_x = 800 nm and P_y = 400 nm are chosen such that near-field interaction between neighboring nanorods is minimized and avoid high-order diffraction.

The near-field interaction in multilayered nanorods structures is investigated in Figure 2. 10. The spectra are displayed depending on the spacer thickness (h_s). Clearly, the multilayered structure exhibits two pronounced resonance (i.e., lifted degeneracy) due to the interaction of the plasmon modes of individual nanorods, as illustrated in Figure 2.8. The near-field induced mode splitting can be clearly understood by plasmon hybridization. One resides at higher frequency with broader spectral linewidth (i.e., electric dipolar resonance), can be identified to be the symmetric mode. The impinging light induces current flow in phase in the two nanorods. In contrast, the other is located at a lower frequency with narrow spectral linewidth (i.e., magnetic dipolar resonance), corresponds to antisymmetric mode. The current flow induced by incoming light exhibits out of phase along two stacked nanorods. Figure 2.10 (b) shows transmission with a spacer thickness of h_s = 100 nm. Hybridized modes are clearly observed in two minimums of transmission. These modes can be simply identified by two different ways, energy level, and spectral linewidth. Figure 2.10 (c, d) displays the calculated the absolute value of magnetic field distribution in the multilayered system at two different spectra positions, 127.7 THz and 205.5 THz, indicated as white circles in the spectra of Figure 2.10 (a). In Figure 2.10 (d), the magnetic field indicates the antisymmetric nature of the plasmon mode. The maximum magnetic field is presented between two nanorods indicating the opposite direction of the induced current flow in two nanorods. In contrast, the magnetic field distribution is dominant on only one nanorod due to the symmetric current flow in nanorods, which indicates electric resonance (i.e., symmetric mode) [22], [27].

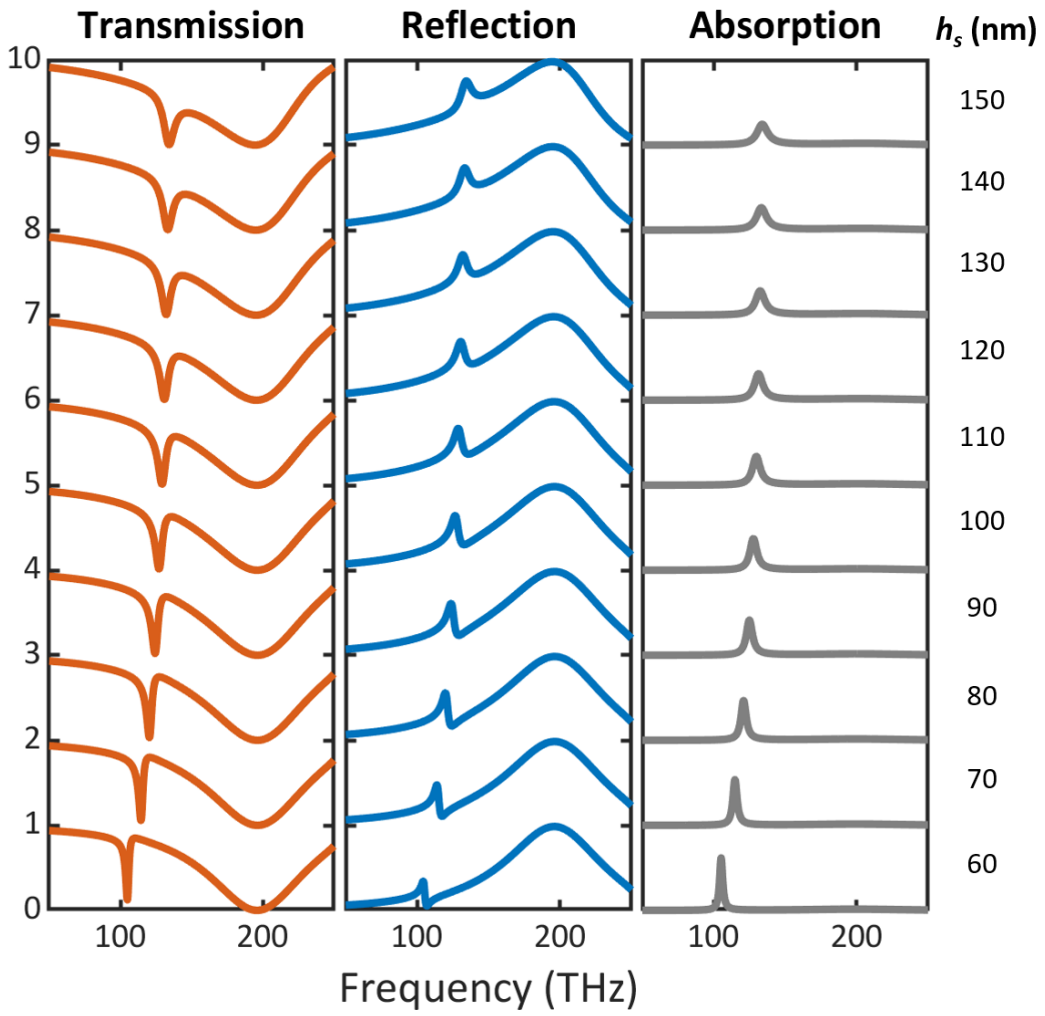

Figure 2.11 Calculated transmission, reflection, and absorption spectra for different spacer thicknesses h_s of the multilayered structure. h_s varies from 60 to 150 nm. The geometric parameters of the identical two nanorods are L = 450 nm, W = 50 nm, and t = 40 nm, and the size of unit-cell is P_x = 800 nm and P_y = 400 nm, respectively.

The influence of near-field coupling is demonstrated in Figure 2. 11 by considering a spacer thickness (h). The calculated transmission and reflection spectra constitute two hybridized modes. The splitting between symmetric and antisymmetric mode increases with a decrease in spacer thickness (h_s) due to a strengthened electrostatic interaction. The antisymmetric mode noticeably shifts to a higher frequency (blueshift) depending on h_s variation, while the frequency shift in the symmetric mode is mere. The spectra position of absorption (A = 1 – T – R) is associated with the

antisymmetric modes, and their shifts in frequency with an increase in h are also observed. The maximum absorption peak is obtained at h_s = 60 nm, due to the strong near-field interaction. The non-radiative nature of the antisymmetric mode, i.e., the suppression of radiative damping, results in a prolonged lifetime (narrow spectral bandwidth) and a pronounced absorption peak.

2.5 Inversion of Plasmon Hybridization in Multilayered Structure

Up to now, the spacer thickness with vertical alignment is only considered in the multilayered structure to control the optical response of hybridized modes. The spectral shifts are strongly dependent on coupling strength between two stacked nanorods. The coupling strength can be controlled by an arrangement of the oscillators with respect to each other. To achieve the relative orientation of the nanorods, a broken structure symmetry is introduced by a lateral shift (d_x) between upper and lower nanorods. Figure 2.12 illustrates the multilayered structure with the displacement of one nanorod by d_x, along the longer axis. Similar works have already been demonstrated by nanowires and pairs of the cut wire. Figure 2.12 displays the influence of symmetry breaking by considering a lateral nanorod displacement. The interchange of spectral positions of two hybridized modes is observed with a continuous increase of lateral displacement. This inversion stems from the near-field coupling. For example, structure with d_x = 0, the near-field interaction between two nanorods is repulsive for the symmetric mode because of parallel current along the interacting stacked nanorods, whereas the attractive force is presented in the antisymmetric mode due to the antiparallel current flow. When the nanorods progressively shift to the lateral direction, the Coulomb interaction between two stacked nanorods is altered, and for enough displacement, d_x = 400 nm in Figure 2.12, the sign of charge interaction changes. As a result, the repulsive (attractive) force becomes attractive (repulsive). This leads to the

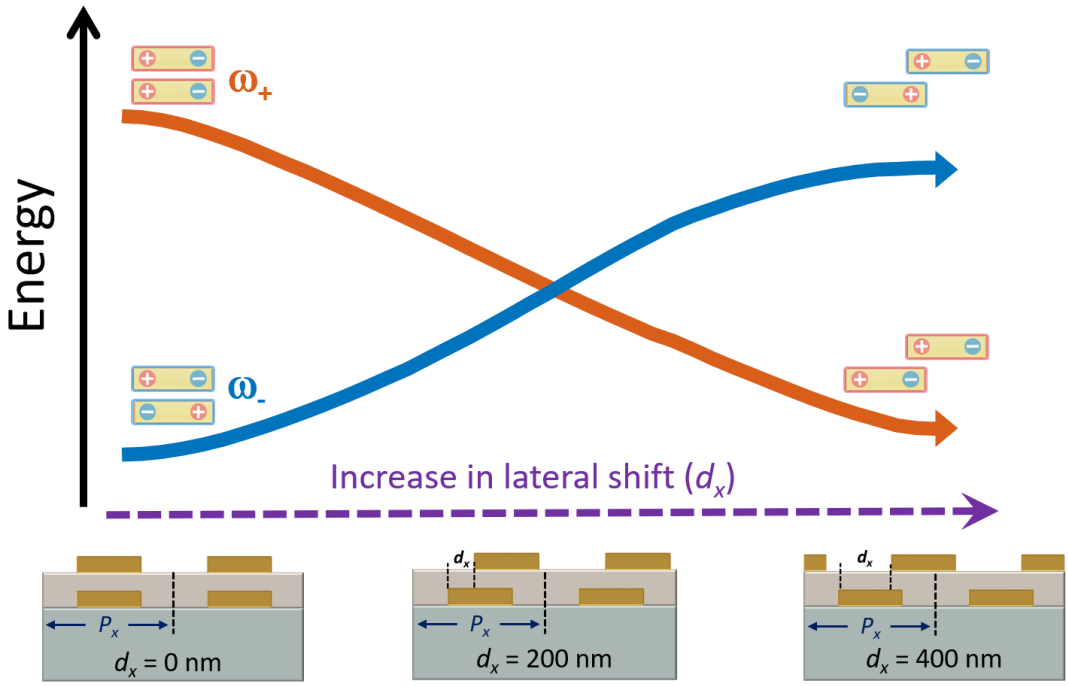

Figure 2.12 Schematic of the hybridized modes inversion with lateral shifts. The energy level is reversed by increasing displacement. Cross-view of multilayered nanorod array presents shifts between upper and lower layers, d_x = 0, 200, 400 nm, respectively.

antisymmetric mode to resides at a higher frequency and vice versa. Therefore, the plasmon hybridization can be reversed by breaking the symmetry of structure [28], [29].

Figure 2.13 displays calculated transmission, reflection, and absorption color maps for multilayered structures with lateral shift (d_x) for different spacer thickness (h_s), 60, 90, 120, and 150 nm, respectively. Calculated results clearly show they hybridized modes in transmission and reflection spectra. The symmetric mode shows the pronounced resonance characteristics, broaden linewidth, in both transmission and reflection. The non-radiative nature of antisymmetric mode is also founded with narrow linewidth in the calculated spectra. The inversion of plasmon

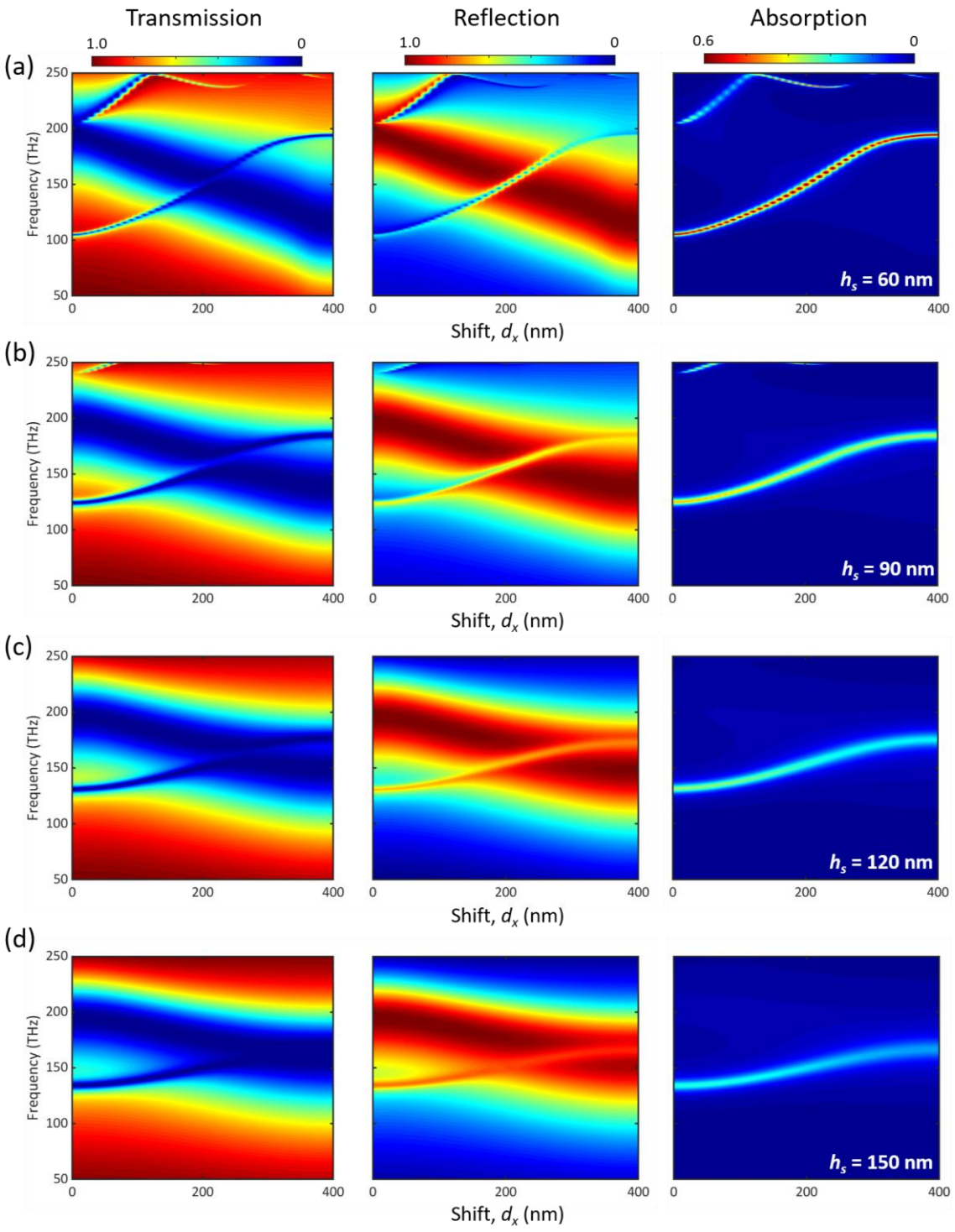

Figure 2.13 Calculated transmission, reflection, and absorption (left to right column) color maps for multilayered structure with increasing lateral displacement (d_x) for different spacer thickness (h_s), (a) 60 nm (b) 90 nm (c) 120 nm and (d) 150 nm, respectively.

hybridization scheme in multilayered nanorods is seen as expected. Absorption peaks are observed in Figure 2.13. The feature of absorption exhibits blueshift to lateral displacement and spectrally narrow linewidth. The maximum peak of absorption is decreased on the lateral shift except for h_s = 60 nm. The near-field coupling between two nanorods becomes weaker when displacing is introduced, and this causes linewidth broadening in absorption as well.

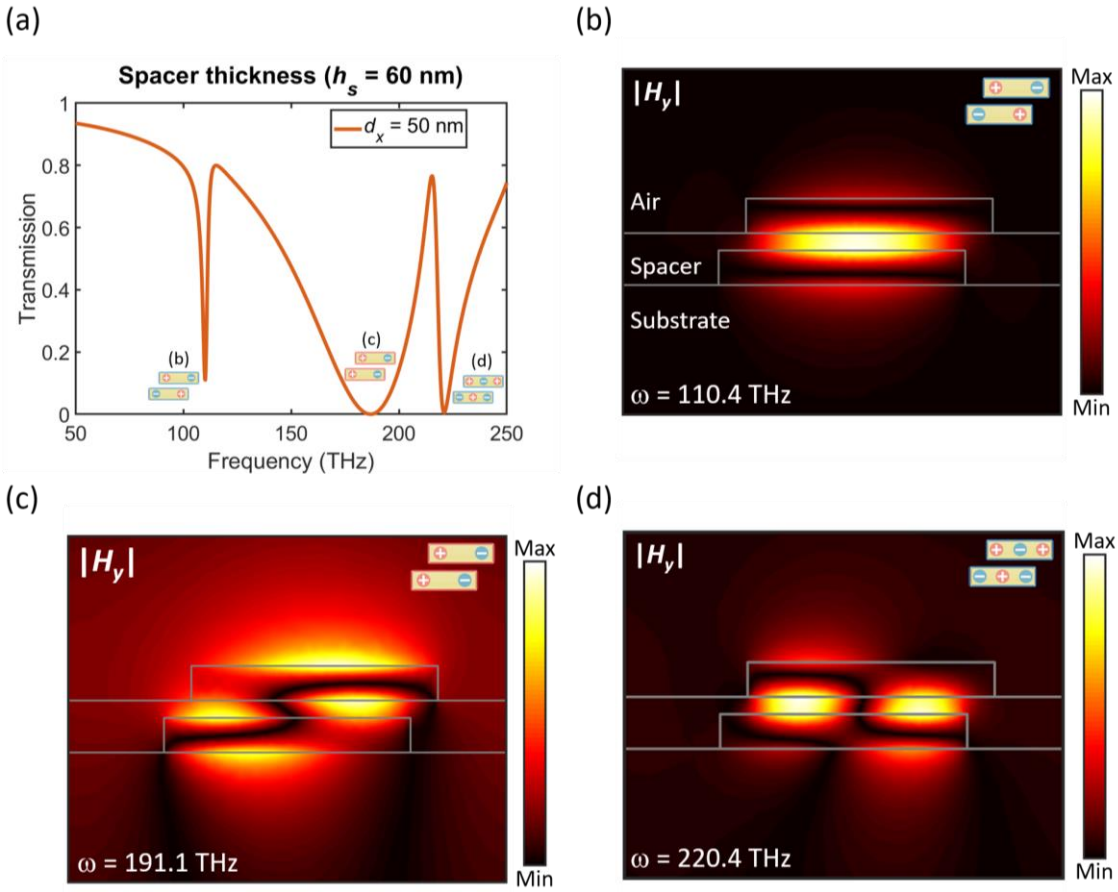

Figure 2.14 Calculated transmission and of the out-of-plane component of the magnetic field distribution. (a) Transmission of the structure with geometric parameters with h_s = 60 nm and d_x = 50 nm. (b) Antisymmetric mode (ω = 110.4 THz) (c) Symmetric mode (ω = 191.4 THz) (d) Second-order antisymmetric mode (ω = 220.4 THz).

Interestingly, for small d_x of space thickness h_s = 60 and 90 nm, the resonance can be identified as being the second-order mode of the magnetic resonance [30] in the spectra in Figure 2.13 between 200 to 250 THz for h_s = 60 nm and approximately 250 THz for h_s = 90 nm. This

second-order antisymmetric mode arises due to the slight symmetry breaking, lateral shift, introduced in the multilayered structure. For higher h_s, the higher-order modes reside out of spectral range in the calculation.

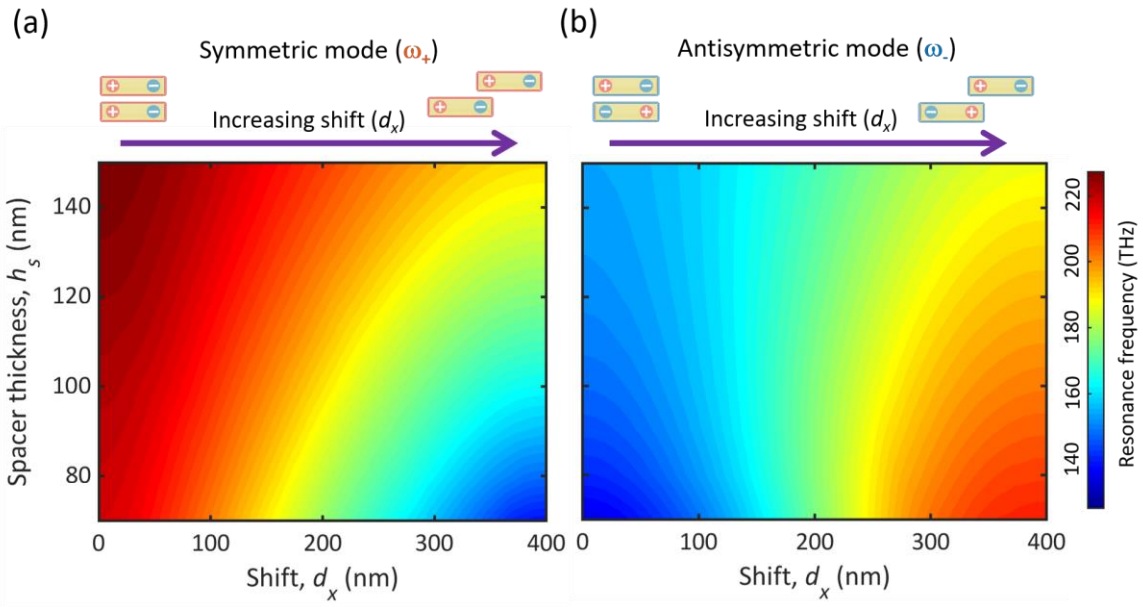

Figure 2.15 Color maps for resonance frequencies of plasmon hybridized modes in multilayered structure with h_s and d_x variation. (a) Symmetric mode (ω_+) (b) Antisymmetric mode (ω_-).

To verify the existence of second-order antisymmetric mode, the magnetic field of the multilayered structure was calculated with the geometrical parameters of h_s = 60 nm and d_x = 50 nm. Figure 2.14 presents the transmission and magnetic field of the structure. The transmission constitutes three different resonant plasmonic modes with minimum positions in frequency. The maximum of single magnetic resonance between nanorods is seen in Figure 2.14 (b), and the electric resonance in a multilayered structure is also presented in Figure 2.14 (c). In particular, the induced current flow between nanorods leads to two maximums in Figure 2.14 (d), and the maximum magnetic field is phase-shifted by π, the so-called odd mode profile [30].

Next, the inversion of the plasmon hybridized scheme is investigated with two geometrical parameters, lateral shift (d_x) and spacer thickness (h_s). Figure 2.15 displays the resonance frequencies of two hybridized modes with a progressive variation of d_x and h_s. Obviously, the symmetric mode moves to a lower frequency by increasing the lateral shift, whereas the antisymmetric mode shifts to a higher frequency as expected. The breaking symmetry using lateral displacement of one nanorod can invert the plasmon hybridization scheme. The strong near-field coupling between nanorods can be directly controlled in the multilayered structure.

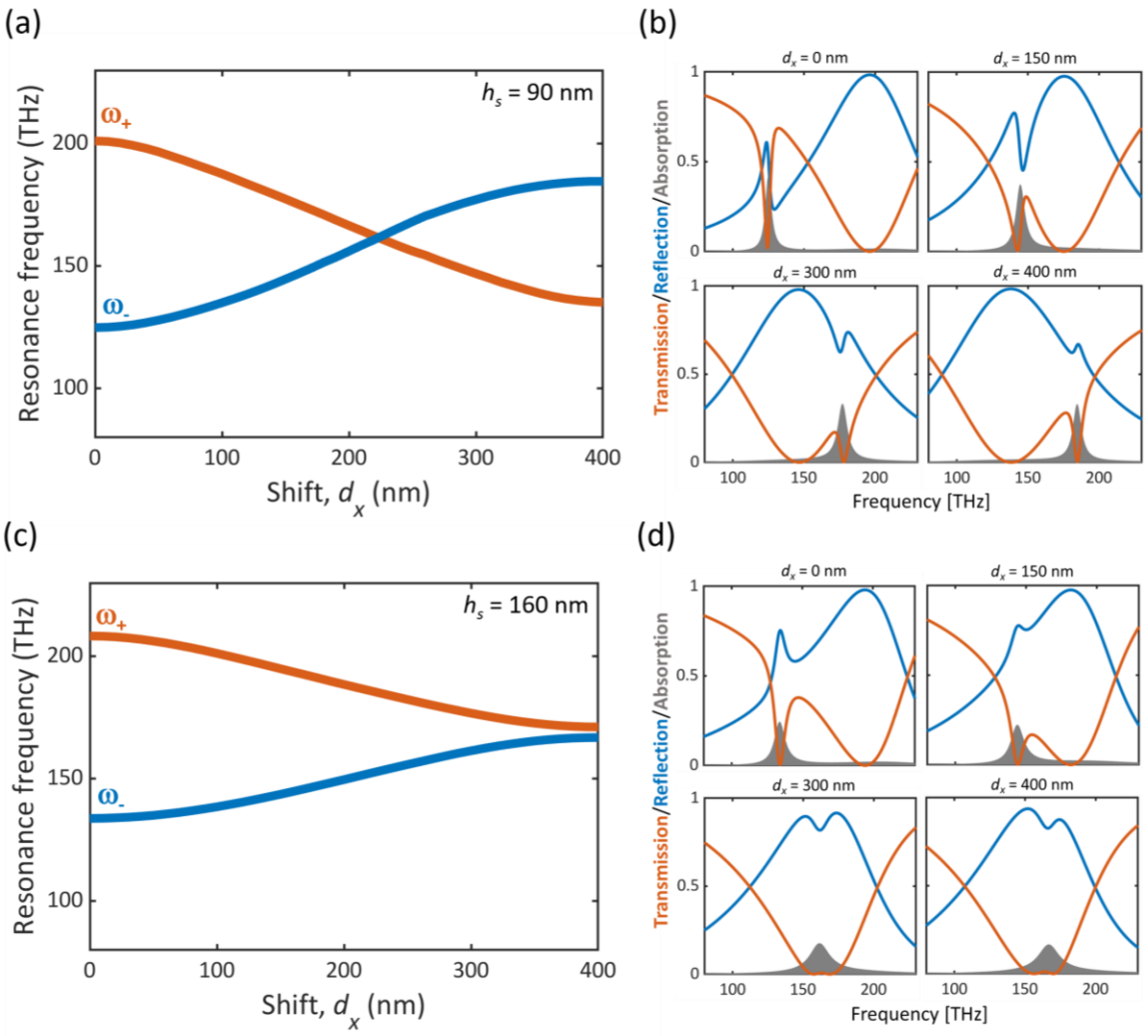

Figure 2.16 Resonance frequency of hybridized modes and transmission, reflection, and absorption for multilayered structure with increasing lateral shift for different spacer thickness. (a, b) Structure with h_s = 90 nm (c, d) structure with h_s = 160 nm.

The influence of spacer thickness (h_s) on the hybridization scheme is also investigated. Figure 2.16 shows the calculated resonance frequency of two plasmon modes and transmission with increasing lateral displacement. The calculated results reveal that spacer-dependent nanorods coupling affects the inversion of the plasmon hybridization scheme. The structure with h_s = 90 nm shows successful hybridization inversion. The resonance frequency of hybridized modes crosses after d_x = 240 nm. The displayed spectra in Figure 2.15 (b) reveal that the related dips (peaks) in transmission (reflection) are modified in resonance positions on the large displacement (d_x > 240 nm). The absorption peaks shift to a higher frequency when increasing d_x, which resemble antisymmetric mode behavior. No inversion of the plasmon hybridization scheme is observed in the case of the structure with h_s = 160 nm, as shown in Figure 2.16 (c). An increase in the spacer thickness weakens the near-field interaction. For a large shift of d_x = 300 nm and 400 nm in Figure 2.16 (d), the resonance frequencies of hybridized modes are close to each other, which results in broadening absorption linewidth.

2.6 Conclusions

In summary, this chapter has provided a thorough study of the simple plasmonic array and the plasmonic hybridization. Near-field interaction in multilayered plasmonic structure has been discussed. The resonance behavior of isolated plasmonic arrays is numerically investigated. Various geometrical parameters achieve the tuning resonance frequency in a plasmonic array, including nanorod dimension and unit-cell size. Indeed, the plasmonic array exhibits many degrees of freedom to steer the resonance frequency systematically. A plasmonic hybridization system is a valuable tool for the qualitative description of the observed coupling effects. Generally, the coupled plasmon resonator comprises two hybridized modes, symmetry and antisymmetry mode.

The opposite characteristic of two hybridized modes is investigated with varying unit-cell geometrical parameters. With structure variation, the antisymmetric exhibits a pronounced resonance shift in frequency. This provides insight in sensing applications with respect to perturbation of the system. Inversion of the hybridization scheme is realized by introducing later displacement (d_x). The inversion provides an intuitive understanding of the near-field coupling between two nanorods. This will be investigated in detail in the upcoming chapter, where hybridized sensing platform to improve sensing capabilities.

Chapter 2, in part, is a reprinted of the materials as it appears in J.-H. Park, A. Kodigala, A. Ndao, and B. Kanté "Hybridized Metamaterial Platform for Nano-Scale Sensing", *Opt. Express*, **25**, 15590 (2017). This work was co-authored by the dissertation author was the primary researcher and author of this paper.

CHAPTER 3: Nanofabrication Techniques for 3D Plasmonic Nanostructure

3.1 Introduction

In this chapter, we will introduce the nanofabrication process for the multilayered plasmonic structure. Nanoscale device processing technology is heavily based on using a positive tone resist. The resist sensitivity and contrast are partly dependent on the resist material property, also partly dependent on the resist process conditions. Especially, the process conditions are subject to pattern density and exposure conditions, such as the beam energy and exposure dose. Therefore, in this section, we investigate an electron beam lithography (EBL) resist optimum process condition to achieve a high-quality pattern, such as cross-sectional shape and line edge roughness (LER), an essential issue for nanofabrication.

3.2 Cold Development for Resolution Enhancement

Substrate preparation is crucial for nanofabrication in that a clean substrate is necessary for high-resolution [30]. In order to avoid contamination, the substrate (BK7) was immersed and fully cleaned with acetone 5 min and then isopropanol for another 5 min in an ultrasonic bath and rinsed in DI water and dried with a nitrogen gun. A hotplate baking of 1 min at 100°C drives off the solvents. Next, polymethyl methacrylate (PMMA, Microchem) resist was spun onto the BK7 substrate. The molecular weight of PMMA was 950 K, and the thickness for PMMA A2 and PMMA A4 at 5000 RPM for 60s yield 50 nm and 200 nm, respectively. After the spin-coating step, BK7 substrates with PMMA were baked at 180°C for 5 min on hotplate just prior to the lithography process.

In the EBL process, the lift-off process is a subsequent process to define patterns because this process can make patterns with a variety of material. Polymethyl methacrylate (PMMA) is one of the first positive tones resists developed for EBL and remains the most used resist for nanofabrication. PMMA has an extremely high resolution, and its ultimate resolution has been demonstrated to be less than 10 nm. Patterning resolution, the quality of narrow lines, cross-sectional shape, and absence of residue at the bottom of trenches are critical for successful lift-off. When electron beams expose to PMMA resist, it takes many scission events of polymer chains and turns them into several shorter fragments. After exposure, PMMA resist typically immersed in a liquid developer (MIBK:IPA=1:3 solutions, Microchem) to dissolve the fragments. While exposing the electron beam, scattered electron beam from the substrate also cuts the polymer chain from the bottom side, and it gives rise to a negative angle of the developed area. However, when the resist is in the developing process, the corner of the top surface of the resist also will be developed and make a positive angle. The positive angle on the top surface makes materials to be deposited on the sidewall, and it brings about very poor pattern definition as Figure 3.1 (a). However, instead of development at room temperature (25 °C, normal EBL process), by performing development process at a lower temperature (5 °C, cold development process) [31], [32], PMMA can be cooled, and the higher molecular weight chain fragments become less sensitive than lower molecular weight fragments that would be found in the exposed region. The lower molecular weight region, the bottom of the resist, will be developed faster than the higher molecular weight region. This process helps the vertical angle make negative to prevent sidewall deposition, and the fine patterns can be obtained as Figure 3.1 (b).

When a feature is exposed in PMMA, the soluble resist in the exposed region is surrounded by a boundary region of the resist that, due to the initial polydispersity of the PMMA and random

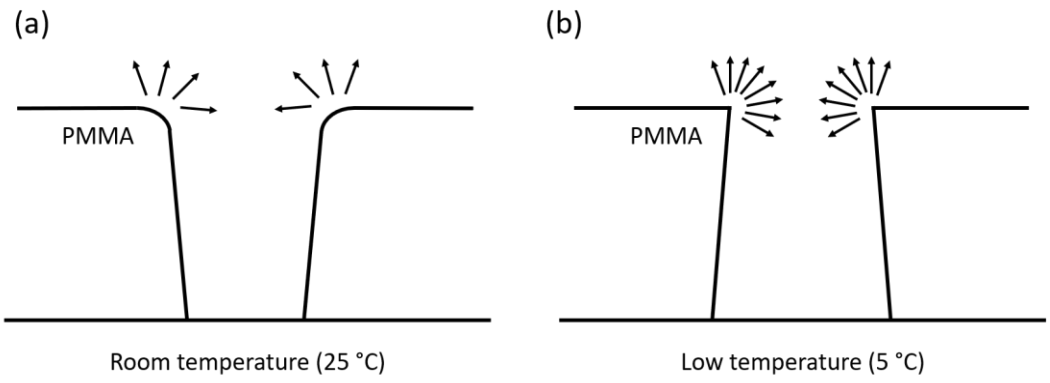

Figure 3.1 The effect of cold development on improvement in shaping trench edges for higher contrast. (a) Room temperature (b) Low temperature.

nature of chain scission contains both soluble and insoluble polymer chains. Figure 3.2 shows the development process, this region phase-separates, with the soluble chains diffusing toward the insoluble region. The result is a region of soluble PMMA that is larger than the initially exposed feature, resulting in a degradation in resolution. Cold development helps prevent this by limiting the diffusion that can occur in the boundary region since diffusion is a thermally dependent process [33], [34].

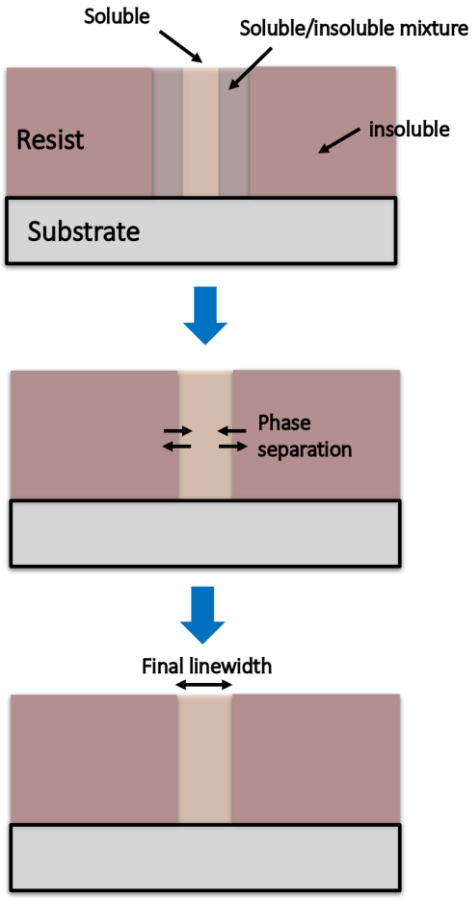

Figure 3.2 Schematic illustration of the determination of final linewidth in cold development.

To explore the effects of cold development on the resolution of EBL at the nanometer scale, several samples were exposed on a Vistec EBPG5200, at an accelerating voltage of 100 kV in PMMA A4 (~ 200 nm) and developed in a 3:1 solution of IPA: MIBK with two different temperatures. This was followed by gold lift-off using the evaporation technique. For the cold development (5°C), the development time is three times longer than the case of the room temperature (25°C).

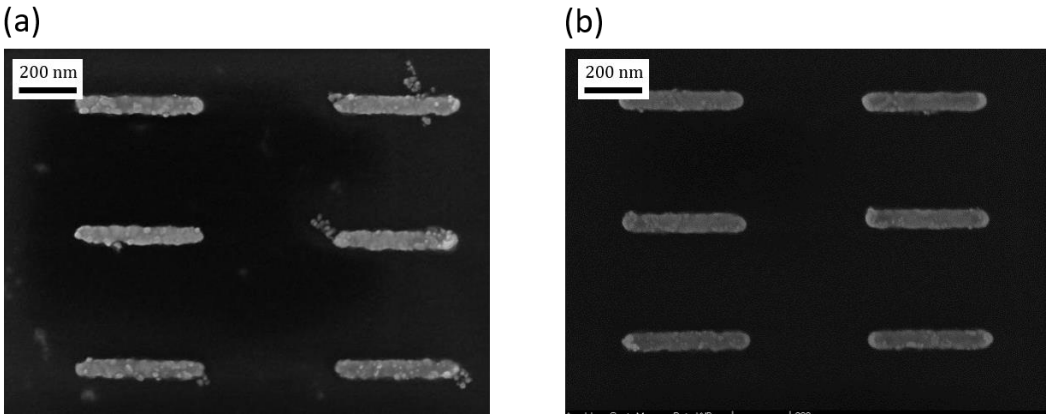

Figure 3.3 SEM images of the different temperatures of the developer. (a) Developed at 25°C (room temperature) and (b) at 5°C (cold development process).

The samples with room temperature development process represent the very poor quality of sidewall and roundness of corner in Figure 3.3 (a). The dimension of the fabricated pattern fails to match the design with sharp lines. In contrast, nanoparticle patterns with the cold development process achieve an improved quality of the EBL lift-off process in Figure 3.3 (b). The experimental results prove the cold development process affects key issues of high-resolution EBL, such as line edge roughness, resist residue, pattern quality, and cross-sectional shapes.

3.3 Bi-layer Resists for Clean Lift-off

Metal lift-off is a common transfer method for the EBL application. It has been widely used for device fabrication, interconnections, and test structure. High quality of metal lift-off normally requires wide undercut to prevent sidewall connection as well as adhesion of metal to substrate. A single layer of PMMA resist with cold development process can be used for lift-off. The cold development process can form a negative angle of the sidewall in PMMA resist to make fine patterns, but the process fully depends on maintaining lower temperatures. If the developing temperature is not stable in the process, the vertical profile of PMMA resist has a positive sidewall,

as shown in Figure 3.1 (a). Aa a result, insufficient undercut would cause sidewall connection. Bi-layer resists, MMA/PMMA process using two types of resists can give more undercut. An undercut resists profile with an appropriate geometric shape is often needed to lift off the deposited thin metal film. Methyl methacrylate (MMA, Microchem) has a lower-molecular-weight than PMMA resist. For the EBL resist preparation, Higher-molecular-weight resists PMMA is applied over a lower-molecular-weight MMA layer. After the EBL and development process, the lower-molecular-weight resist, MMA, gives a larger aperture to form significant undercut due to the fact that the sensitivity difference between resists to electron beam exposure. Therefore, the vertical profile of the developed structure will have two steps, and the bottom step in the MMA region will be wider than the top step, PMMA region. The fabrication process of a single layer of PMMA resist and bi-layer MMA/PMMA resists are described in Figures 3.4 and 3.5, respectively.

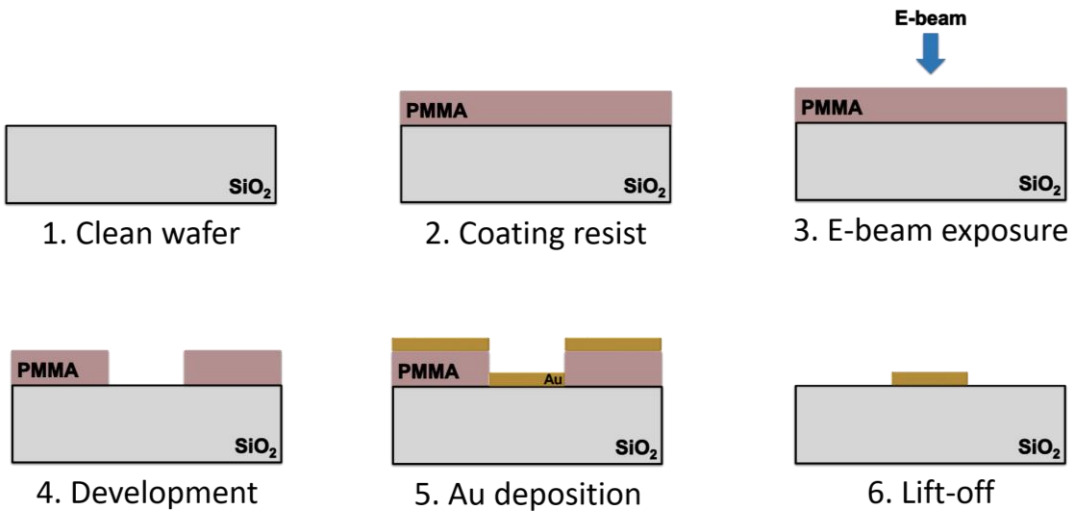

Figure 3.4 Schematic illustration of lift-off process with PMMA single layer.

The bi-layer resist, firstly, MMA and PMMA are spun on the substrate in order, and the electron beam is exposed on the top layer, PMMA resist. The difference in sensitivity to the electron beam, the top, and bottom layer makes it possible to achieve a sufficiently large undercut

resist profile, which is a prerequisite for a clear separation between the evaporated films on the resist and on the substrate. Figure 3.5 showed a comparison between the single and bi-layer resist process.

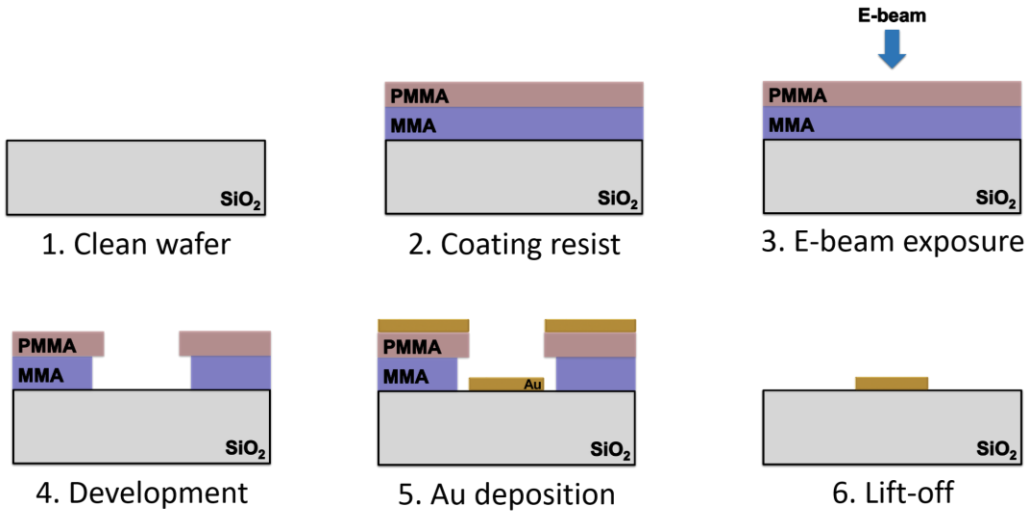

Figure 3.5 Schematic illustration of the EBL Lift-off process with bi-layer MMA/PMMA resist.

The SEM image clearly that sharp line edges of nanorods patterns with various lengths, 450, 250, and 150 nm are successfully achieved by the bi-layer resist process. Using the bi-layer resist the process and optimized parameters, enough undercut resist profile for lift-off was achieve, and a very fine pattern without any residue can be obtained.

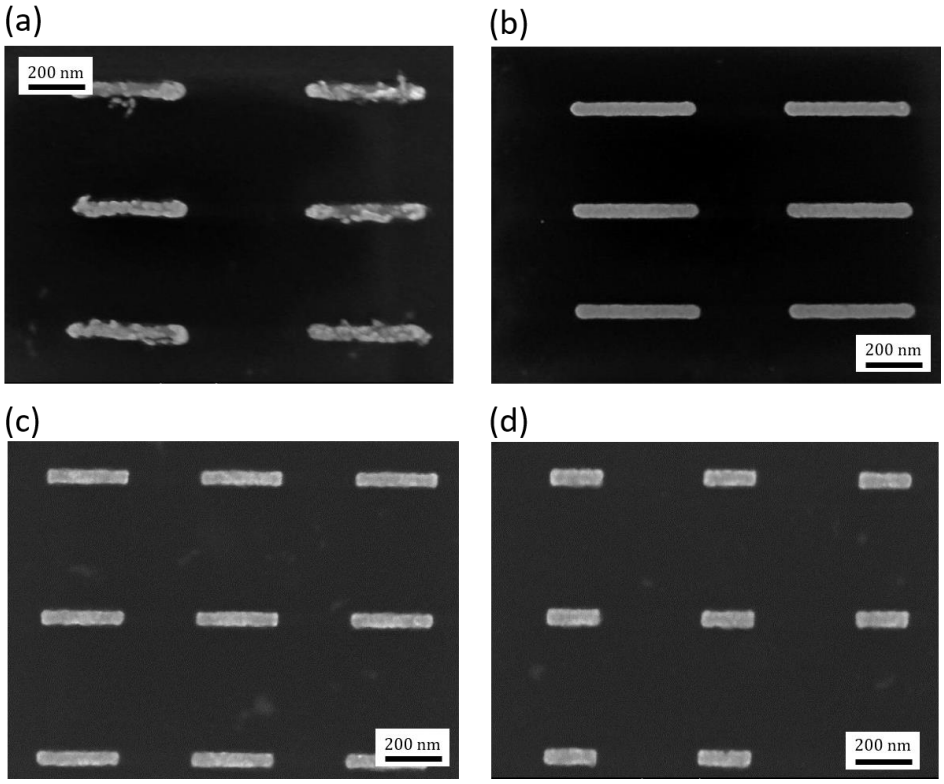

Figure 3.6 SEM images of single and bi-layer resist process. (a) A single layer of PMMA resists, (b)-(d) Bi-layer of MMA/PMMA resist, nanorod length (*L*) is 450, 250, 150 nm, respectively.

3.4 EBL Alignment

The fabrication of functional nanoscale photonic devices often requires multiple lithographic exposures within 10 nm accuracy [33, 34]. It is important that the nanostructure defined in these different lithography processes are positioned accurately with respect to each other. The process of positioning a pattern during electron beam exposure so that it is matched to some existing features is known as 'alignment.'

Alignment in electron beam lithography is generally performed by locating four markers and then mapping the stage coordinate system onto the designated coordinates of the markers [35]. The physical structure of the marker must be suitable for detection by the electron beam system. When an electron beam is scanned across on the surface of a substrate, a signal is generated. The electrons

penetrate beneath the surface of the substrate, experience collision, and are backscattered toward the backscatter detectors. The backscattered electrons are modulated by the steps or contours on the surface or within the substrate. Figure 3.7 shows how some of the electrons emerging from alignment markers on the substrate surface can be detected. Some secondary electron detectors can pick up a significant fraction of the backscattered electron and be used for marker detection. Typically, the markers are made of metal with a high atomic number, dense materials, such as gold or tungsten. This is because the backscattered yield can be enhanced by the atomic number. Figure 3.8 shows the minimum thickness of the marker for various materials and topographical markers. The minimum thickness of the marker can be express by

$$T_{marker} = 2600/(Z - 14) \quad (2)$$

where Z is the atomic number in the periodic table, for example, copper (Cu), atomic number is 29. The minimum thickness of the marker requires 170 nm, and for Niobium (Nb), atomic number and minimum thickness are 41 and 100 nm, respectively. Gold (Au) should be used because of its high

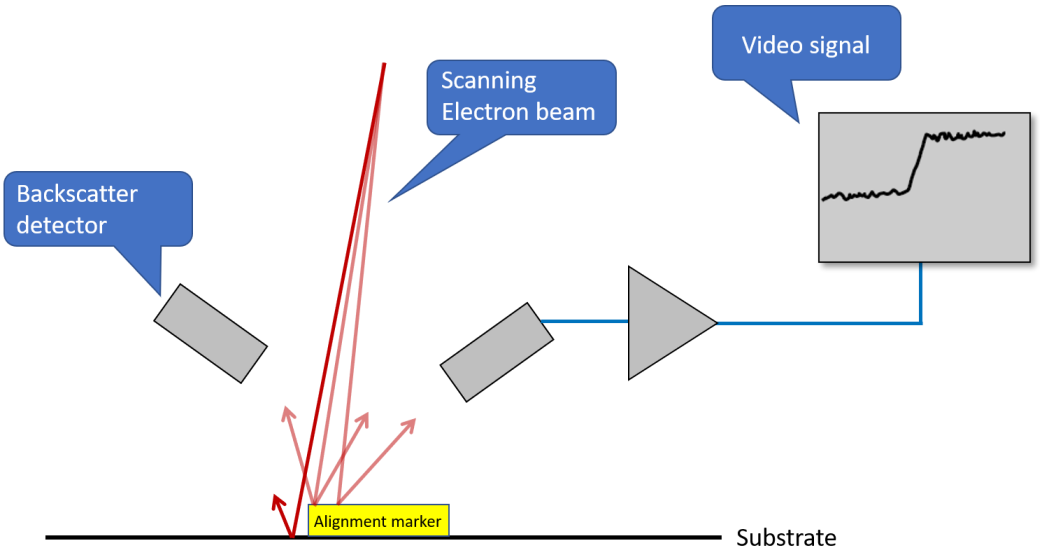

Figure 3.7 Schematic illustration of the alignment marker detection via backscattered electron imaging.

atomic number (Z = 79) contrast with SiO_2 substrate, as seen in Figure 3.8. It can decrease the thickness of the marker to 40 nm and can simplify the fabrication step, and a single evaporation process can be used to make alignment markers and nanorods at the same time. Another sort of marker is an etched structure. A deep hole will appear dark under backscattered illumination, but as the depth decrease, the center of the hole becomes brighter, and only the edges provide good contrast. To obtain a uniform contrast within the hole, an aspect ratio of about 0.3 is required (e.g., 3 μm deep for a 10 μm wide marker). This is not easy to achieve. It will increase the complexity of the fabrication process [36].

The marker shape is arbitrary. Squares are often used, but so are rectangles, crosses, and more complex shapes. Here, simple shapes such as squares have the advantage of simplicity and mark detection algorithm. The size of a marker of 20 x 20 μm^2 is chosen due to the identifying geometry. Figure 3.9 shows the detected backscattered signal process, as described in Figure 3.7 when the electron beam is scanned across the marker. The position of rising and falling edge

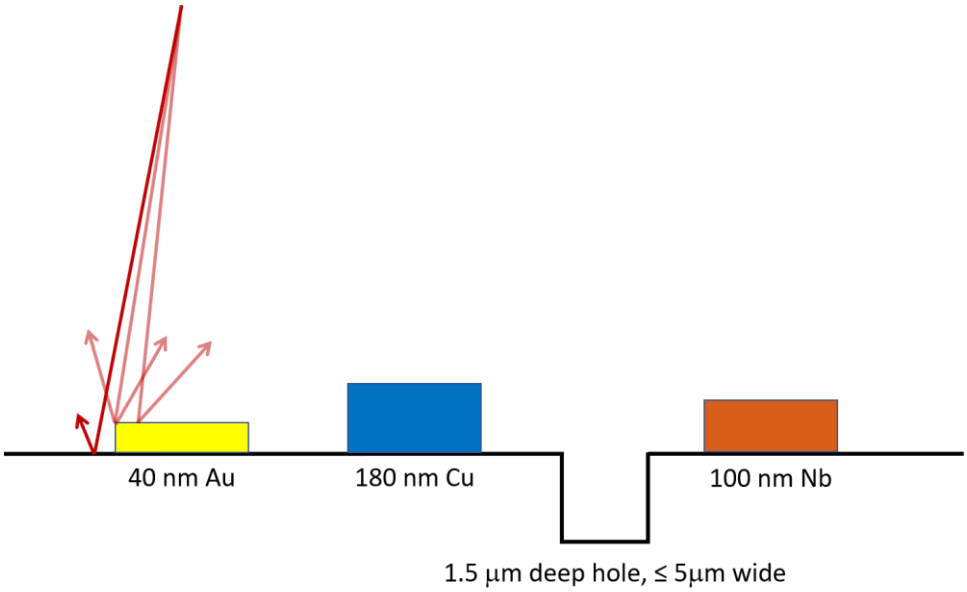

Figure 3.8 Alignment marker thickness for various metal materials and topographical markers.

equates to the marker edges, and these positions can simply be averaged to give a measure of X-position of the center marker. A similar scan in the vertical direction allows the Y-position to be found. The alignment markers are scanned repeatedly until a satisfactory alignment is obtained [37].

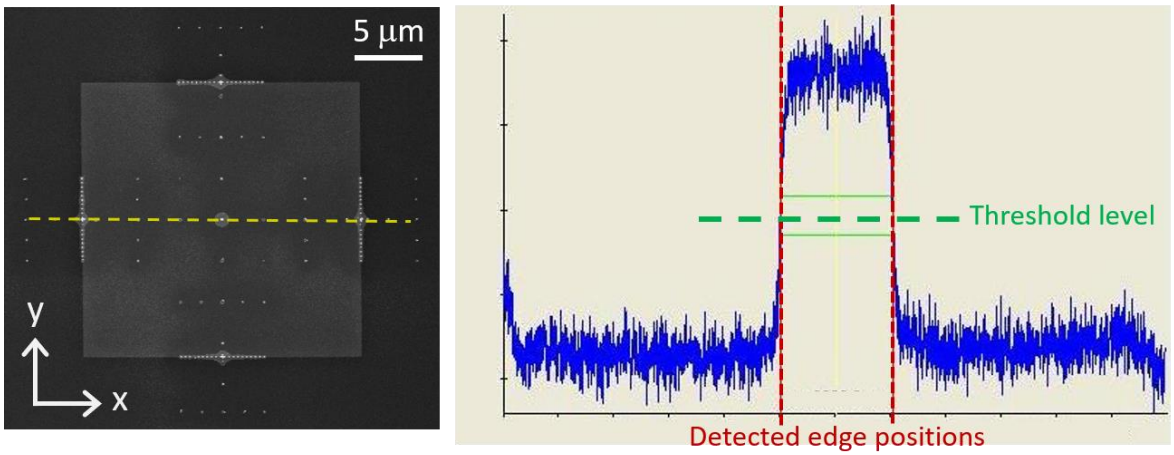

Figure 3.9 Signal produced in the process of marker detection when the electron is scanned across a metal square marker.

When designing EBL alignment scheme, in addition to the details of the marker materials and design itself, it is important to have the markers located in appropriate locations to provide necessary alignment accuracy for the patterns while optimizing the write time. The EBL system usually detects four global marker points P, Q, R, and S to use in calculating the expansion, rotation, and the shift amount of the substrate. Chip markers are positioned in the writing-field region to correct the deflection gain and rotation of the main and sub-deflectors in the writing-field region and write the pattern according to the shape. Two kinds of alignment markers, global and local, and writing-field regions in the EBL system are illustrated in Figure 3.10.

In this study, the comparison of overlay accuracy between global and local markers alignment process will be investigated, and an optimized alignment process will be achieved. The simplest alignment process would just use two global alignment markers, either P, Q, or R, S on the substrate, and this process would save writing time. When the pattern is written, it is translated,

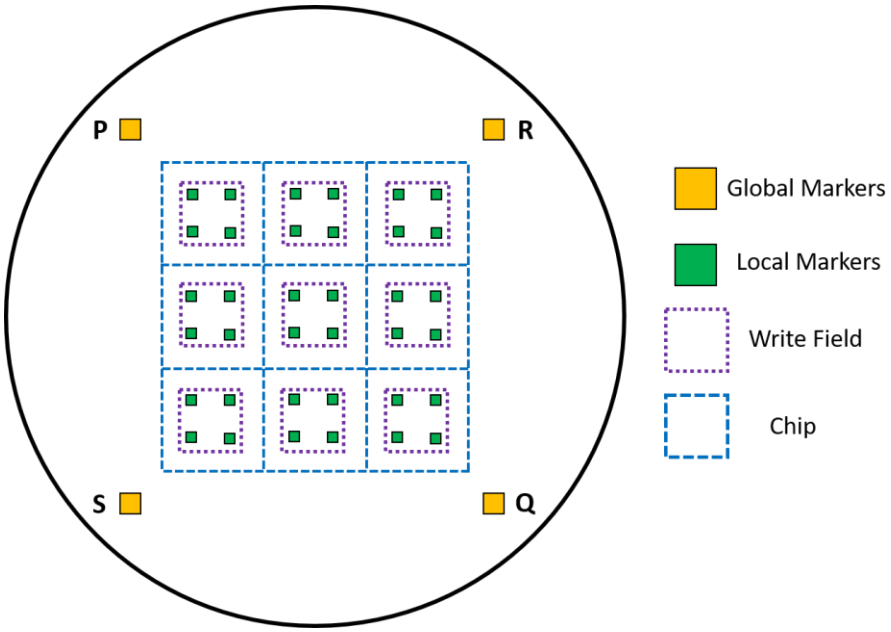

Figure 3.10 An example of alignment markers on a wafer.

rotated, and scaled by the amounts determined by those two global maker error vectors. Long-distance between global markers brings about a significant error vector [38]. In the EBL system, the wafer is not moved or rotated inside the system. However, better alignment can typically be achieved by aligning not only the substrate but also aligned in the smaller incremental region of the pattern. In this process, the wafer is still aligned using two or four global markers shown in yellow in Figure 3.10, but then each pattern unit is aligned using four local alignment markers shown in green. With each smaller unit corrected independently, alignment results are improved and summarized in Figure 3.11. Only the global alignment marker shows over 50 nm accuracy, misaligned overlay. In contrast, the combination of global and local alignment marker has only 5 nm overlay accuracy. Even though the alignment process with global and local marker increase writing time, the alignment error is achievable below 5 nm, which is the best approach to get a well-aligned overlay.

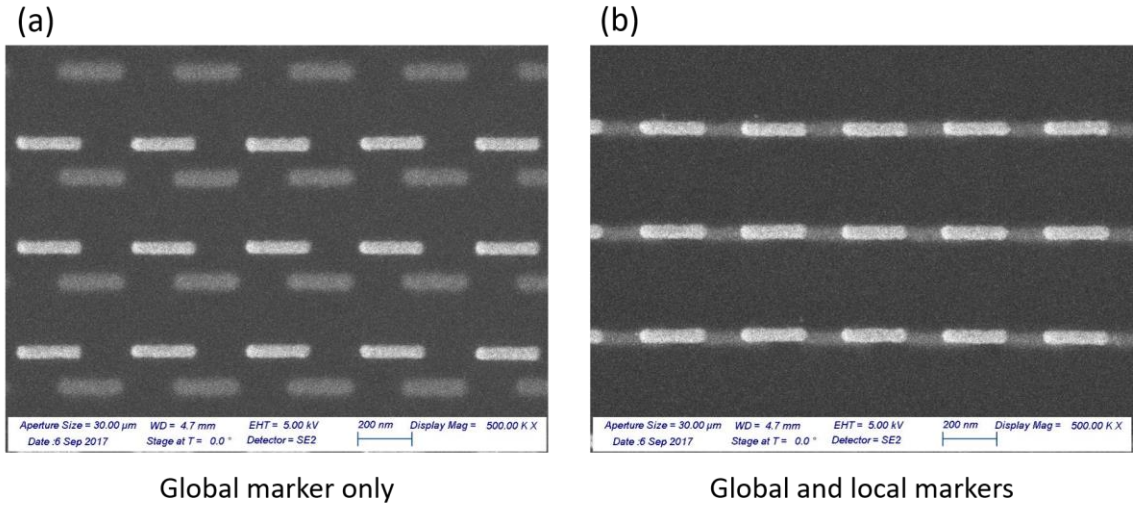

Figure 3.11 SEM images of alignment results. (a) Global alignment marker only (b) Global and local alignment marker.

Another alignment issue is observed in the EBL process. While the electron beam is scanned to find alignment markers described in Figure 3.7, the electron scanning area should be considered. Figure. 3.12 shows the interference between the scanned electron beam and nanorod pattern. During the alignment process using electron beam scanning, PMMA resist reacts to electron beam resulting stitching pattern after development and lift-off process. To avoid the interference in EBL alignment process, the 1st alignment markers are moved away from the pattern illustrated in Figure 3.12 with yellow and blue colors, respectively.

The ability to perform highly accurate alignment EBL process plays an important role in the fabrication of 3D nanoscale photonic devices and CMOS compatible integrated devices. Experimental demonstration of high accurate overlay below 5 nm is achieved using appropriate material and position of alignment marker. This will open the route to application in three-dimensional, isotropic, and bulk material and devices.

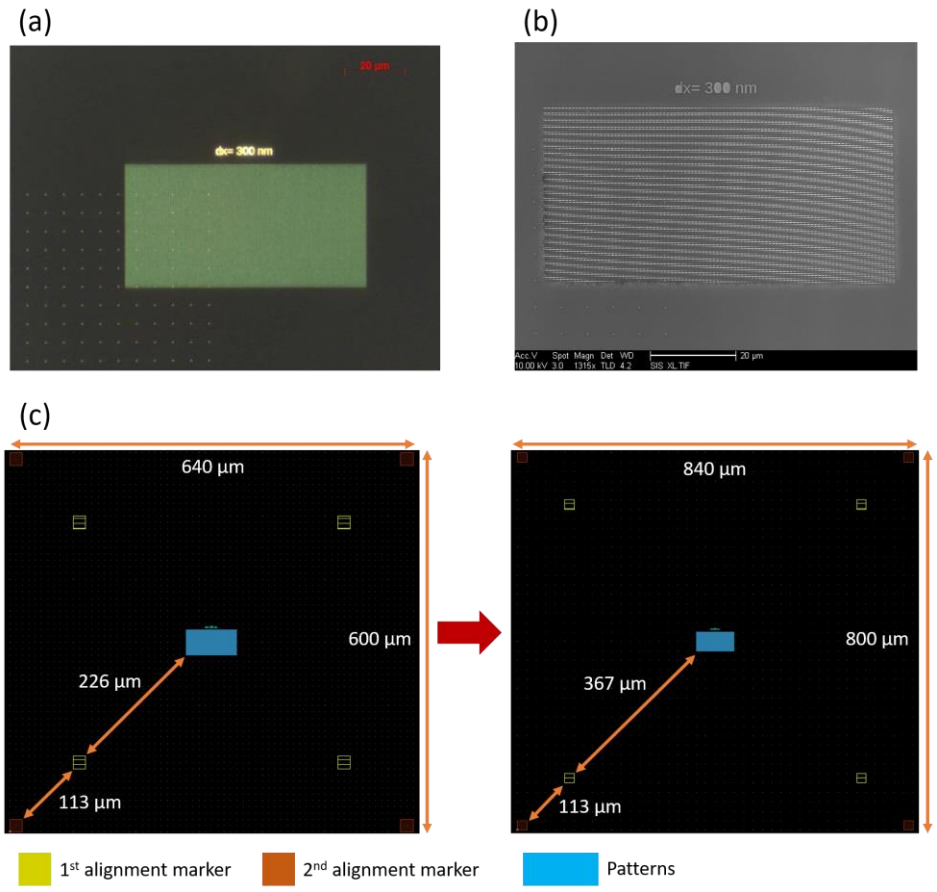

Figure 3.12 Scanning electron beam interference to pattern and alignment position modification. Results of interfered scanning electron (a) Microscope image (b) SEM image (c) Alignment marker modification in distance between marker and pattern.

3.5 Insulating Substrate

Application areas such as photonics, nanoelectronics, and the bio-electromechanical system often require fabrication of large, microscopic-scale arrays of nanoscale features. Transparent dielectric materials encounter a major hurdle when employing EBL for nanostructure fabrication. Even though most resist are insulating, charging is not an issue for typical resist thickness less than 500 nm, because most electrons penetrate deep into the conducting substrate [39]. Figure 3.13 illustrates the charging effect in the electron beam writing process. When electron beam lithography must be carried out on insulating substrates such as quartz, SiO_2, and then negative

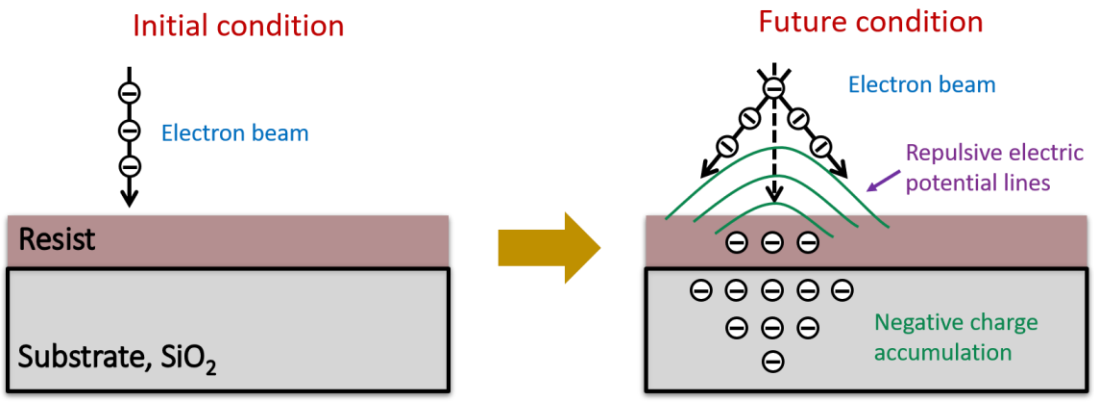

Figure 3.13 Schematic illustration of charging during e-beam writing. The charging accumulation on the surface results in a considerable amount of pattern displacement and distortion.

charge buildup can occur on the substrate surface, give rise to beam deflection, and thus pattern distortion. Figure 3.14 shows nanorod array fabrication results with a charging effect, giving rise to pattern displacement, pattern distortion, and registration error. In this study, the charging effect in the EBL process and its improvement are experimentally investigated. The optimized EBL preparation for eliminating the charging effect also demonstrated systemically.

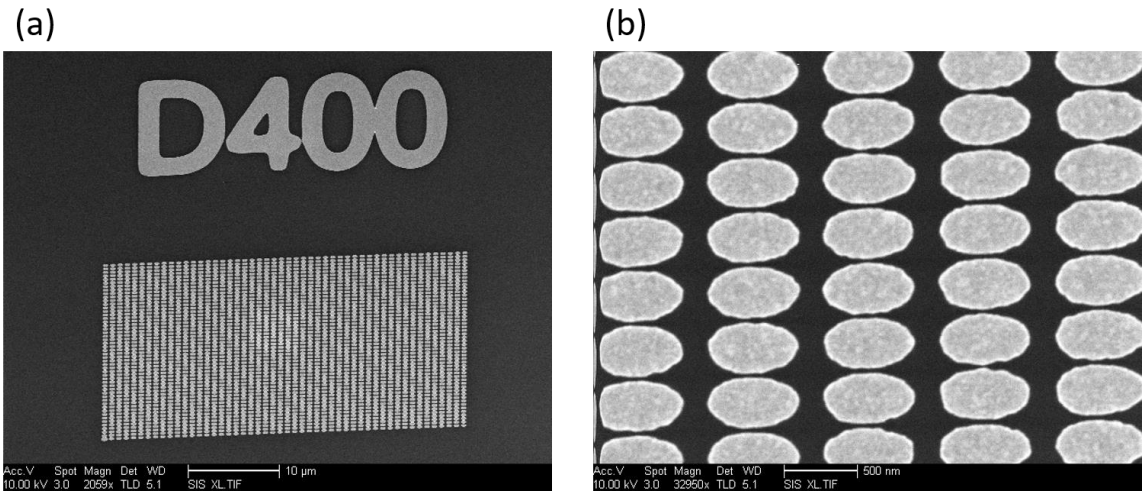

Figure 3.14 SEM images of fabricated nanorod array with the charging effect. Pattern displacement, pattern distortion, and registration error are clearly observed.

In an ideal electron beam lithography system, the stage plane and sample plane should be normal to the incident electron beam. This enables a focused beam to remain in focus at any point on the sample surface. When the beam focus varies across the sample, the writing resolution and stitching errors also vary. To ensure that the beam is focused on the sample, Vistec, the EBPG5200 system, is equipped with a height system, as illustrated in Figure 3.15. A height detection system measures the sample height and adjusts the beam focus before exposing a pattern [40]. This measurement is repeated in each exposure field. The laser in the system measures the sample height by projecting spot onto the surface of the substrate, and then the laser spot is reflected onto the Dual-diode detector. Signals from the Dual-diode detector determines distance moved by a laser beam. Thus, the laser spot movement due to changes in the height of the substrate surface is converted to a focus correction.

To eliminate the charging effect, one of the standards and simple solution to substrate charging is to evaporate a thin layer of metal on top of the resist. Anti-charging metals, such as aluminum (Al), gold (Au), and chrome (Cr), are widely used. Another solution is spin-coating

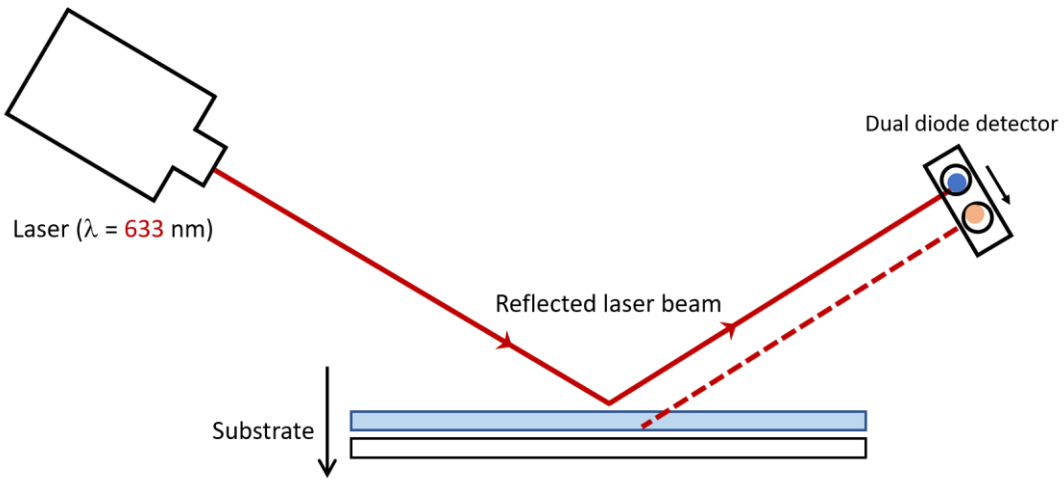

Figure 3.15 Schematic illustration of laser height sensor in the EBL system for focus correction.

conductive polymer such as Espacer [41] or AquaSave [42] on the top of the resist. However, Vistec, EBPG5200 system requires a height mapping step for focus correction on the surface of the substrate. Therefore, the conductive polymer is not an appropriate solution as a conducting layer due to the low reflected signal from the substrate. Here, the effect of thickness of the conducting layer, a thin gold film on charging, and focus correction will be investigated.

The deposition of a thin gold film on top of PMMA resist was carried out using a thermal evaporation system. Other physical vapor deposition methods, for instance, electron beam evaporation and DC sputtering may damage to PMMA resist due to X-ray radiation in electron beam evaporation and plasma glow in DC sputter. Different thickness of the gold layer (T_{Au}), 5, and 10 nm was deposited by thermal evaporation system. Figure 3.16 illustrates the EBL lift-off process with charging dissipation. It should be noted that gold etchant does not damage PMMA and substrate, and the thin layer of gold is compatible with this EBL process. The thickness effect of the conducting layer (T_{Au}) in the EBL lift-off process is shown in Figure. 3.17. The optical microscope and SEM images clearly prove that the thickness of the gold layer is crucial to correct focus in the height mapping process. Even though the thickness of 5 nm gold layer can eliminate the charging effect, it leads to a low reflected beam, preventing beam focus correction. The thickness of the gold layer higher than 10 nm may cause local current flow in the gold layer because of the high beam current density in electron beam exposure.

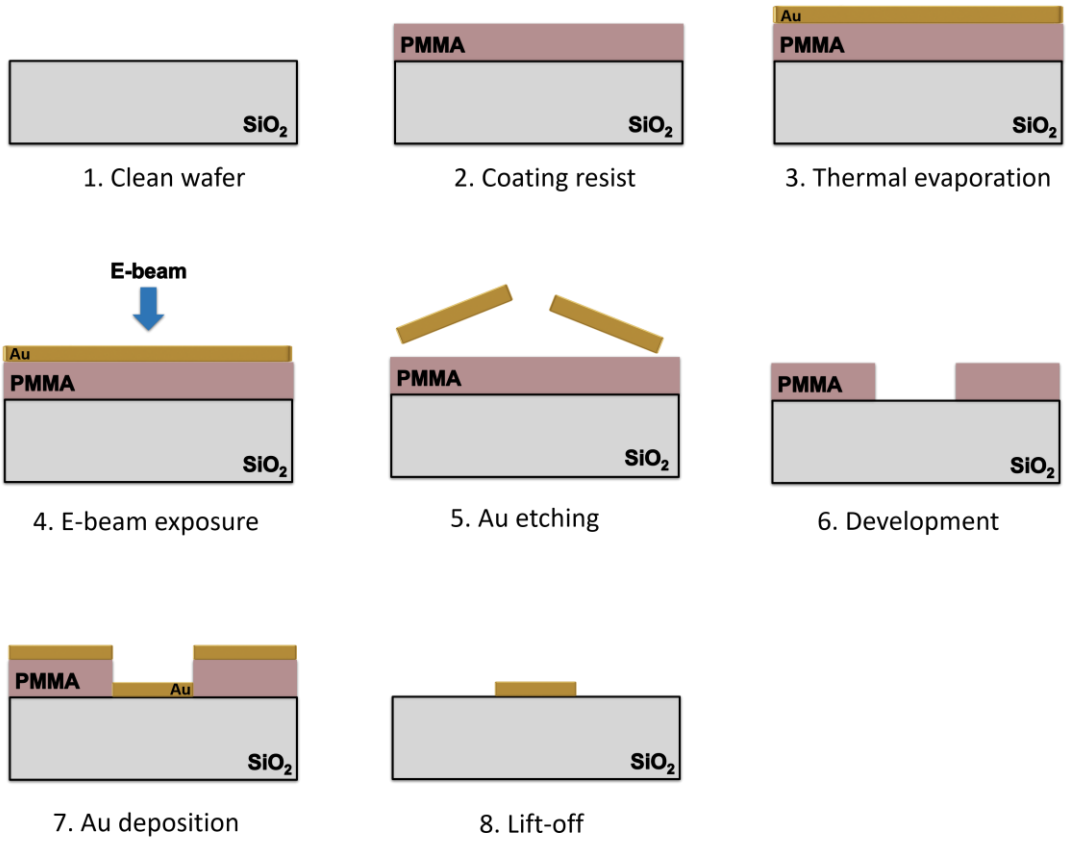

Figure 3.16 Schematic illustration of the EBL Lift-off process with a conductive layer on top of PMMA resist.

Charging dissipation for electron beam lithography is achieved by the optimum thickness of the 10 nm gold layer. We have demonstrated the capability of obtaining the highest resolution, least position error, and accurate overlay process. Following section, all fabrications are performed by cold development, bi-layer MMA/PMMA resist, and 10 nm of the gold layer as a conducting layer; otherwise, there is noted.

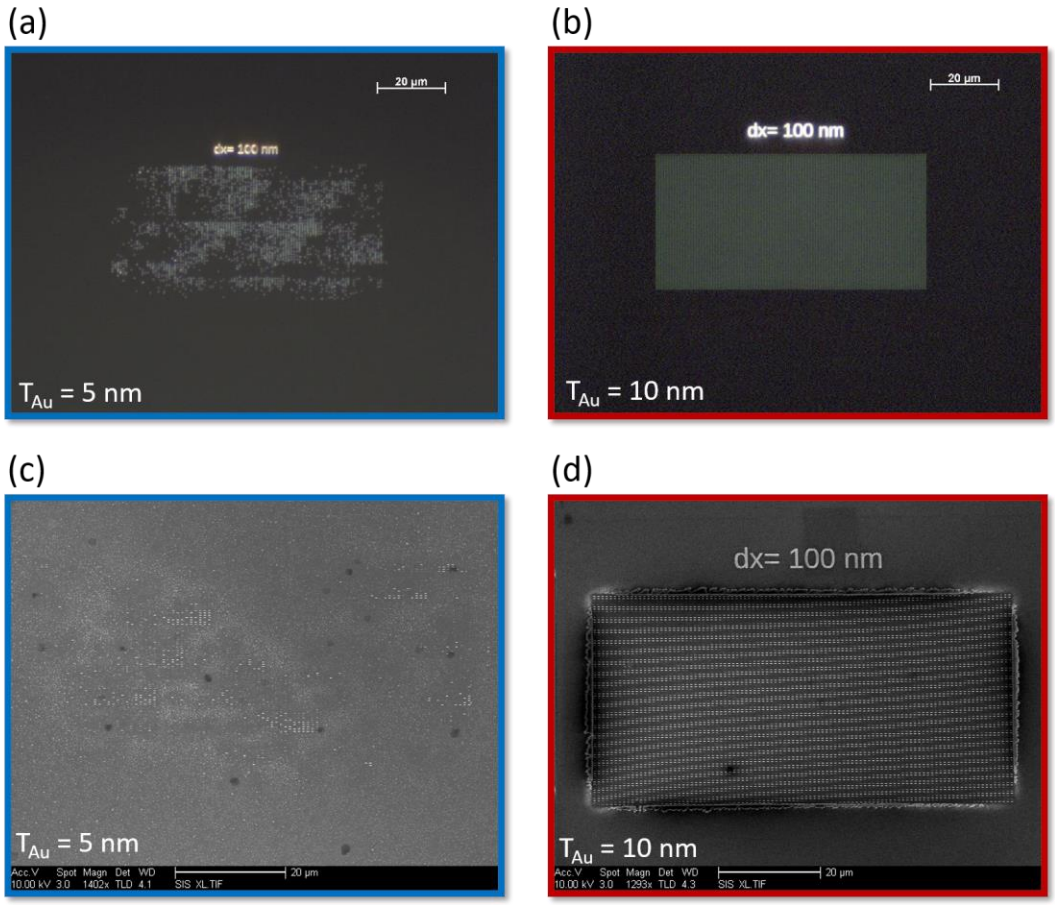

Figure 3.17 The thickness effect of the conducting layer in the EBL lift-off process. (a)-(b) Optical microscope images for 5 and 10 nm conducting layer. (c)-(d) SEM images, respectively.

3.6 Layer-by-layer Technique for 3D Nano-Device

SU-8 negative photoresist was originally developed and patented by IBM in 1989 [43]–[46]. This material was developed for applications that require excellent high aspect ratio and designed for use as a permanent photoresist. Fully cured thin or thick films are very stable against a wide range of acids, bases, and organic solvents. SU-8 is a unique material, which offers good adhesion to a lot of surfaces with careful processing conditions. SU-8 proceeds in a similar manner to other chemically amplified negative photoresist; the flowchart in Figure 3.18 highlights the interdependence between, and effect of, these processing stages on the final structure [47]–[49].

The prebake, postbake, exposure, and development stages are dependent on the application stage (which defines resist thickness). The development stage is, in turn, dependent on the two baking stages, and the postbake is, to an extent, dependent on the prebake.

SU-8 2000 is an improved formulation of SU-8, which has been widely used by MEMS producers for many years. SU-8 2000 is also best suited for permanent applications where it is imaged, cured, and left on the optical device. This negative-tone polymer exhibits the characteristic of a dielectric, planar surface, low viscosity, optical transparency, chemically inert, and simple process. In addition, SU-8 2000 is a photo imaginable resist, the area of interlayer can be

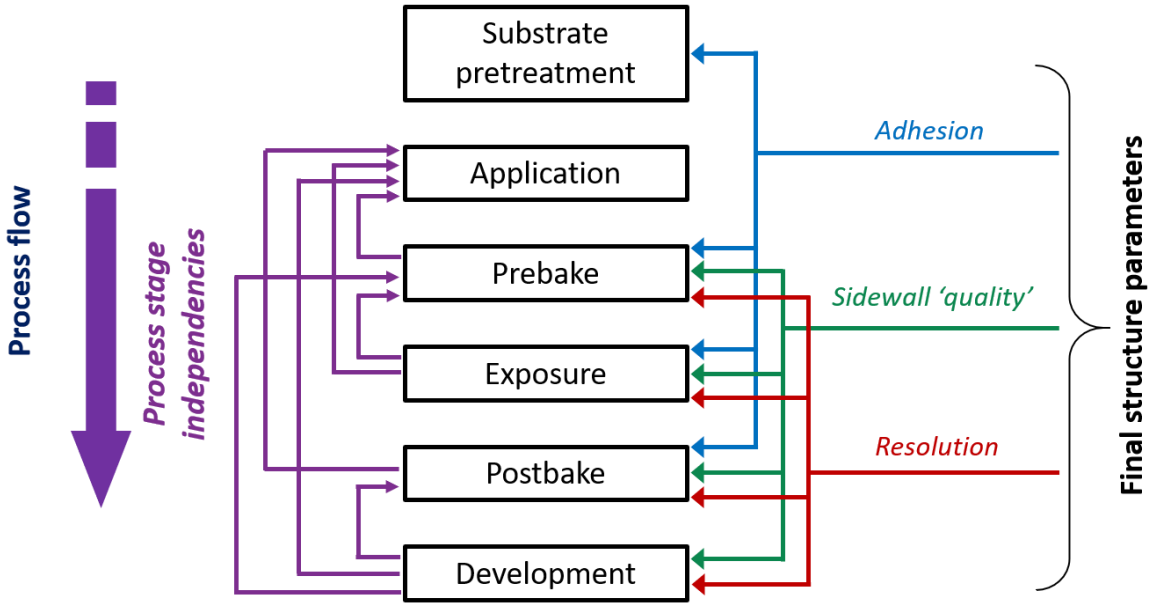

Figure 3.18 The Stage of the SU-8 process along with their interdependence and effect on final structure characteristics [47].

patternable for any purpose. The ability to stack multiple layers of SU-8 2000 to form a complex three-dimensional structure means SU-8 2000 offers increased versatility.

SU-8 2000 series can be reached to the desired thickness in the process of custom dilutions using SU-8 thinner, cyclopentanone. Resist thickness in the range of 100 to 1500 nm was

investigated by making a series of dilutions. Figure 3.19 shows the resist thickness as a function of solid content with two different spin speeds. SU-8 2002 (29.0 % solid contents) and SU-8 2000.5 (14.3 % solid contents) were used for dilution process to reach desired thickness, 1500, 1000 nm (SU-8 2002 dilution) and 500, 200 and 100 nm (SU-8 2000.5 dilution), respectively. The thickness of the SU-8 2000 series on silicon substrates was measure by Filmetric, optical thickness measurement. The volume ratio calculation between SU-8 2000 series and thinner to get the desired thickness is as follows.

$$V_{target} = (S_{init} \times V_{init})/S_{target} \quad (3)$$

where V is volume and S is solid content of SU-8 2000.

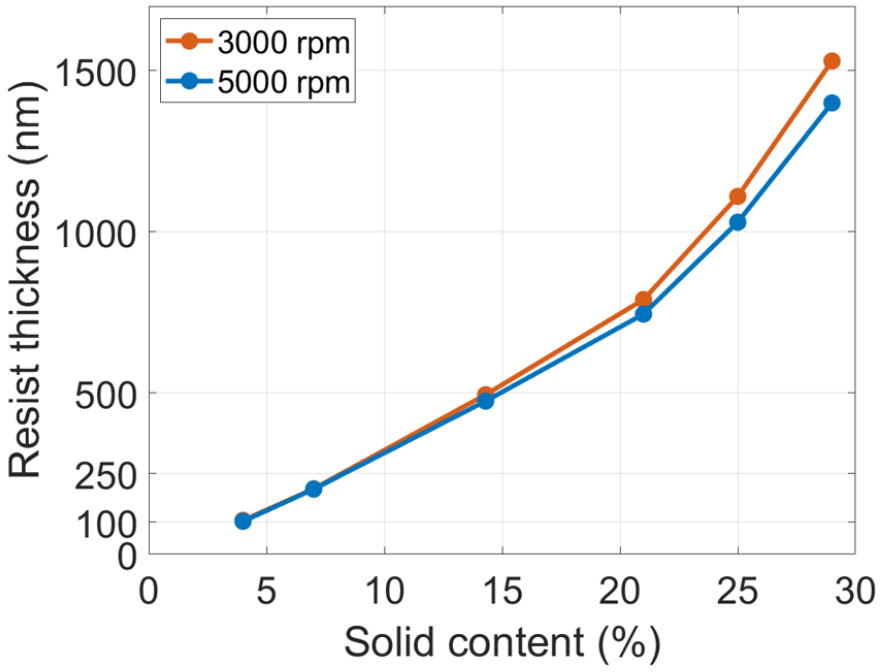

Figure 3.19 Resist thickness as a function of solid content with spin speed (3000, 5000 rpm).

Figure 3.19. shows the resist thickness of SU-8 2000.1 obtained in the dilution process with SU-8 2000.5. The measured thickness of SU-8 2000.1 exhibits consistent results to spin speed variation. The thickness of 100 nm is achievable over than spin speed of 4000 rpm.

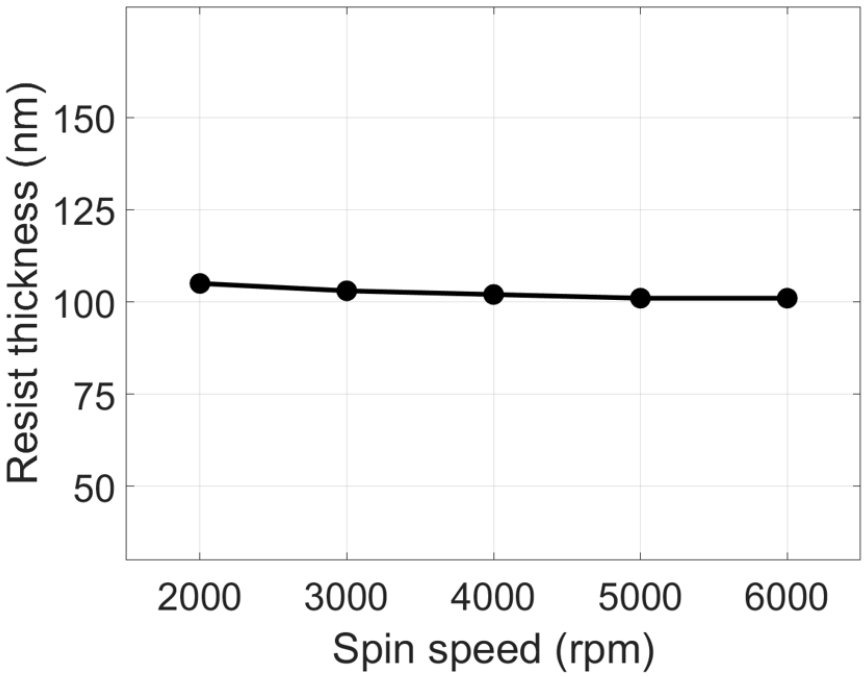

Figure 3.20 Spin curve of SU-8 2000.1 (4% solid contents).

Device fabrication typically starts with a flat surface. However, the surface becomes non-flat surface shortly after the fabrication process is started. As the first layer of structures is fabricated onto the substrate, this layer of topography is introduced onto the substrate surface. The topography plays a profound role in advanced devices that contain multilayers of sub-micron or finer structure. Thus, planarization technology is developed to reduce or eliminate the topography in device fabrication processes.

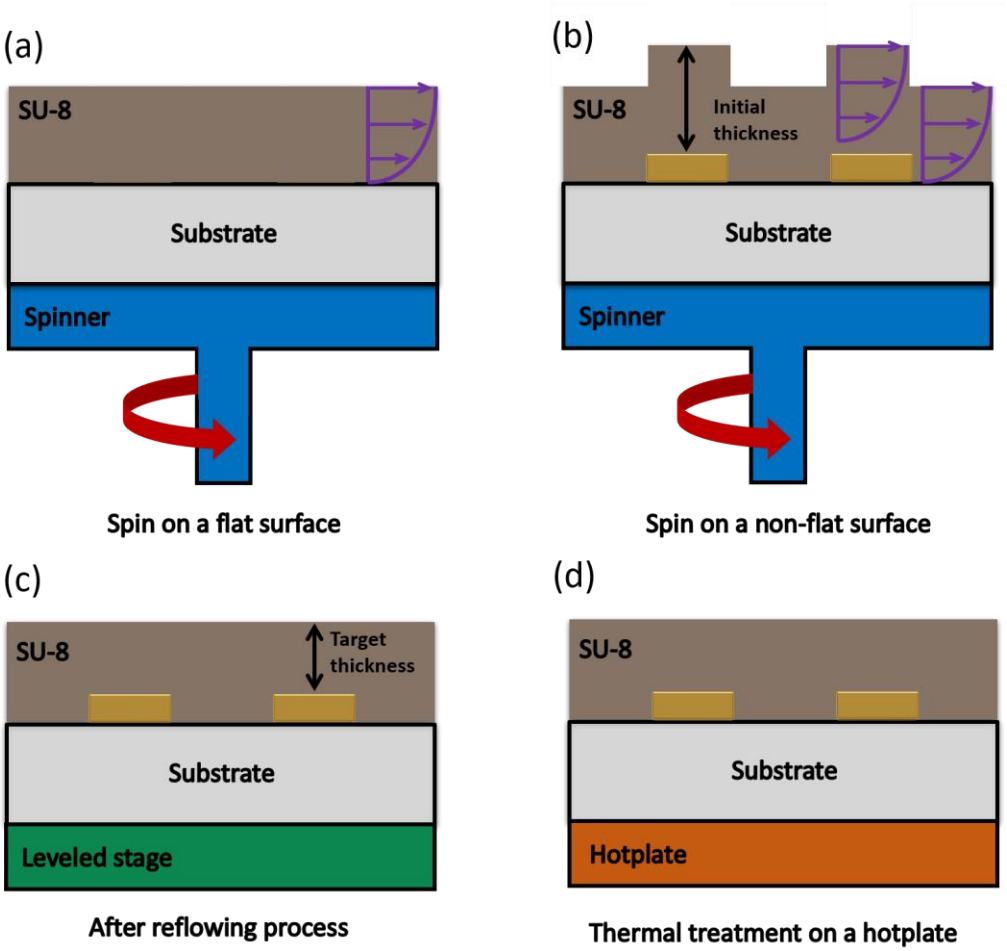

Figure 3.21 Schematic illustration of planarization of non-flat surface. (a) The spin coating on a flat surface, (b) Spin coating on a non-flat surface (c) Reflow process after spin coating (d) Thermal treatment on a hotplate.

SU-8 photoresist has been used to spin coat and planarize topographic surface with thermal treatment [50], [51]. Figure 3.21 describes the planarization process of SU-8 photoresist with thermal treatment. Prior to spinning, the substrates were washed insolvent and gently with O_2 plasma to remove possible organic contaminants. The spinning was performed in two steps. On the first step, the spin speed was set to 500 rpm with a total step time of 10 seconds. On the second step, the spinner was quickly ramped up to 5000 rpm and remained at that speed for 40 seconds. After the spin coating process, the substrate was then placed onto a carefully leveled stage for 5

mins for reflowing resist, as described in Figure 3.21 (c). SU-8 has a relatively lower viscosity and reflows more easily on the substrate, which ultimately contributes to the self-planarization of SU-8. After that, the substrate was baked at 65 °C for 1 min, followed by baking at 95 °C for 5 min. A prebake is employed to reduce the solvent concentration in the resist and increase adhesion to the substrate and serves to reduce diffusion of the crosslinking promoting photogenerated acid after exposure.

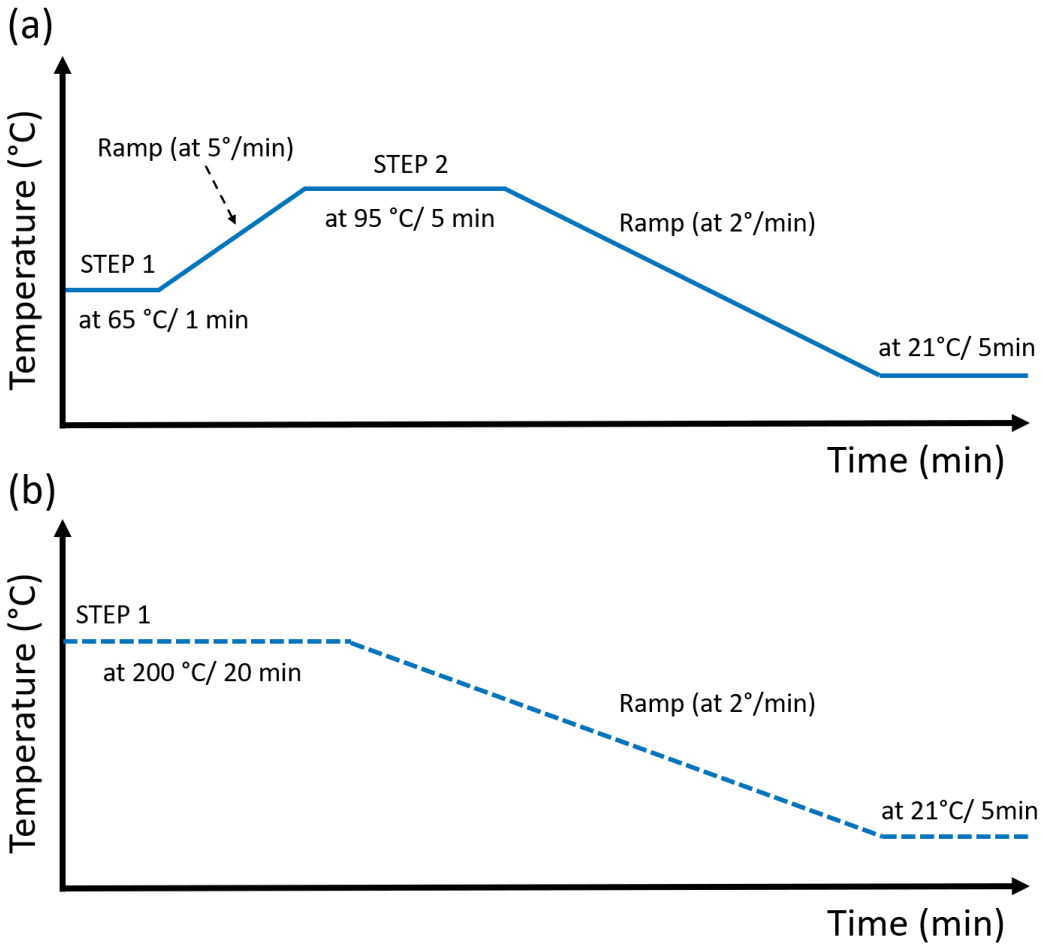

Figure 3.22 The optimized baking profile of SU-8 2000.1 using a leveled hotplate with good thermal control (a) Prebake and postbake (b) Hardbake.

It should be noted that, in order to minimize the residue stress in SU-8 resist, a slow temperature ramp (i.e., at 5 °C / min) is always necessary during the heat-up while the substrate is cooled down naturally to room temperature (21 °C) after the baking process as illustrated in Figure 3.22 (a). The optimum UV exposure dose required for a layer of resist is not only dependent upon its thickness (100 nm) also on the reflectivity of substrates. i-line UV exposure on the substrate is performed by MA6 over 100mJ/cm^2. Following exposure, the crosslinking process is accelerated with a postbake process as the same baking profile to softbake in Figure 3.22 (a). It is noted that the development was not needed at this stage. A harbake can be performed to increase the hardness, and chemical resistance of SU-8 resist. This is carried out at 200 °C for 20 min and cooled down naturally to room temperature, as described in Figure 3.22 (b).

The non-flat surface of the nanorod layer prevents stacking by simple serial EBL, development, and metal deposition. Therefore, the surfaces of the nanorod layer were flattened by applying a planarization procedure with dielectric spacers. The multilayered nanostructures were fabricated by two steps electron beam lithography (EBL) and metal lift-off on a glass substrate, as illustrated in Figure 3.23. The glass substrate is cleaned with acetone and isopropyl alcohol (IPA) while sonicating. For clean sidewalls, the bi-layer e-beam resists with 170 nm thick methyl methacrylate (MMA, Microchem) and 50 nm thick polymethyl methacrylate (PMMA, Microchem) are used to define metallic array patterns. MMA and PMMA are soft-baked for 5 min at 180 °C on a hot plate. Since MMA is more sensitive than PMMA for the EBL exposure, the bi-layer gives a larger undercut that avoids coating the sidewall. This larger undercut is helpful in the lift-off process. High-resolution EBL exposure process (EBPG5200, Vistec) at a beam voltage of 100 kV is used to define the patterns, methyl isobutyl ketone (MIBK, 1:3) with cold development

at 5 °C followed. After development, a 3 nm chromium and a 37 nm gold are deposited using electron beam evaporation under high vacuum condition at 10^{-7} Torr with an average deposition

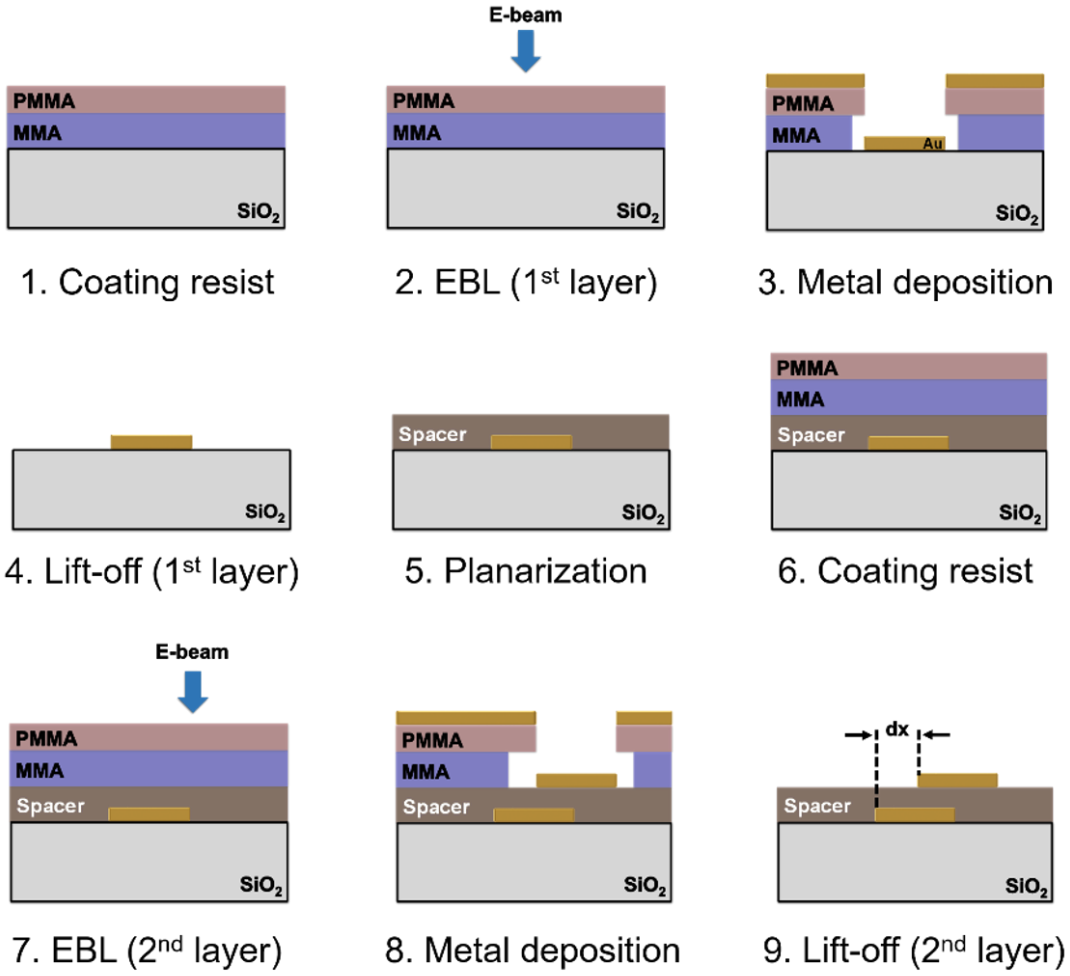

Figure 3.23 Fabrication process of the multilayered plasmonic systems.

rate of 0.1 nm/s. The chromium layer is used as an adhesion layer between the glass and the gold layer. The MMA and PMMA resist are removed by soaking in acetone for 30 minutes at 80 °C.

A 100 nm thick SU-8 2000.1 (MicroChem) is spun over the first metallic layer as a planarized dielectric. The surface of the SU-8 layer is uneven due to the existence of the first layer and is planarized by thermally cycling the sample repeatedly from 65 °C to 95 °C, followed by

SU-8 crosslinking via UV light exposure plus hard baking at 200 °C. The roughness of the surface after planarization is around 2.5 nm. To evaluate the planarization, the roughness of the SU-8 layer.

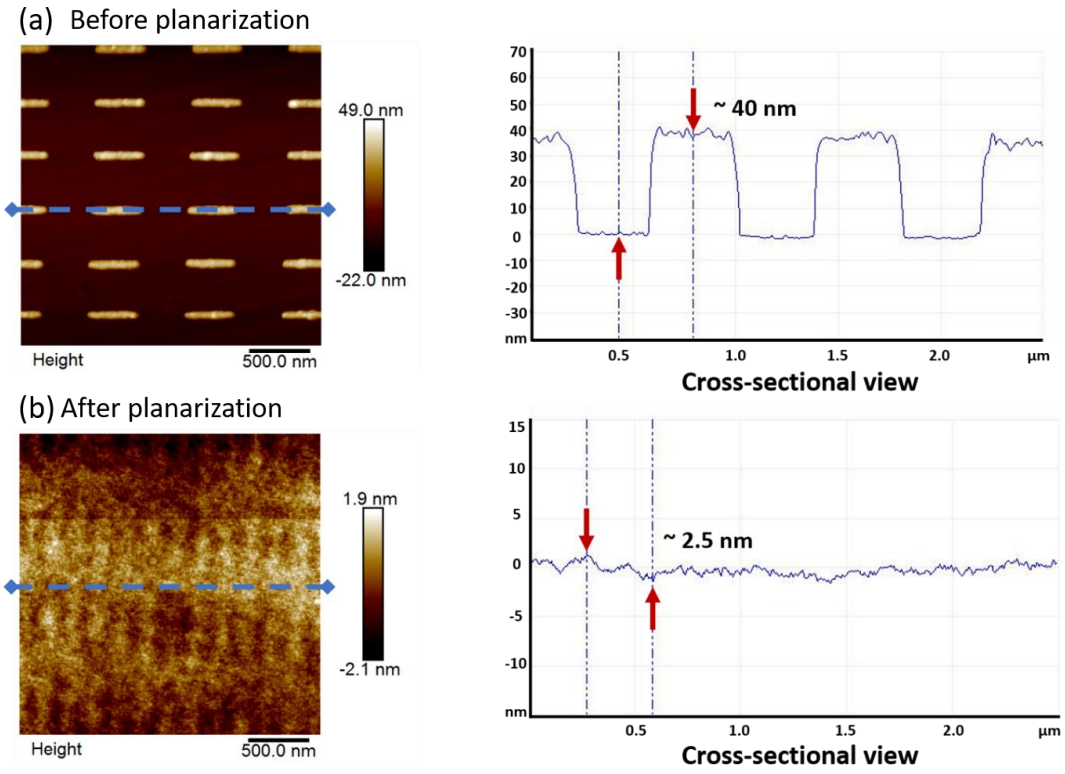

Figure 3.24 Characterization of the structures using an atomic force microscope (AFM) to quantify geometrical parameters (height and surface roughness). (a) Topographical characterization (AFM) before planarization, step (4). (b) AFM image to verify the flatness of the spacer, step (5). The cross-sectional view shows that the root-mean-square (RMS) is around 2.5 nm.

surface was measured using atomic force microscopy (AFM), and the surface roughness (RMS) was found to be around 2.5 nm, as seen in Figure 3.24. MMA and PMMA are spun on the spacer layer and soft-baked for 5 min at 180 °C on a hot plate. A second EBL process is performed using the same method but including a precise alignment step. Metallization and lift-off steps are repeated for the second layer to realize the completed multi-layer structure [52]–[54]. Figure 3.25 (a). presents the SEM images of fabricated multilayered structure with a normal incidence view, which indicates excellent lateral overlay accuracy between different nanorod layers. Figure 3.25

(b) shows an oblique angle view, representing the high quality of the nanorod structures. An enlarged oblique view is shown in Figure 3.25 (c) in which the underlying nanorods are clearly visible, proving that the planarization and the second EBL lift-off fabrication have been successfully performed by optimized multilayer EBL technique.

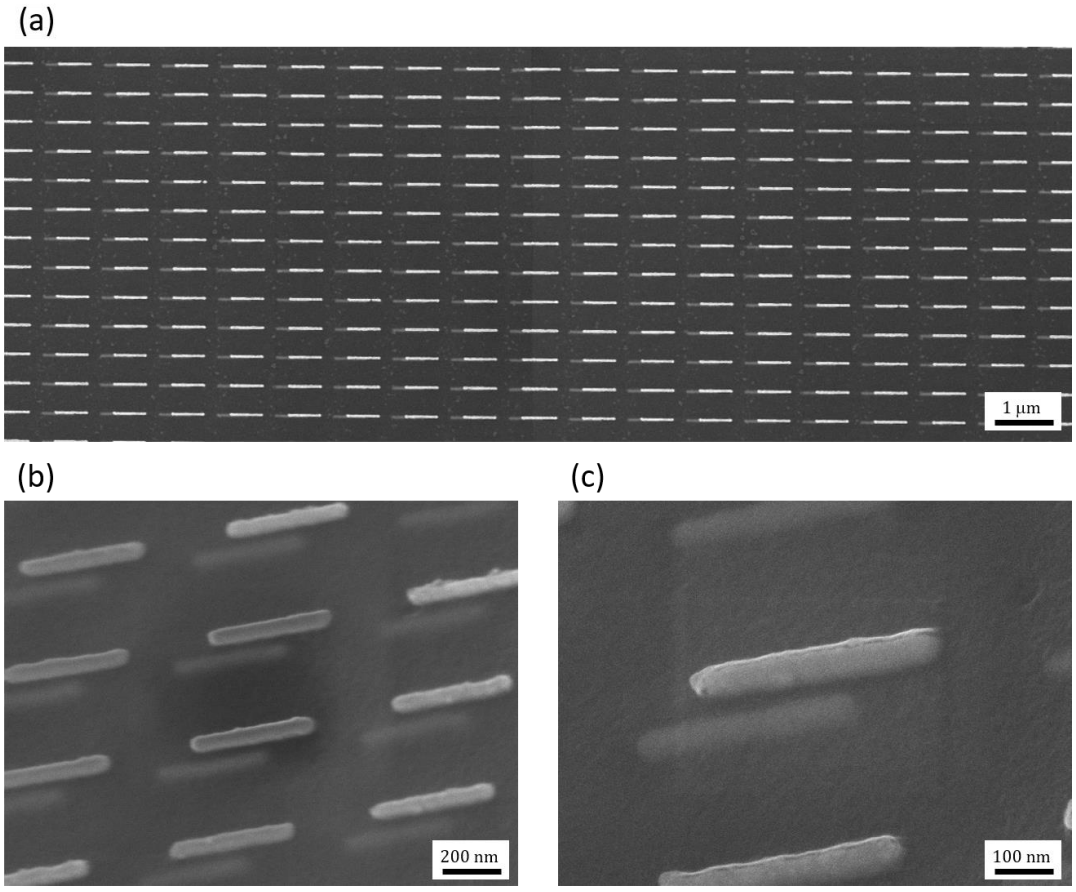

Figure 3.25 SEM images of the fabricated multilayered plasmonic nanostructure. (a) Normal incidence overview. (b) Oblique incidence view (c) Enlarged oblique view.

3.7 Conclusions

In this chapter, we discuss several methods to improve the quality of nanostructure-based on nanofabrication techniques such as cold development and bi-layer resists for EBL and lift-off process. As a consequence, the sidewall roughness of the plasmonic nanostructure is significantly reduced. The precise alignment techniques for the overlay process in EBL allows novel types of

plasmonic structures. This will provide a new platform toward 3D nanostructure for various applications.

Chapter 3, in part, is a reprinted of the materials as it appears in J.-H. Park, A. Kodigala, A. Ndao, and B. Kanté “Hybridized Metamaterial Platform for Nano-Scale Sensing”, *Opt. Express*, **25**, 15590 (2017). This work was co-authored by the dissertation author was the primary researcher and author of this paper.

CHAPTER 4: Hybridized plasmonic sensing platform

4.1 Introduction

In this chapter, we will introduce a new sensing platform to enhance the sensitivity of sensors. At first, a fundamental investigation of localized plasmon resonance is presented. Localized surface plasmonic resonance (LSPR) sensors have become one of the most prominent features of plasmonic nanostructures in terms of practical platforms such as the detection of biomolecules, the measurement of gas concentration, and a monitoring chemical reaction [55]–[59]. The greatly enhanced electromagnetic fields surrounding the surface of a resonant plasmonic structure allow the detection of tiny changes in its local nanoscale dielectric environment. The sensing volume of plasmonic nanostructures is slightly larger than the structure makes it possible to probe the local changes in the surrounding medium. Such enhancement and confinement nature make plasmonic platform low-cost point-of-care (PoC) diagnostic devices [60] due to the integration of the microfluidic device with plasmonic arrays for probing refractive index changing and surface binding events ‘on-chip’ [61].

Subsequently, the new sensing platform to enhance the sensitivity and resolution performance is introduced. It is based on the plasmon hybridization in the multilayered structure. Compared to the conventional LSPR sensor, the hybridized sensing platform allow for much more sensitive detection of the presence of the cladding layer. Finally, the experimental results prove the plasmon hybridization scheme and their inversion process by introducing lateral displacement (d_x) and improved sensing capabilities for refractive index detection.

4.2 General Principle of LSPR Sensing

The sensing performance of the plasmonic system can be quantified by considering the spectral position of the resonances to the refractive index of the surrounding medium. Figure 4.1 represents the principle of plasmonic sensing. An increase in the refractive index of surround

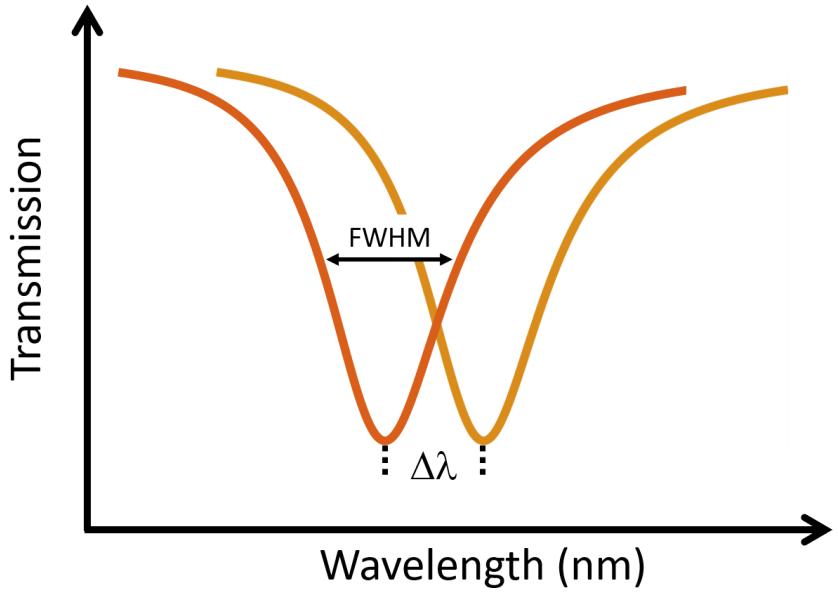

Figure 4.1 Principle of plasmonic sensing. Transmission spectra for the plasmonic sensing system. Definition of resonance shift (Δλ), Full-width-half-maximum (FWHM), and change in refractive index (Δn).

medium results in the redshift of the plasmon resonance. The optical response clearly defines resonance wavelength (λ_{LSPR}) and full-width-half- maximum (FWHM). These spectral shifts (Δλ) can be detected and give information on the change in the analyte. The sensitivity can be extended from the detection of local refractive index changes by the chemical surface modification process of metal nanoparticle, so-called biofunctionalization. This allows for selective detection of a certain molecule concentration [62]–[64]. Figure 4.2 shows bulk refractive sensing verse molecular sensing by LSPR. The highly localized sensing volume allows one to observe molecular

interactions near the nanoparticle surface. For molecular sensing, the change to the surrounding environment is confined to the sensing volume, whereas, the electric fields are extended from nanoparticle for bulk refractive index sensing. The electric field enhancement in Figure. 4.2 (c, d) for a nanorod shows the very small sensing volume due to the strong field localization. Thus, the LSPR sensor is the best candidate for selective molecular detection.

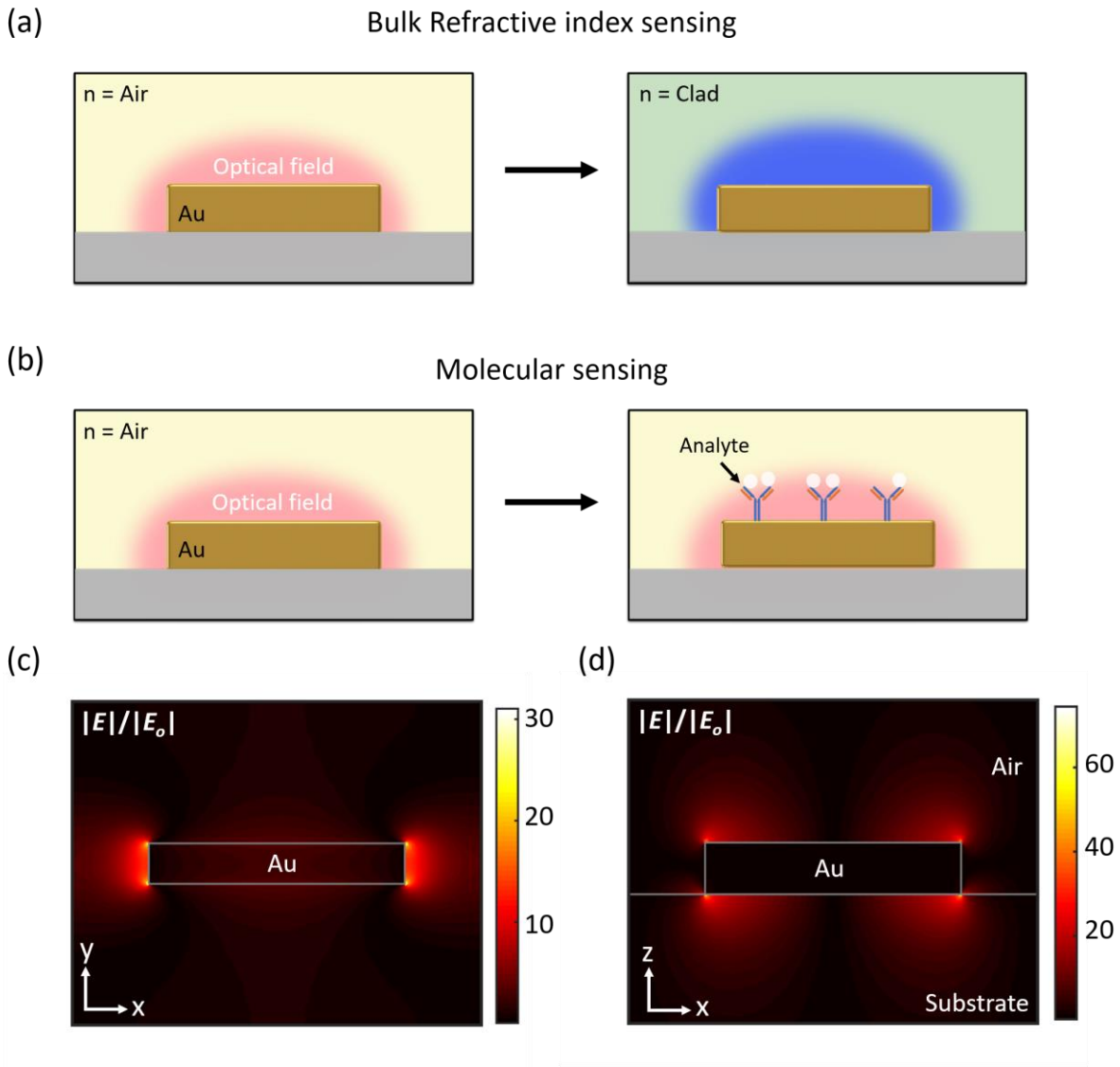

Figure 4.2 The contrast between bulk refractive index and molecular LSPR sensing and simulated E-field enhancement of a gold nanorod. (a) Bulk refractive index sensing (b) Molecular sensing (c) E-field enhancement (top-view) (d) E-field enhancement (cross-section view). Nanorod structure parameter: L = 250 nm, W = 50 nm, and t = 40 nm.

4.3 Refractive Index Sensing with LSPR

The ability of plasmonic nanostructures is typically expressed in terms of their bulk sensitivity (*S*), which is defined as the ratio of resonant wavelength shift (Δλ) to the variation of the surrounding refractive index (Δn, RIU). A figure-of-merit (FOM) obtained by dividing the bulk sensitivity by the resonance linewidth is widely used to characterize LSPR sensing capabilities. This quantity determines the overall performance of the sensor [65].

$$S = \frac{\Delta\lambda_{LSPR}}{\Delta n} \text{ [nm/RIU]} \quad (4)$$

where RIU is refractive index unit.

$$FOM = \frac{S}{\Gamma} \quad (5)$$

where Γ is full-width-half-maximum.

Figure 4.3 displays the schematic illustration of a unit cell of a single nanorod to investigate the sensing capabilities of refractive index variation. The cladding layer with a thickness (h_c) covers the top of a nanorod. The simplest sensing application of the LSPR sensor is to detect the changes in the bulk refractive index of their environment. Two physical parameters, cladding layer index (n_c) and thickness, are considered to evaluate sensing capabilities. The cladding refractive index (n_c) variation with constant h_c = 70 nm exhibits linear dependence of LSPR wavelength shifts in Figure 4.4 (a). LSPR with high refractive index environment experiences broadens linewidth due to the radiative damping, as seen in Figure 4.4 (b). The dependence of cladding layer thickness (h_c) is summarized in Figure 4.4 (c, d). The cladding refractive index is kept at 1.4 for LSPR shift evaluation. The LSPR wavelength shifts reach the limitation of approximately 210 nm when h_c is higher than 100 nm. The results are clearly seen in the transmission spectral in Figure 4.4 (d). Therefore, the detection of the high thickness of cladding is hard to differentiate in the

sensing process with the same refractive index. It is desirable to measure the LSPR wavelength shift with cladding thickness less than 2.5 times of a nanorod thickness for analyte identification.

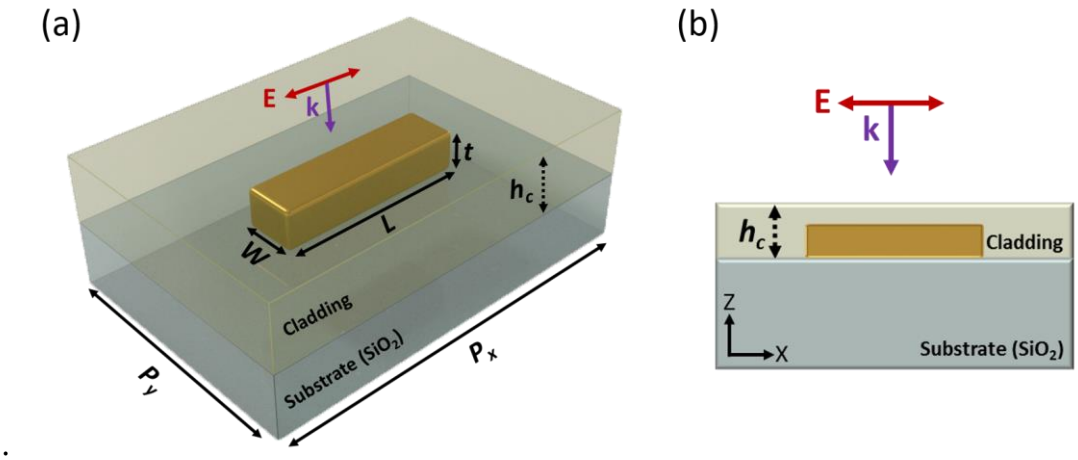

Figure 4.3 Schematic illustration of a unit cell of a single nanorod with a cladding layer (h_c). (a) 3D image of unit-cell (b) Cross-section view.

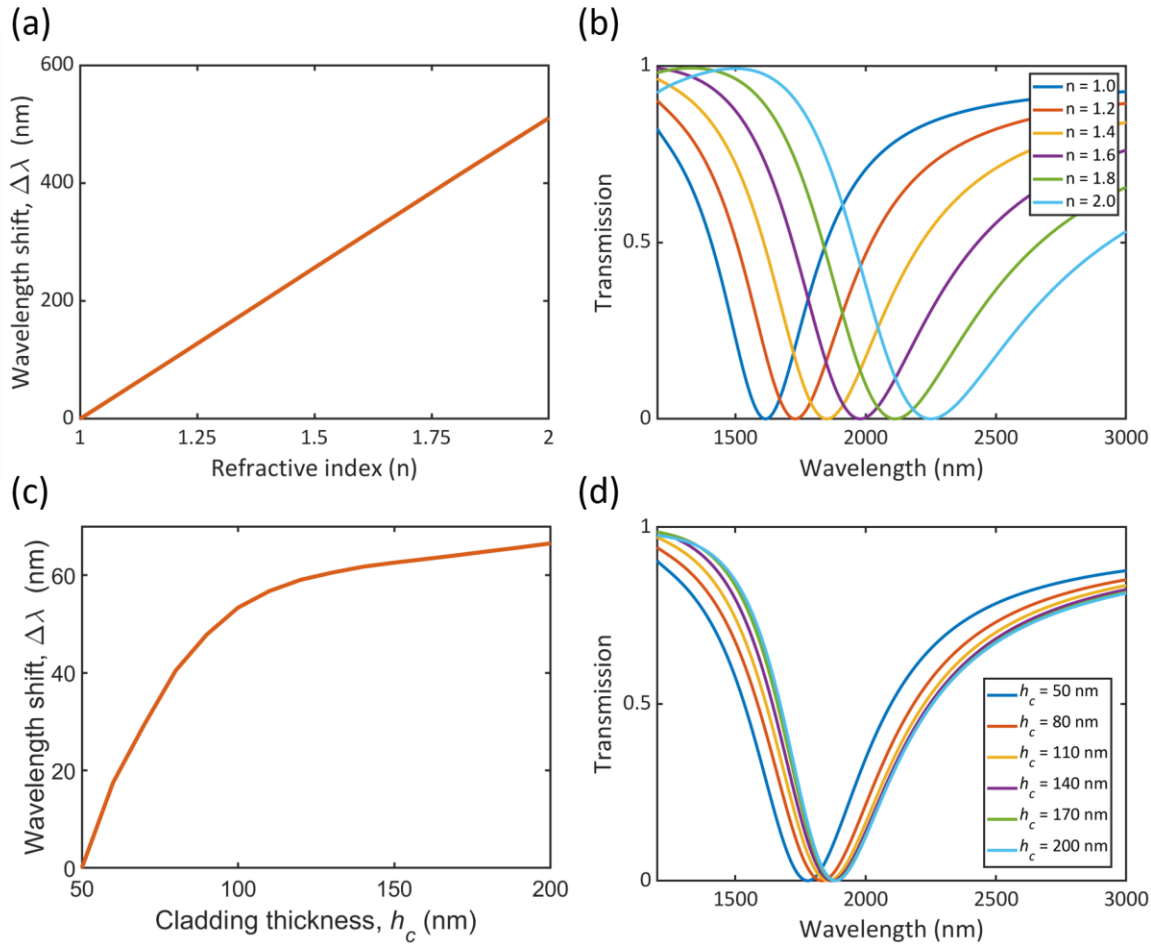

Figure 4.4 Dependence of the LSPR shift on the cladding layer. (a, b) Refractive index variation (c, d) Cladding layer thickness variation.

The LSPR spectral shift is strongly dependent on the dimension of a nanorod. The width of a nanorod is chosen to evaluate the LSPR properties and their sensing capabilities. The simulation is performed on the width variation from 30 to 150 nm with constant parameters as defined in Figure 4.5 , L = 250 nm, t = 40 nm, h_c = 70 nm, and n_c = 1.4, respectively. Figure 4.5 (a,b) summarizes the dependence of LSPR shift on change in the width of a nanorod. An increase in width indicates increasing aspect ratio (length divided by width) simultaneously. Smaller width (i.e., higher aspect ratio) exhibits a larger wavelength shift due to the stronger dipole moment influencing the surrounding media. In addition, not only bulk sensitivity (S) but also figure-of-

merit are improved with the increasing aspect ratio, as seen in Figure 4.5 (c, d). Bulk sensitivity is increased to 2.5 times than the lower aspect ratio. Interestingly, FOM is increasing to 4.4 times than the lower aspect ratio. This is because resonance linewidth also varies with the width of a nanorod. Spectrally narrow linewidth in smaller width contributes to the enhancement of FOM.

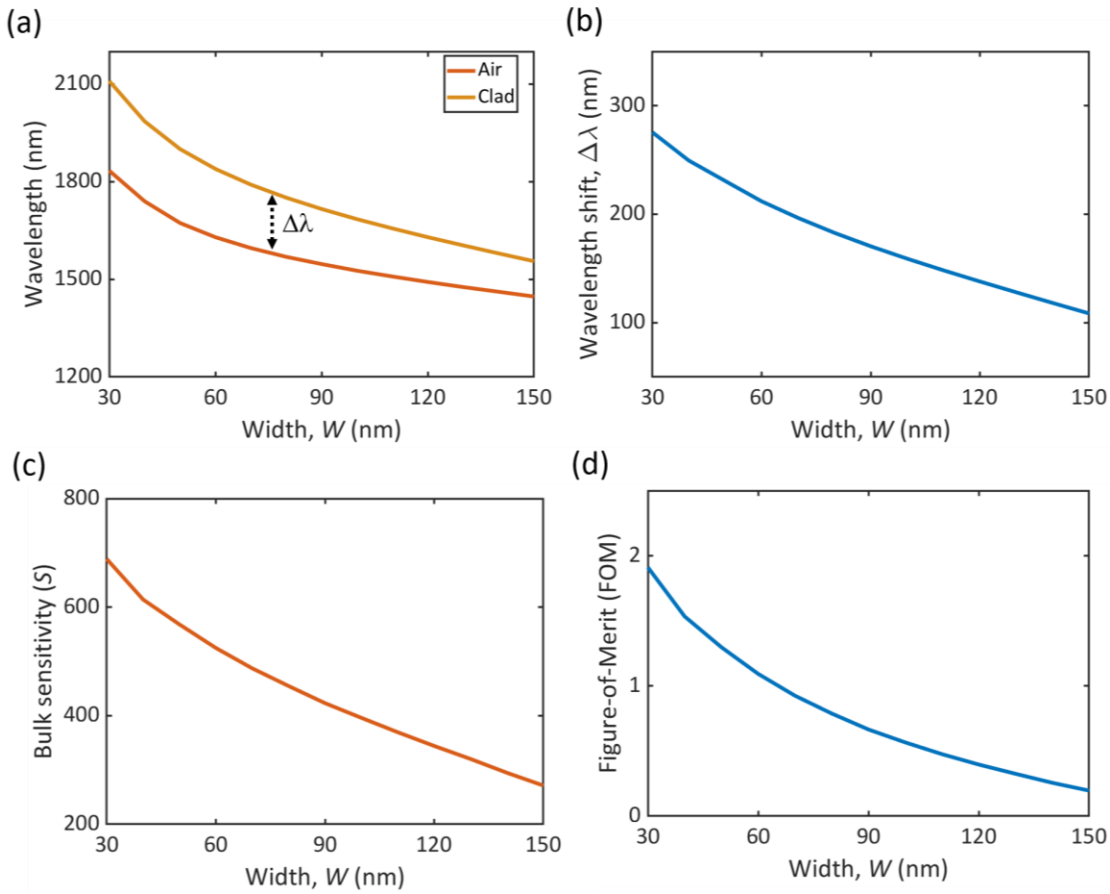

Figure 4.5 Dependence of the LSPR shift on the dimension of a nanorod. (a, b) LSPR wavelength shift (c) Bulk sensitivity (d) Figure-of-Merit (FOM).

4.4 LSPR Sensing Experiment

The behavior of a single plasmon resonance based on the single-layer structure is investigated in the experiment. Two different polymers are deposited by way of spin-coating and cladding layer thickness (h_c = 70 nm), each with different refractive index respectively: PMMA

(n_c = 1.4778) and MMA (n_c = 1.4118). As seen in Figure 4.6, the interaction between the surrounding medium (PMMA and MMA) and the near field significantly affects the resonance wavelength of the fundamental mode (single layer metallic bars). Figure 4.6 presents the reflection spectra recorded for three different surrounding refractive indices (n_{air} = 1.0, n_{PMMA} = 1.4778, n_{MMA} = 1.4118) for both numerical simulation (left column) and experiment (right column). We

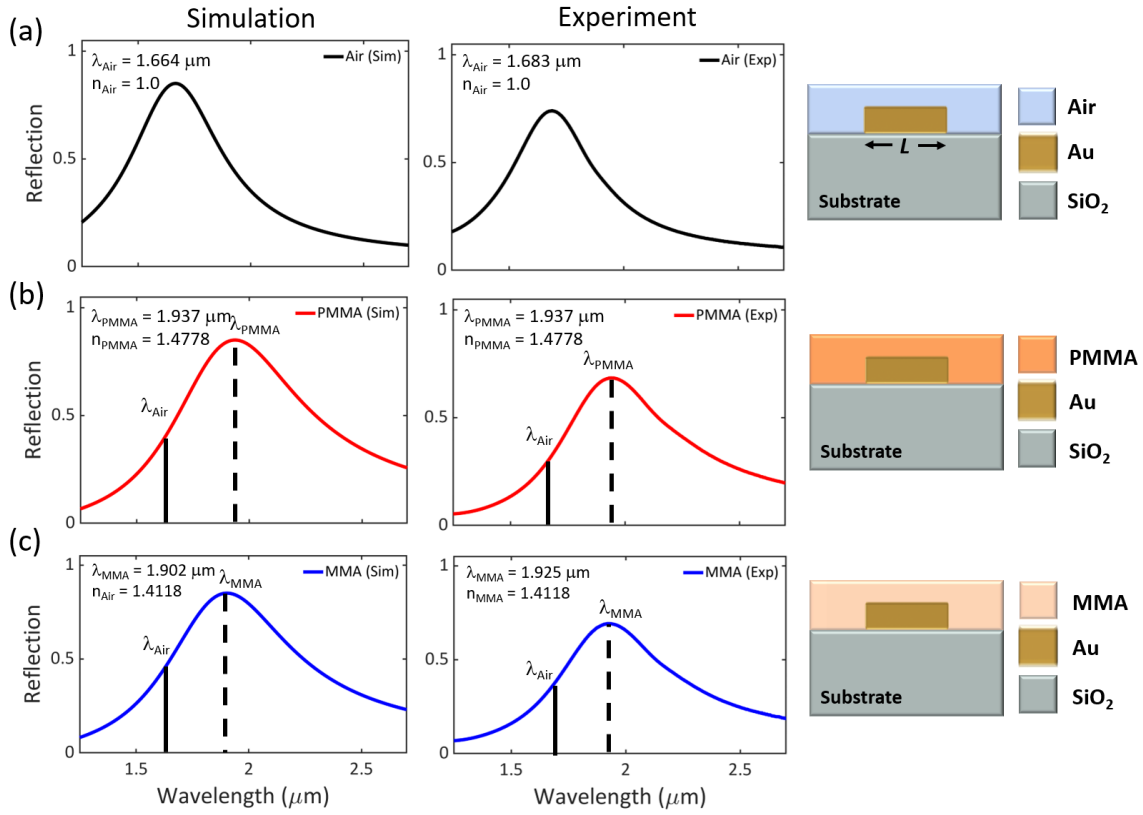

Figure 4.6 Dependence of the resonance frequencies on the cladding medium on top of the single-layer system. (a) Reflection spectra of a nano-bar structure without cladding media. (b), (c) Dependence of the resonance wavelength for different cladding media: (b) PMMA and (c) MMA.

experimentally observe that the presence of a refractive index greater than that of air redshifts the resonance by $\Delta\lambda$ = 260 nm for PMMA (Δn = 0.4778) top- cladding and by $\Delta\lambda$ = 242 nm for MMA (Δn = 0.4118). The linewidth of the single-layer dipolar resonance is ~ 640 nm.

Experimental and numerical data are in good agreement in terms of the resonance position and amplitude. The performance of this rudimentary sensor is also evaluated, and the calculated the bulk sensitivity for PMMA and MMA is 544 nm/RIU and 587 nm/RIU, respectively. The FOM in both cases for the single-layer structure are: $FOM_{PMMA} = 0.85$ and $FOM_{MMA} = 0.91$. In comparison, the sensitivity values acquired from simulated scattering spectra are 571 nm/RIU with PMMA and 578 nm/RIU with MMA. The difference in the sensitivities arises from both the fabrication imperfections and the penetration of the field in the material to sense.

4.5 Hybridized Sensing Platform for Enhancing LSPR

As pointed out in the previous section, the figure-of-merit is improved by reducing the resonance linewidth (i.e., FWHM). The broad linewidth of plasmon resonance limits the sensing properties fundamentally. An effective way of decreasing the linewidth is to arrange plasmonic nanoparticles into a defined geometry. Coupling effects may occur and can significantly decrease linewidth of the plasmonic resonance. One way to achieve this is to place plasmonic resonance in proximity to one another leading to plasmon hybridization. The characteristic of magnetic resonance exhibits non-radiative nature, as discussed in Chapter 3. This hybridized mode properties can be employed in sensing applications to obtain a greatly increased FOM compared to the simple dipolar plasmonic structure in the same spectral range [66]–[69].

To evaluate the sensing capabilities of the plasmon hybridization sensing platform, the multilayered structure is considered as seen in Figure 4.7. Two stacked nanorods configuration gives rise to plasmon hybridization due to the coupling between nanorods. For the investigation of sensing performance, the cladding layer with the thickness (h_c) is fully covered on the top layer.

The lateral displacement of an upper nanorod along the *x*-axis is introduced to the invert hybridization scheme, as discussed in Chapter 3.

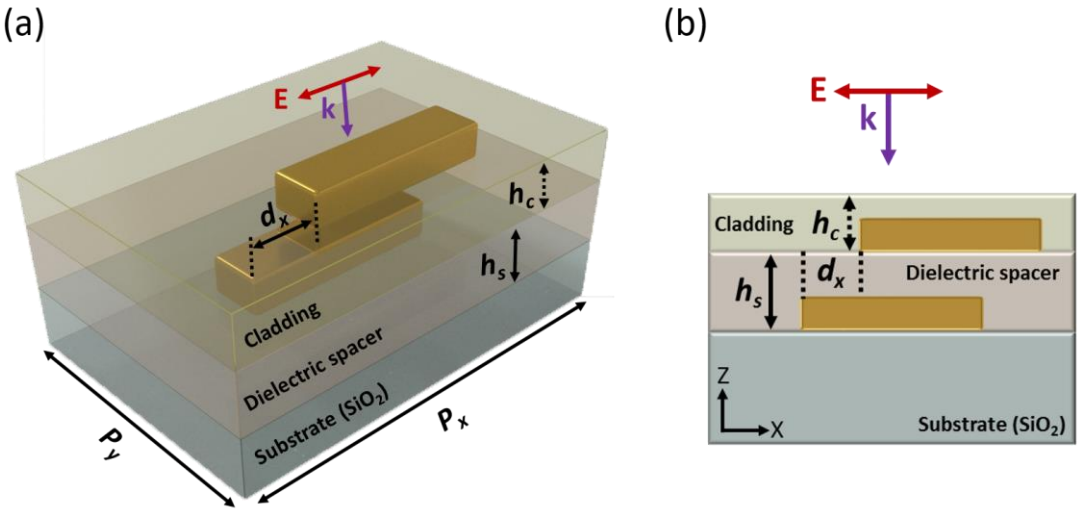

Figure 4.7 Schematic illustration of a unit cell of multilayered structure with cladding layer (h_c). (a) 3D image of a unit-cell (b) Cross-section view.

Figure 4.8 shows the sensing capabilities of the plasmon hybridization system by increasing the cladding index with constant cladding thickness (h_c) = 70 nm. Due to the strong absorption associated with antisymmetric mode (ω_-), the surrounding cladding layer strongly interacts with the resonance. Consequently, the LSPR peak of antisymmetric modes is pronounced, whereas the symmetric mode is inefficiently interacting with respect to the increasing cladding index, as shown in Figure 4.8 (a, b). LSPR shift of antisymmetric mode exhibits linear dependence on cladding index variation. Additionally, the LSPR shift of antisymmetric mode is nearly constant to lateral displacement (d_x). This means wavelength shift ($\Delta\lambda$) of the fabricated sensor can be insensitive to fabrication imperfection in terms of lateral displacement. Another critical parameter of the sensing platform, Figure-of-Merit (FOM) values are also calculated as 0.2 and 5.2 for symmetric and antisymmetric modes when lateral shift 0 nm and 400 nm, respectively. The

enhanced FOMs for two hybridized modes are obtained at different lateral shift values due to the opposite radiative nature of resonance modes with respect to the geometric parameter d_x. The narrow linewidth of antisymmetric mode is observed at d_x = 400 nm, whereas, without lateral displacement, d_x = 0 nm brings about minimum full-width-half-maximum. The FOM values of the two modes are not affected by the change in the cladding index.

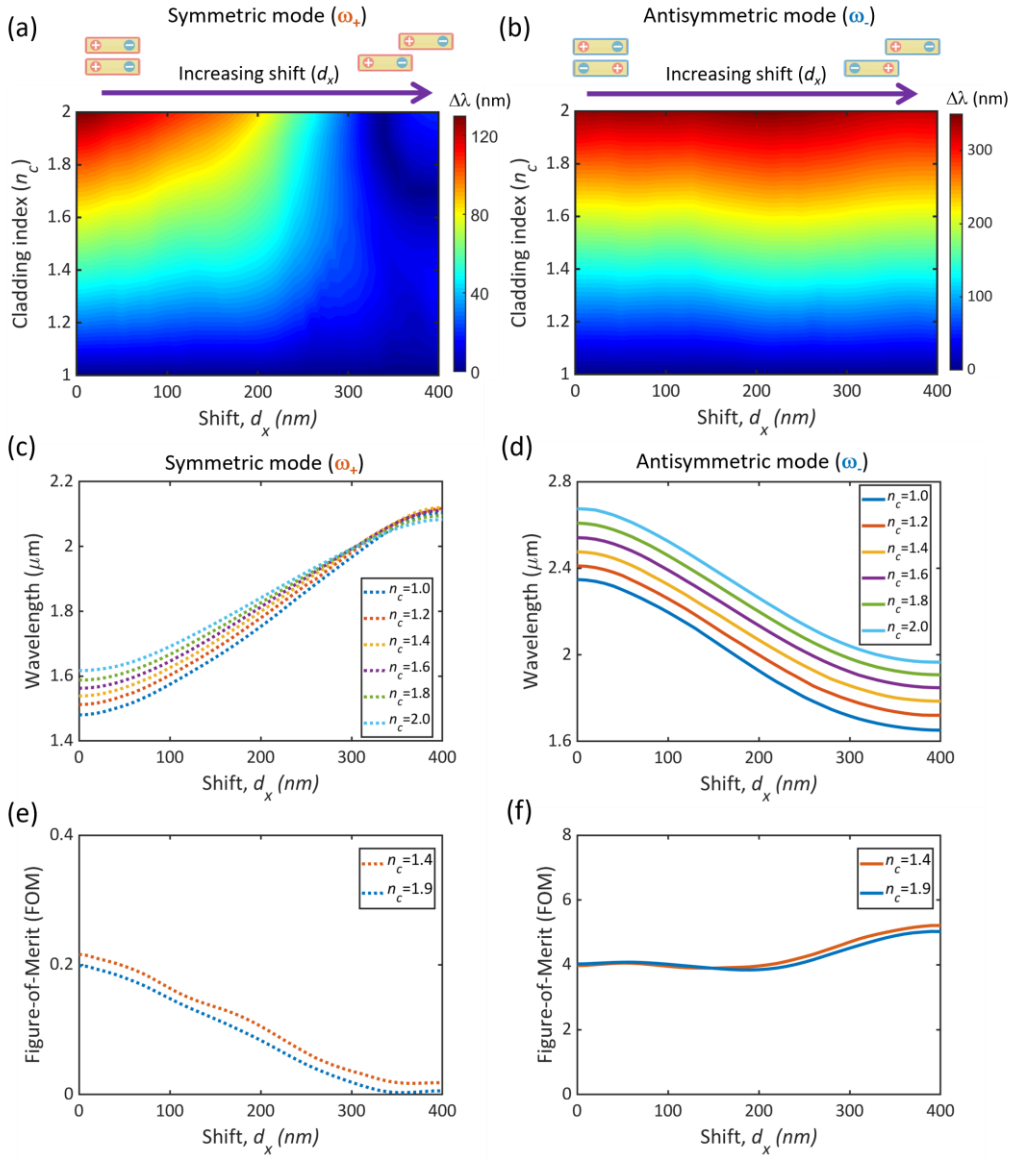

Figure 4.8 Sensing capabilities of hybridized modes with cladding index variation. (a, b) Wavelength shifts of two hybridized modes, symmetric and antisymmetric mode, respectively. (c, d) Resonance wavelength of hybridized modes for different cladding index (e, f) Figure-of-Merit of two hybridized modes.

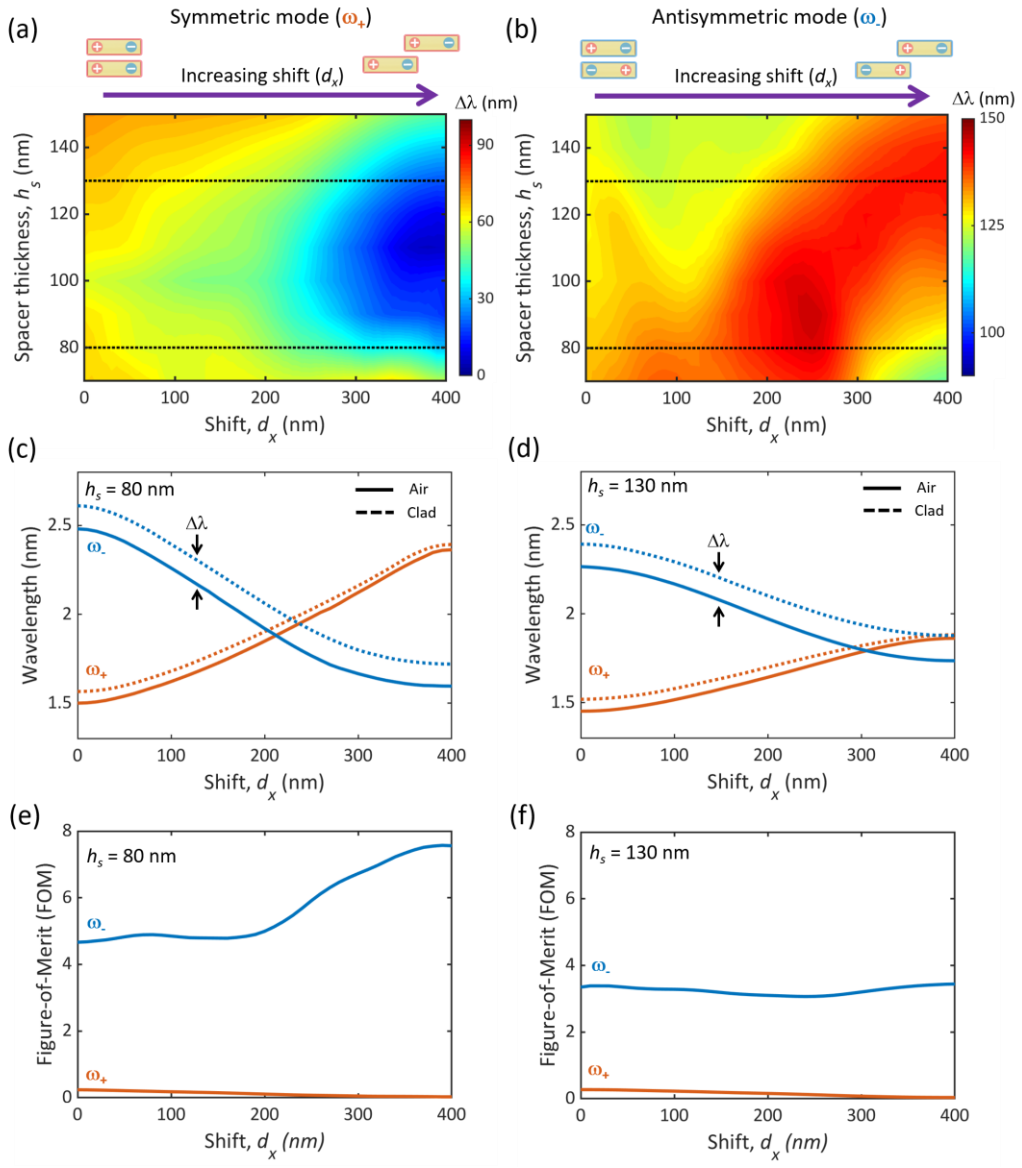

Figure 4.9 Sensing capabilities of hybridized modes with spacer thickness variation (a, b) Wavelength shifts of two hybridized modes, symmetric and antisymmetric mode, respectively. (c, d) Resonance wavelength of hybridized modes for two different h_s. (e, f) Figure-of-Merit of two hybridized modes.

The sensing capabilities on the geometrical parameter, spacer thickness (h_s) is investigated while keeping n_c = 1.4 and h_c = 70 nm to evaluate the plasmon hybridization sensing platform. Figure 4.9 displays the dependence of LSPR wavelength shifts and FOM on space thickness variation. The results show that the LSPR shifts for antisymmetric mode are very pronounced

compared to symmetric mode, as seen in Figure 4.9 (a - d). The FOM value of antisymmetric mode for h_s = 80 nm increases after hybridization inversion at the shift of d_x = 200 nm. This implies the linewidth of mode is significantly reduced past hybridization schemes. The maximum value of FOM is calculated as 7.6, which is a two-fold enhancement to h_s = 130 nm in Figure 4.9 (e, f). Strong near-field interaction between two stacked nanorods at h_s = 80 nm attributes to the enhancement of sensing performance. For h_s = 130 nm, the inversion of the hybridization scheme with the cladding layer is not achieved with lateral displacement. The presence of the cladding layer leads to lowered near-field interaction between two nanorods.

4.6 Hybridized Sensing Experiment

To evaluate the sensing capabilities of the plasmon hybridized sensing platform, we choose nanorod having a thickness of 40 nm, a length of 450 nm, and a width of 50 nm. The material of the dielectric spacer is the SU-8 with a refractive index $n_{SU\text{-}8}$ = 1.57 and a layer thickness of 100 nm due to the optimized fabrication process. The unit-cell size of the nanorod array is 800 nm x 400 nm, which is well below the distance where Wood anomalies induce a problem [70].

First, we optically characterize the fabricated sample without sensing material to prove simulation and fabrication steps. Figure 4.10 summarizes the simulation (left column) and experimental (right column) results accompanied by SEM images (middle column) for single layer and multilayer structures with varying shifts, d_x. Figure 4.10 shows numerical and experimental spectra for a single layer of gold bars on a glass substrate with a single observed resonance at 1.64 μm (182.8 THz), which corresponds to the fundamental localized plasmon resonance on an individual bar. This is slightly different from a fundamental resonance of 1.67 μm with ideal geometrical parameters. To better compare the numerical simulations and the experimental results,

we simulated the geometrical parameters extracted from the SEM images of each sample for a direct comparison with the experimental results. There is a quantitatively excellent agreement between the numerical simulations and the experimental results for both reflection and transmission in terms of the location of the resonance and the amplitude of the resonance. This validates the quality of the fabricated single-layer structures.

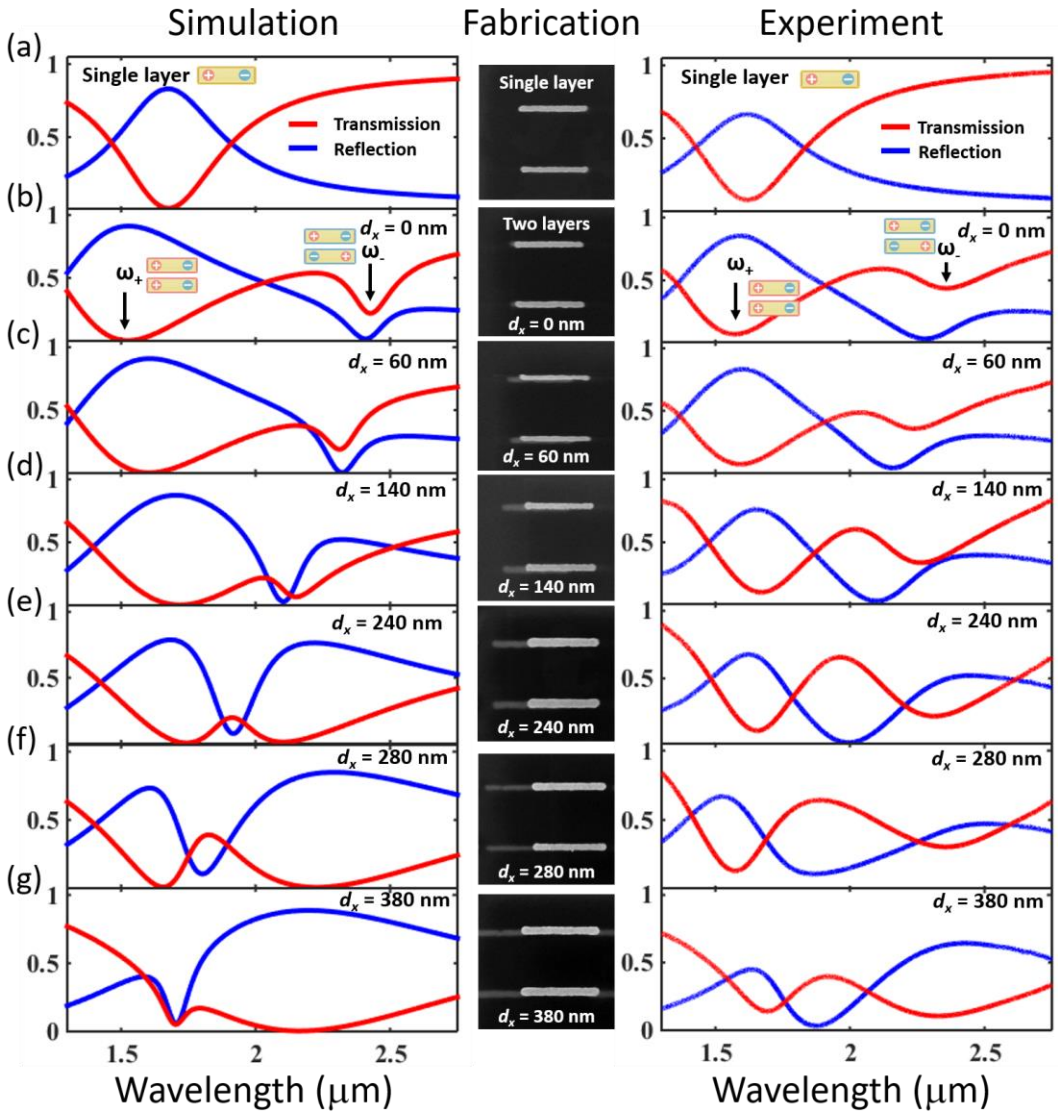

Figure 4.10 Simulation and experimental results for a single layer and a multilayer structure with varying shifts, d_x. (a) The single plasmon resonance of a single layer (b-g) Multilayered structures with hybridization (symmetric mode, ω_+, and antisymmetric mode, ω_-) with shift, d_x: (b) d_x = 0 nm, (c) d_x = 60 nm, (d) d_x = 140 nm, (e) d_x = 240 nm, (f) d_x = 280 nm, (g) d_x = 380 nm.

Figures 4.10 (b-g) correspond to the numerical and experimental results for the multi-layer structures for varying values of the shift, d_x. From Figure. 4.10 (b), it is seen that the spectrum of transmission and reflection comprises two main hybridized resonances as expected: symmetric (ω_+) and antisymmetric (ω_-) modes. The symmetric mode resides at a higher frequency (smaller wavelength), and the antisymmetric mode resides at a lower frequency (higher wavelength). This splitting of the resonances corresponds to a coupling of the plasmon resonances of the different layers, which leads to a lifting of the degeneracy of the fundamental mode. Figures 4.10 (b–g) show the existence of these two resonances in all cases (represented by vertical arrows in Figure. 4.10 (b)).

With the increasing shift, d_x, we observe experimentally that the antisymmetric mode moves down in wavelength. In contrast, the symmetric mode moves up in wavelength as expected (physical shift seen in Figure 4.10). This is best observed from the quantitative resonances extracted from the scattering parameters for both the simulation and experiment. There is an observable inversion between the symmetric and antisymmetric modes past a shift of 'd_x = 240 nm', indicating strong near-field coupling. Other all-dielectric platforms may also be used for sensing.

Minor discrepancies in the results are mainly due to fabrication imperfections not accounted for in the simulations such as the slightly rounded edges of the bars, misalignment between layers, and the surface roughness. It is important to note that in practice, it is difficult to obtain a perfect alignment of the bars, and hence the experimental results deviate slightly from the numerical result. The decay rates (i.e., losses) for both the symmetric (i.e., larger linewidth) and antisymmetric (i.e., smaller linewidth) modes are as anticipated. The same is true for the resonance frequencies. Overall, an excellent agreement between the numerical and experimental results is

observed. Plasmon hybridized sensing platform is now established in the form of the shift-bar system.

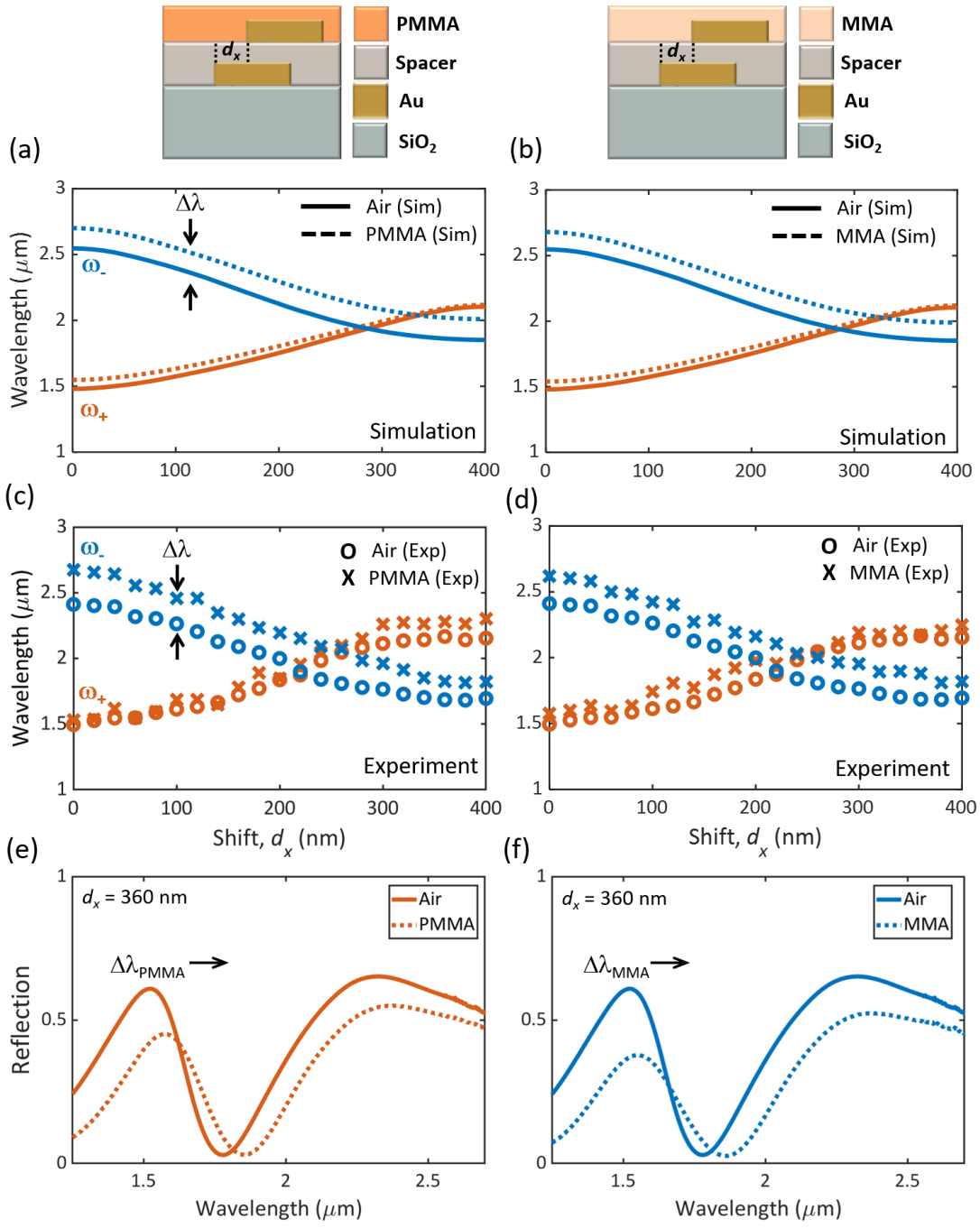

Figure 4.11 Resonance extraction from scattering parameters for both simulations (solid and dash lines) and experiment (circular and cross markers). Numerical simulations for air with PMMA (a) and MMA (b) cladding and Experimental results for air with PMMA (c) and air with MMA (c). (e, f) The measured Reflection spectra of air, PMMA, and MMA at d_x = 360 nm.

Similarly, we evaluate the sensing ability of the hybridized plasmonic system for both the symmetric (ω_+) and antisymmetric (ω_-) modes. As previously stated, there is an observable inversion between the symmetric and antisymmetric modes for shifts, d_x, larger than 'd_x = 240 nm' for resonances extracted from scattering spectra for both simulation [Figure 4.11 (a) and Figure 4.11 (c)] and experiment [Figure 4.11 (b) and Figure 4.11 (d)]. Here, the resonance positions of the two modes are acquired from the complex poles of the fitted scattering parameters. For an added top-cladding of either PMMA [Figure 4.11 (a) and Figure 4.11 (b),], or MMA [Figure 4.11 (c) and (d)], both symmetric and antisymmetric resonances are redshifted. Moreover, the antisymmetric mode is more sensitive compared to the symmetric mode judging from the shift in resonances ($\Delta\lambda$) for both PMMA and MMA cladding irrespective of 'd_x.' In both cases for $d_x = 0$, the experimentally calculated FOMs for the symmetric mode are $FOM_{PMMA} = 0.08$ and $FOM_{MMA} = 0.27$ whereas for the antisymmetric the FOMs are $FOM_{PMMA} = 3.65$ and $FOM_{MMA} = 3.82$. Only the symmetric mode is more sensitive than the single-layer fundamental mode, which has $FOM_{PMMA} = 0.85$ and $FOM_{MMA} = 0.91$. At $d_x = 0$, the linewidths of the symmetric and antisymmetric modes are ~ 830 nm and ~210 nm, respectively. Experimentally, the symmetric mode experiences a resonance shift of 39 nm for PMMA and 110 nm for MMA. Similarly, the antisymmetric mode experiences a resonance shift of 313 nm for PMMA and 250 nm MMA.

Hence, we plot the FOM for the higher sensitivity antisymmetric mode as a function of the shift, d_x, in comparison to the single-layer device for both PMMA [Figure 4.12 (a)] and MMA [Figure 4.12 (b)] top-claddings. We note here that there is a factor of 4 increase in the FOM for the hybridized antisymmetric resonance compared to the fundamental resonance of a nano-bar [71].

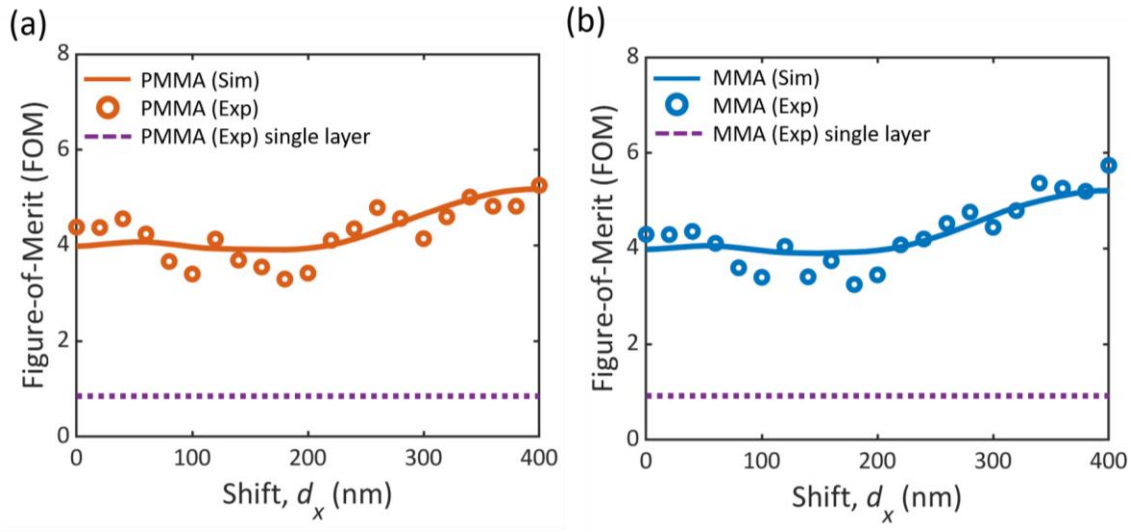

Figure 4.12 Figure-of-merit (FOM) for the multilayer structure as a function of shift, dx. (a) The solid and dashed lines show the calculated FOMs for both simulation and experiment for PMMA cladding and (b) MMA cladding. The dashed green line is the FOM value calculated for a single-layer structure for comparison.

4.7 Conclusions

In this chapter, we introduce the LSPR sensing method and its sensing capabilities. The numerical investigation provides insight to improve sensitivity enhancement and resolution performance of sensors with geometrical parameters such as aspect ratio of a nanorod. We also proposed a novel sensing platform based on plasmon hybridize to get enhanced sensitivity. The sensing capability of a hybridized plasmonic system exhibits a superior sensor to a standard single plasmonic resonance system. The FOM is a factor of 4 higher in the hybridized case using the antisymmetric mode. Furthermore, the antisymmetric mode of the hybridized system has a higher sensitivity and FOM compared to the electric dipolar mode regardless of the shift. A quantitative analysis of the plasmonic resonances allowed for accurate computation of both sensitivity and FOM. Moreover, specificity can be introduced to the current hybridized label-free sensing scheme by functionalizing the gold nanoparticles with appropriate biological or chemical markers. Intricate hybridized metamaterial resonances will usher the next generation of sensing devices.

Chapter 4, in part, is a reprinted of the materials as it appears in J.-H. Park, A. Kodigala, A. Ndao, and B. Kanté "Hybridized Metamaterial Platform for Nano-Scale Sensing", *Opt. Express*, **25**, 15590 (2017). This work was co-authored by the dissertation author was the primary researcher and author of this paper.

CHAPTER 5: Observation of Plasmonic Exceptional Points

5.1 Introduction

Energy conservation is a fundamental physical concept in the Hermitian system whose eigenvalues are real, and eigenstates are orthogonal. The Hermitian Hamiltonian ($H=H^{\dagger}$, where the superscript † denotes Hermitian conjugation) has been considered as the main physical model, such as in quantum mechanics and electromagnetics. However, realistic physical systems interact with the environment, which means the energy is non-conserved open systems. The non-Hermitian Hamiltonian ($H\neq H^{\dagger}$) is a proper description of the energy level of open systems allowing its eigenstates to decay. In the non-Hermitian system, the eigenvalues, in general, are complex, and eigenstates form a nonorthogonal set. The eigenvalues acquire imaginary parts meaning that systems undergo dissipation in the form of radiation or absorption. Therefore, the complex eigenvalues can be clearly accounted for, representing the eigenenergy of a state and its decay rate of real and imaginary parts, respectively.

The remarkable difference between Hermitian and non-Hermitian systems is the spectral degeneracies, merging their eigenmodes with each other. In the case of Hermitian degeneracies known as diabolic points (DPs), the eigenvalues are degenerated, the eigenvectors remain linearly independent, but the corresponding eigenstates are orthogonal. Interestingly, non-Hermitian singularities, so-called exceptional points (EPs) [72]–[74] is not only eigenvalues coalesce at the same points (i.e., both real and imaginary parts), but also their eigenvectors are completely parallel one another. As a consequence, the corresponding eigenstates become identical, giving rise to a collapse of the eigenspace dimensionality at an EP, and the eigenfunctions become defective operator [75].

Recently, non-Hermitian singularities, EPs have been investigated in various fields. The presence of around EP has a dramatic effect on a system altering its physical properties. This leads to a highly non-trivial characteristic compared with the Hermitian degeneracies. The enhanced sensitivity near EP is demonstrated due to the peculiar topology of the system [76]–[79]. Dynamically encircling of exceptional points enable a robust asymmetric transmission in the microwave and optical waveguide [80], [81]. The observation of EPs has so far been restricted to wavelength-scaled systems based on dielectric waveguides and resonators subject to diffraction limits [82]–[84]. No Experiments have also been performed to test EPs in the context of optical gyroscopes, implantable microsensors, linear time-periodic systems, and thermal mapping [79], [85], [86]. While parity-time symmetry prescribes a systematic recipe for implementing EPs, their implementation in subwavelength-scale systems such as plasmonics constitutes a challenge that requires the controlled spatial distribution of loss and gains at extremely small scales beyond current nanofabrication capabilities [87]–[89]. The observation of such non-Hermitian singularities in plasmonics has thus remained elusive and has hampered the investigation of the physics of EPs at smaller scales. In this chapter, we will focus on the implementation of plasmonic exceptional points based on the hybridization of detuned resonators in a multilayered periodic plasmonic structure to reach a critical complex coupling rate that results in the simultaneous coalescence of resonances and loss rates.

5.2 Exceptional Point in Two-Level System

EPs are observable in parameter-dependent eigenvalue problems. Such parameter variation in the complex plane can find points where eigenvalues coincide. To demonstrate it, non-Hermitian 2 x 2 matrix H considered as.

$$H = \begin{bmatrix} \omega_1 - i\gamma_1 & \kappa \\ \kappa & \omega_2 - i\gamma_2 \end{bmatrix} \quad (6)$$

describe a non-Hermitian ($H \neq H^{\dagger}$) two-level system [74] in Figure 5.1 with complex frequency $\omega_1 - i\gamma_1$ and $\omega_2 - i\gamma_2$, where ω is the resonance frequency of the two coupled modes, γ is their decay rate and κ is the coupling strength between the component of systems. The eigenvalues of the system are

$$\omega_{\pm} = \omega_0 - i\chi \pm \sqrt{\kappa^2 + \Gamma^2} \quad (7)$$

where $\omega_0 = (\omega_1+\omega_2)/2$ and $\chi = (\gamma_1+\gamma_2)$, respectively, represents the mean values of resonance frequencies and loss factors, whereas $\Gamma = \delta + i\beta$ with $\delta = (\omega_1 - \omega_2)/2$ and $\beta = (\gamma_1-\gamma_2)/2$ are the differences between their resonance frequencies and loss factors. By variation of parameters, two eigenvalues can generically coincide at an exceptional point where $\kappa^2+\Gamma^2 = 0$, meaning the solutions ($\delta=0$, $\kappa=\mp\beta$) or ($\beta=0$, $\kappa=\mp i\delta$).

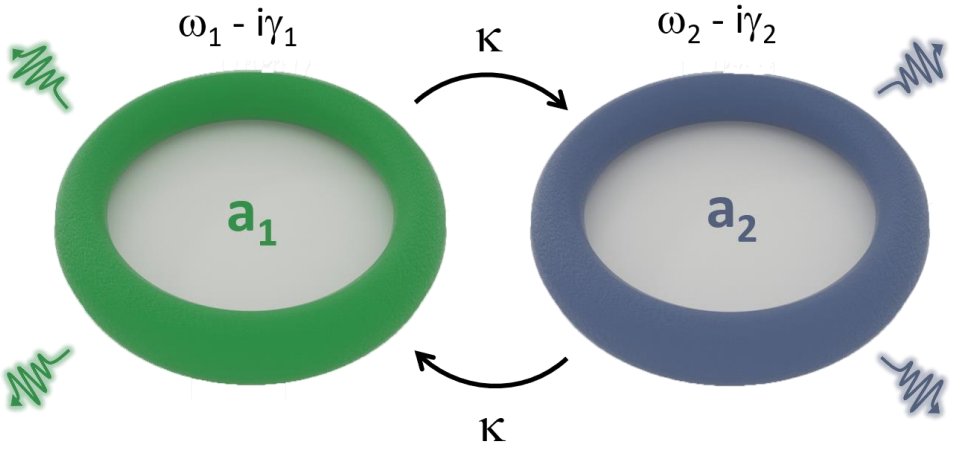

Figure 5.1 Schematic of illustration of the two-level coupled system. ω, γ, and κ represent resonance frequency, loss rate, and coupling strength, respectively.

Figure 5.2 illustrates exceptional points in a non-Hermitian two-level system [90]. The Riemann sheets associated with real (red) and imaginary (blue) parts of eigenvalues shows two coalescing eigenmodes. An exceptional point takes place when the square-root term in Eq.(7) is zero, as the two complex eigenvalues coalesce, as seen in Figure 5.2 (a, b). This happens for real coupling constant assuming $\delta = 0$ and $\beta = \pm \kappa$. The position of an EP can be arranged to lie just above or below the real part of the eigenvalues. Figure 5.2 (c - h) shows a cross-section of the eigenvalue surface in Figure 5.2 (a, b) for different values of β, respectively. Level repulsion takes place in the real parts of the eigenvalues avoided, whereas the imaginary parts of the eigenvalues cross, as shown in Figure 5.2 (c, d). Level crossing real parts of eigenvalues cross, whereas imaginary parts of eigenvalues avoided, as seen in Figure 5.2 (g, h). The switching from level repulsion to the level crossing is affected by the slipping of the EP over the real eigenvalue axis. The EP, where both real and imaginary parts of the eigenvalues coalesce, is achieved with the critical condition ($\beta = \beta_{EP}$) in Figure. 5.2 (e, f). The existence of both the level crossing and level repulsion indeed indicates the EP can be found nearby.

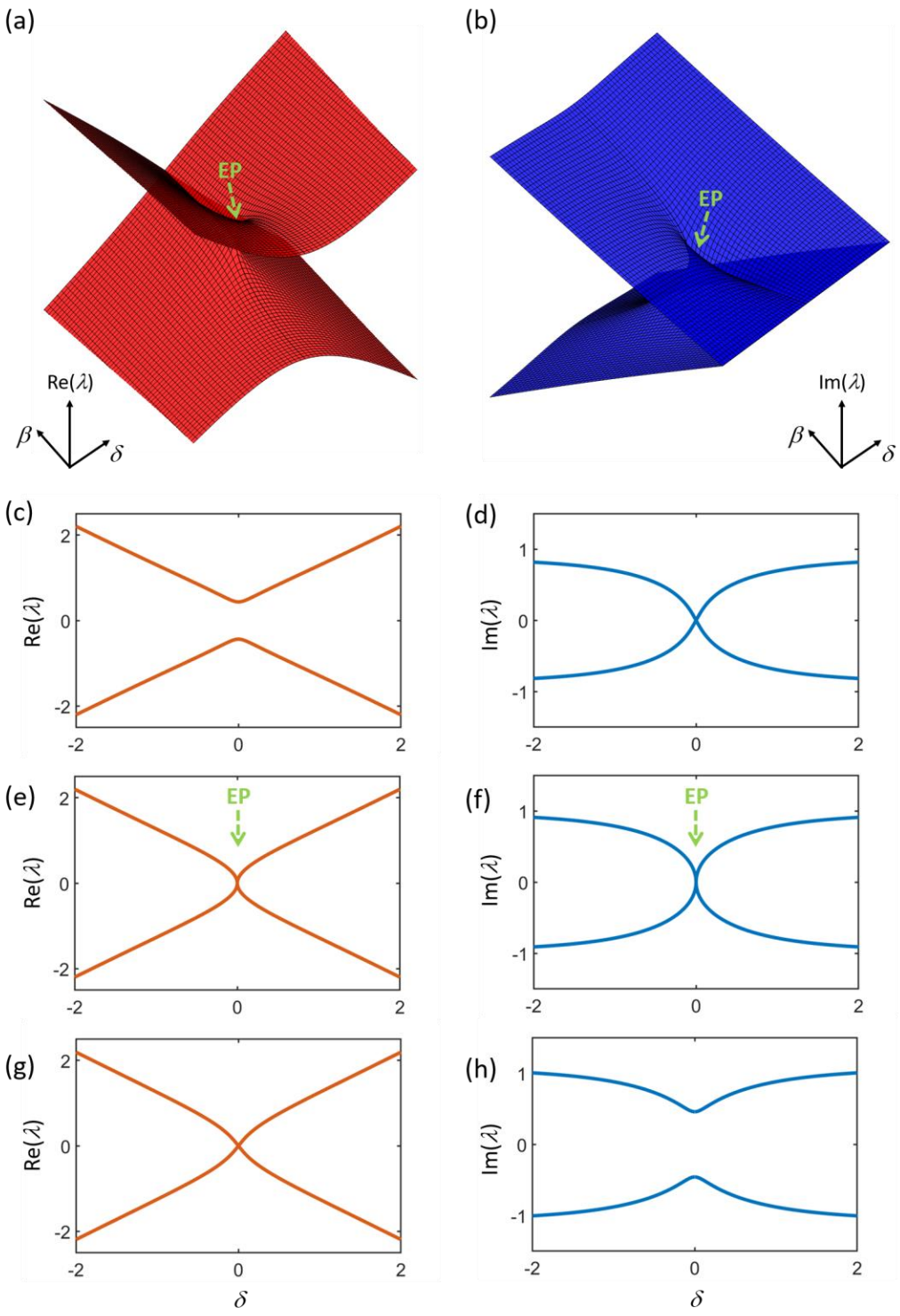

Figure 5.2 Exceptional point in the two-level system. (a, b) The Riemann sheet structure of coalesces of two eigenmodes. (c, d) Level repulsion (e, f) Eigenvalues coalesce at the EP for $\gamma=\gamma_{EP}$ and $\beta=\beta_{EP}$. (g, h) Level crossing.

Non-Hermitian systems in the field of optics and photonics with peculiar phenomena in the vicinity of EP have been demonstrated for the past decade. However, these researches have been restricted to wavelength-scaled systems based on dielectric components such as waveguides and resonators, which are subject to diffraction limits. Plasmonics allows the localization of light field into nanoscale regions and manipulation of light much smaller than the wavelength in the material [91]. Implementing EP in plasmonic media has attracted significant attention recently. There have been several theoretical studies on a platform for EP using *PT*-symmetric plasmonic [92] and coupled nanoantenna with an odd number of resonators [93]. However, no experimental measurement has followed due to challenges in implementing it in a realistic experimental setting. In this section, we will focus on new approaches to achieve EPs in open multimode systems based on the hybridization of detuned resonators in a multilayered periodic plasmonic structure to reach a critical complex coupling rate that results in the simultaneous coalescence of resonances and loss rates.

5.3 Rational Fitting for Frequency Domain Response

The scattering parameters (transmission, reflection) are computed by using a full-wave finite element method using a unit-cell with periodic boundary conditions in the multilayered plasmonic array. We observe two resonances as a result of a coupled resonance system that exhibits asymmetric resonance line-shape features. Due to the asymmetric feature of the resonance system, the quantitative values of the real part of the complex eigenvalues do not simply correspond to transmission dips or reflection peak. The scattering parameters are then fitted to determine the poles of the scattering matrix that are the eigenmodes of the system using a rational function of the form [94], [95]. The fitting transmission curves give us an accurate estimate of the complex

eigenvalues. We extract the resonance frequency and loss rate from the asymmetric resonance line-shape features.

The scattering matrix provides information on the frequency evolution of transmission coefficients.

$$\boldsymbol{F}(\boldsymbol{s}) = \sum_{n=1}^{N} \frac{C_n}{s - A_n} + D, \mathrm{s} = \mathrm{j} * 2\pi\mathrm{f} \tag{8}$$

where A_n, C_n, D are the fitting parameters, and f represents the frequency. The fit yields complex poles corresponding to mode A and mode B, basically A_1 and B_1 in the fitting function. The real and imaginary parts of the complex poles indicate the resonance frequencies and loss rates, respectively. The number of fitting parameters is $2N + 1$. N should be at least four times larger than the number of expected poles, i.e., the sum of expected poles, corresponding background poles, and their complex conjugates [100]. In our system, in the frequency range of interest, we have two modes (mode A and mode B), and N should thus be at least 8. Resonance frequency (ω) and loss rates (γ) information are thus extracted from A_k

$$\omega_R = \frac{Im(A_k)}{2\pi} \tag{9}$$

$$\gamma = \frac{-Re(A_k)}{\pi} \tag{10}$$

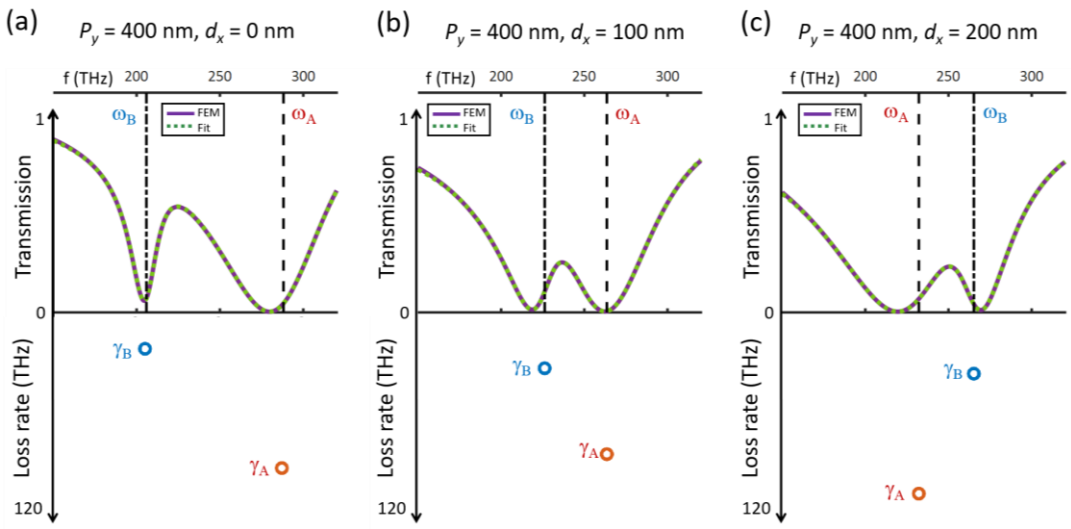

Figure 5.3 Transmission, $|S_{21}|^2$ are plotted for P_y = 400 nm as a function of the shift, dx. (a) d_x = 0 nm, (b) d_x = 100 nm, (c) d_x = 200 nm for the case: P_x = 400 nm, h_s = 100 nm, and L = 250 nm, respectively. The simulation data and fitting results show excellent agreement. Resonance frequencies crossed whereas loss rates avoided.

To validate the fitting method, we compare the fitting results (green dashed line) to the numerical simulations (purple line) in Figure 5.3. The numerical results of the scattering parameter $|S_{21}|^2$, (transmission) are perfectly fitted by the rational function that thus yields the correct poles. Other scattering parameters are similarly fitted and generate the same poles. Complex eigenvalues are successfully extracted using a rational fitting method in a coupled resonance system. We clearly see the complex eigenvalues vary as lateral displacement and level cross occurs after d_x of 100 nm. Tracking resonance behavior makes it possible to pinpoint a resonance frequency and loss rate from scattering parameters.

5.4 Tuning Loss

Plasmon hybridization scheme can be inverted by lateral displacement (d_x), which gives rise to resonance frequency crossing in a hybridized system. However, non-Hermitian degeneracy,

EP needs simultaneous coincidence of complex eigenvalues, i.e., resonance frequency and loss rate. Control of dissipation is a key factor in reaching an exceptional point in the non-Hermitian open system. For an EP of order 2, the coalescence of two levels requires two physical parameters. There are many controllable physical parameters in the unit-cell structure, namely, P_x, P_y, d_x, and h_s. Here, we investigate two different positions of a nanorod in a multilayered structure to observe the behavior of dissipation by changing the distance between the nanorods in Y-direction (P_y).

Figure 5.4 (a, b) shows resonance frequency and its loss rate of single nanorod in different layers, air, and spacer with sweeping size of unit-cell in Y-direction. The nanorod dimensions are identical for both physical setups. The calculated resonance frequencies are quite different due to the surrounding environment. The resonance frequencies are dependent on the period in Y-direction. Most radiation emitted perpendicular to nanorods in Y-direction, which leads to strong near-field interaction. By enhancing P_y from 350 to 500 nm, the loss rate of the resonance system is remarkably reduced. The loss rate of two physical setup exhibits almost the same magnitude with P_y variation, meaning that dissipation is merely dependent on the surrounding environment. It is worth note that the loss rate of the resonance system is very dependent on the size of unit-cell in Y-direction due to the area ratio (unit-cell size divided by nanorod size).

In Figure 5.4 (c, d), the transmission spectra are plotted with two different physical setups. Insets show the different positions of a nanorod in a multilayered structure. For both cases, the linewidths of transmission are gradually broadened with a decrease in P_y. In Figure 5.4 (e, f), the total loss (γ) is separated into absorption (α) and scattering (σ) loss for two physical setups, respectively. The most optical loss is dominated by scattering, indicating the radiative properties of dipole nanoantenna. The dependence of scattering loss on P_y variation is very significant, whereas absorption loss remains constant. The change of unit-cell size in Y-direction can tune not

only the loss rate but also resonance frequency in the plasmonic array. This method can be readily applied to the plasmon hybridized system for level repulsion and vice versa.

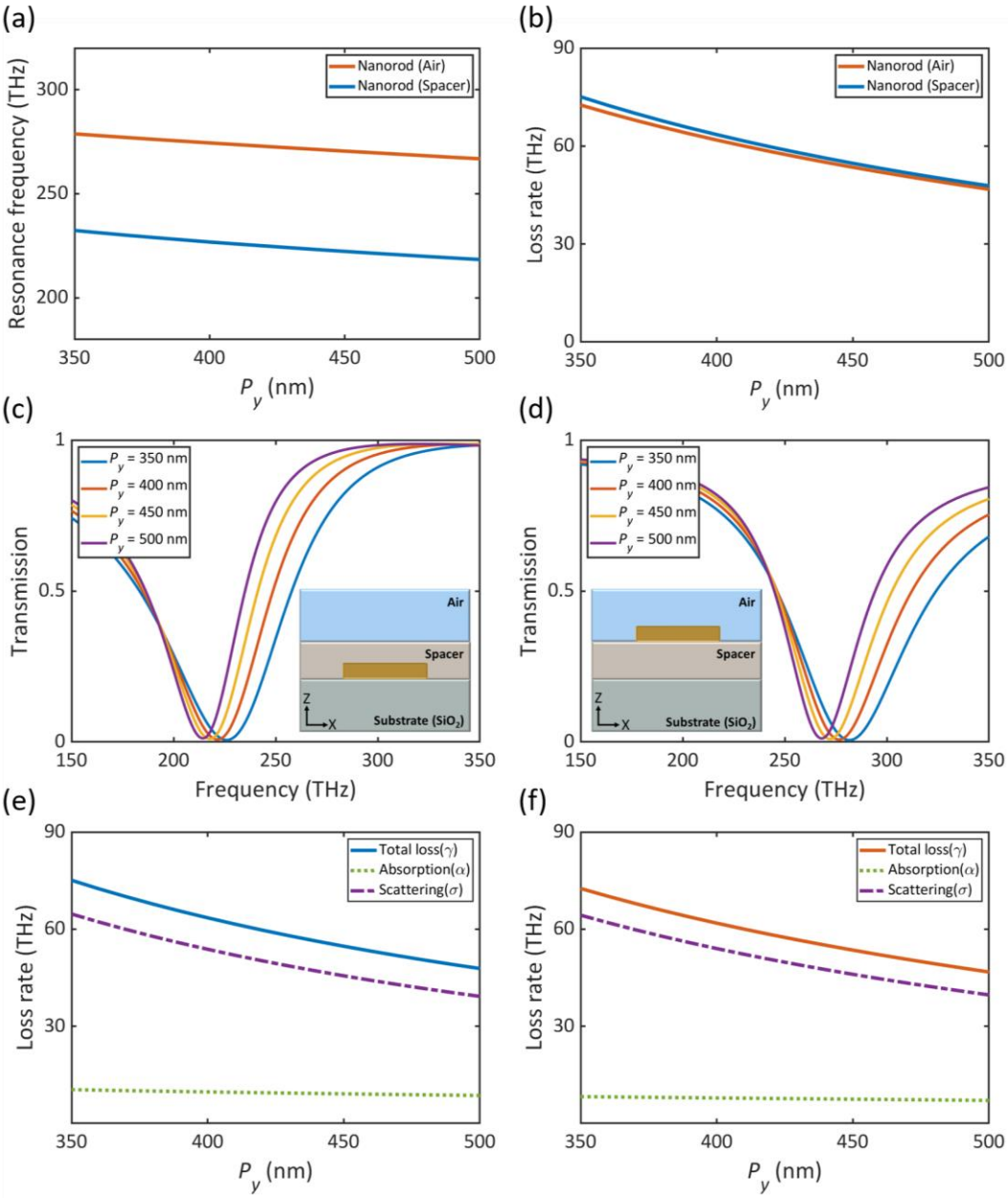

Figure 5.4 Calculated complex eigenvalues and loss rate contribution for two different nanorod position in the multilayered structure. (a, b) The resonance frequency and loss rate. (c, d) Transmission spectra with P_y variation. Inset indicates two different physical setups. (e, f) The calculated optical loss in the system: absorption and scattering loss.

5.5 Symmetry-dependent Hybridization Scheme

Plasmon exceptional points exist in open multimode systems, and the challenge of their observation resides in the identification of real physical parameters, i.e., simple geometrical parameters, enabling their implementation. To implement EP in plasmonic system, three different configurations were considered (see Figure 5.5). The first one consists of an array of paired metallic bars of the same dimensions embedded in a dielectric slab with refractive index n_{slab} = 1.5. The second configuration consists of an array of paired metallic bars with detuned resonances embedded in the same dielectric slab. The control of two physical parameters represented by the shift between the center of the two metallic bars in the direction of their electric dipolar mode (d_x) and the periodicity in Y-direction (P_y) lead to the emergence of an exceptional point (EP). The third configuration enables exceptional points and can be used for sensing applications as the top metal layer is exposed to air for functionalization and analytes binding.

Our system consists of a bilayer plasmonic structure made of two optically dissimilar plasmonic resonators array with detuned resonances. The periodic system is infinite in the XY plane and of finite size out-of-plane and is thus a metallo-dielectric photonic crystal. The detuning is implemented by symmetry breaking either using identical resonators in distinct optical environments or using structures of distinct size in a uniform optical environment (Figure 5.5).
Figure 5.5 presents the real and imaginary parts of the eigenmodes of hybridized plasmonic arrays of optically identical resonators, configuration 1 (Figure 5.5 a-b) and optically dissimilar resonators as a function of the lateral shift between the center of the dipoles (d_x) and the periodicity perpendicular to the electric dipole moment (P_y). The optically dissimilar structures are implemented using either resonators of dissimilar size, configuration 2 (Figure 5.5 c-d) embedded in a dielectric slab (n_{slab} = 1.5 and $h_{z,slab}$ = 240 nm) or using resonators of identical size in distinct

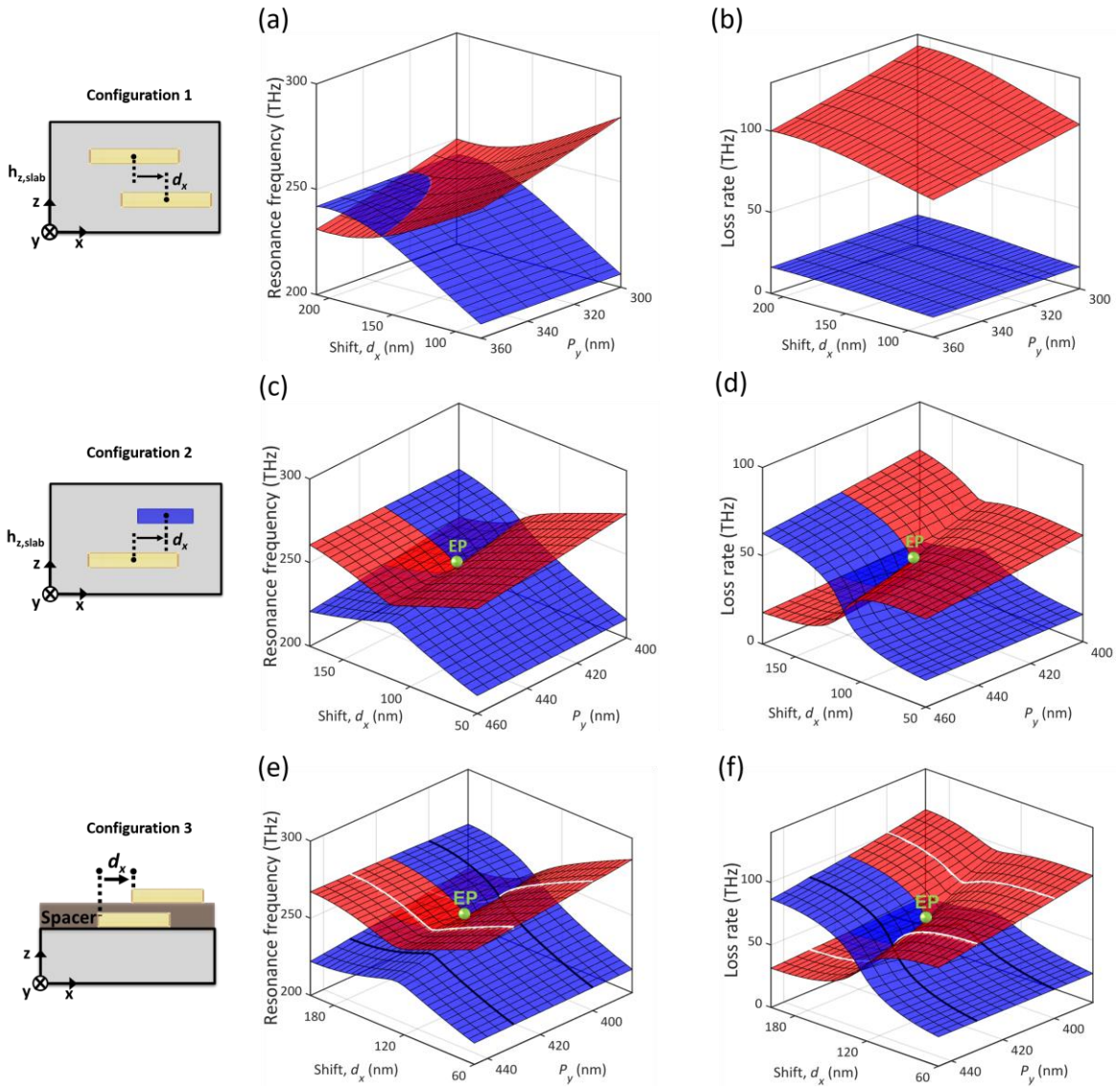

Figure 5.5 Plasmonic exceptional point and symmetry-dependent hybridization scheme of resonances and loss rates. Plasmonic resonators arrays of identical size, configuration 1 (a, b), dissimilar size embedded in a dielectric slab, configuration 2 (c, d), identical size, configuration 3 (e, f) as a function of the lateral shift.

optical environments, configuration 3 (Figure 5.5, e-f). The hybridization of optically identical resonators leads to symmetric and antisymmetric modes, and resonances cross along a diabolic line as a function of d_x and P_y (Figure 5.5 a). Because of the opposite symmetry of the hybridized modes, their loss rates (Figure 5.5 b) are very different and are always avoided [103]. The

symmetric configuration can thus not lead to exceptional points (EPs) and leads to usual Fano resonances where two modes of distinct loss rates overlap.

The hybridization of optically dissimilar resonators, however, led to two-hybrid modes with crossing and avoided crossing of both the resonances and loss rates (Figure 5.5 c-d, e-f) unambiguously demonstrating the existence of a plasmonic exceptional point where resonances and loss rates become simultaneously degenerate. By breaking the symmetry, i.e., making the bars optically different, the hybridized modes are no longer purely symmetric or anti-symmetric, making interference via radiation possible. It is worth noting that the loss rate for plasmonic EPs includes losses by radiation and absorption. The EP singularity (black dot) occurs at ~ 241 THz in configuration 2, and, at ~ 246 THz in configuration 3. The interplay between near-field Coulomb interactions (mostly controlled by d_x) and radiative coupling via interferences (enabled by symmetry breaking and mostly controlled by P_y) allows the coalescence of the hybrid modes.

5.6 Coupled mode model

To validate numerical simulation results of the existence of plasmonic EP, we first model the identical resonator system using the Lagrangian formalism for coupled resonators [96]. The coupled resonator system can be modeled as:

$$\frac{d^2a_1}{dt^2} + {w_0}^2 a_1 + 2\Gamma\frac{da_1}{dt} = -k_m\frac{d^2a_2}{dt^2} - k_e{w_0}^2 a_2 \tag{11}$$

$$\frac{d^2a_2}{dt^2} + {w_0}^2 a_2 + 2\Gamma\frac{da_2}{dt} = -k_m\frac{d^2a_2}{dt^2} - k_e{w_0}^2 a_2 \tag{12}$$

where $a_{1,2}$ are the field amplitude of modes 1 and 2 in the resonators, $k_{e,}$ and k_m the electric and magnetic coupling coefficients between the two resonators, Γ is dissipation coefficients, and w_0 is the uncoupled resonance frequency. We assume harmonic time dependence for $a_{1,2}$ as exp(jwt). Moreover, we use $k_m - k_e = k$, the coupling coefficient between two resonators which is the overlap integrals of each resonators' electric and magnetic fields [97], [98],

$$k = \frac{\int \mu H_1 \cdot {H^*}_2 dv - \int \varepsilon E_1 \cdot {E^*}_2 dv}{\int \varepsilon |E|^2 dv} = k_m - k_e \tag{13}$$

The modified dynamics equations are approximate:

$$\frac{d^2a_1}{dt^2} + \widetilde{w_0}^2 a_1 + \widetilde{w_0}^2 k a_2 = 0 \tag{14}$$

$$\frac{d^2a_2}{dt^2} + \widetilde{w_0}^2 a_2 + \widetilde{w_0}^2 k a_1 = 0 \tag{15}$$

where $\widetilde{w_0}$ is the uncoupled resonance complex frequencies $(\omega + \mathrm{j}\gamma)$ of resonators. ω is the resonance frequency, and γ represents the loss rate. It is also equivalent to substitute the coupled field equation into Maxwell's equations and obtain the differential equations for the field of each resonator.

Solving the characteristic equation for the differential equations above gives two resonances $\widetilde{w_1}'$ and $\widetilde{w_2}'$

$$\widetilde{w_{1,2}}' = \widetilde{w_0}\sqrt{1 \pm jk} \tag{16}$$

Figure 5.6 shows the simulation and fitting results based on the model explained above for P_y = 350 nm and d_x from 0 nm to 250 nm. Figure 5.6 (a) is the resonance frequency and Figure 5.6

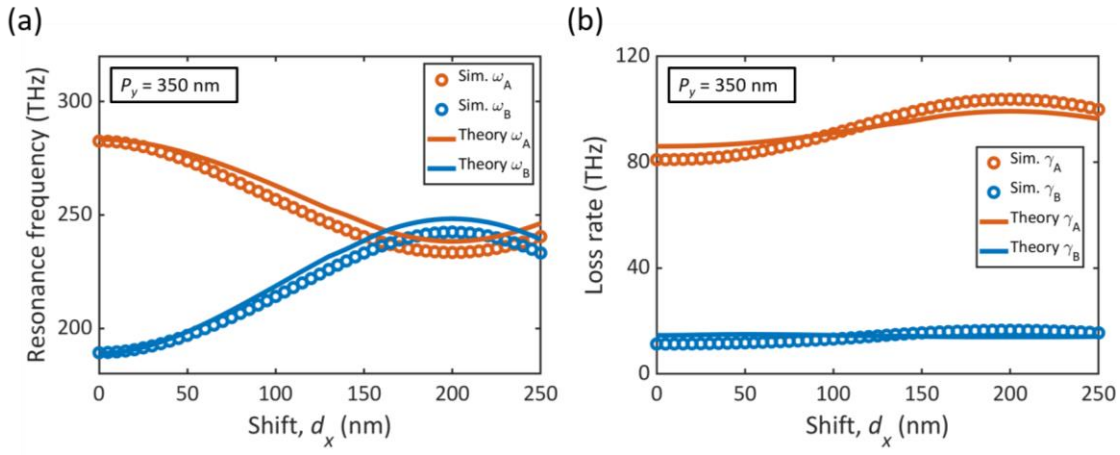

Figure 5.6 Resonance frequency and loss rates with different dx. (a) Resonance frequency (b) Loss rates for P_y = 350 nm and d_x = 0 to 250 nm.

(b) is the loss rate. One can observe a good agreement between numerical simulations and the model in both cases of crossing for resonance frequencies (Figure 5.6 (a)) and avoided crossing for loss rates (Figure 5.6 (b)) in the case of the diabolic point (DP) system (identical coupled resonators).

To reach an exceptional point (EP), the two resonators can be implemented either using identical resonators in distinct optical environments or using structures with resonators of distinct size in a uniform optical environment (Figure 5.5). For the EP case, we need two distinct resonators. Using the same approach as in the previous example, the modified dynamic equations for distinct and lossy resonators can be approximated as:

$$\frac{d^2a_1}{dt^2} + \widetilde{w_1}^2 a_1 + \widetilde{w_2}^2 k a_2 = 0 \tag{17}$$

$$\frac{d^2a_2}{dt^2} + \widetilde{w_2}^2 a_2 + \widetilde{w_1}^2 k a_1 = 0 \tag{18}$$

where $\widetilde{w_1}$, $\widetilde{w_2}$ are the uncoupled and distinct resonance complex frequencies of resonators 1 and 2, and k is the coupling coefficient between the two resonators again.

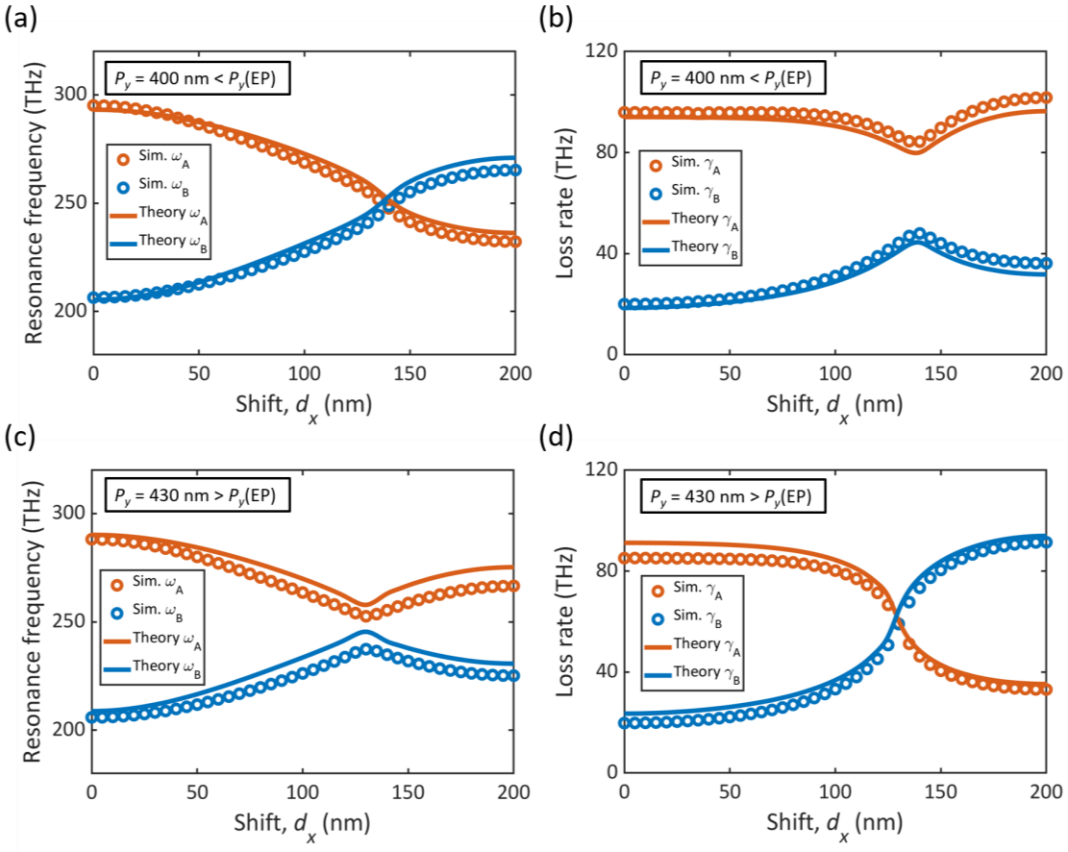

Figure 5.7 Resonance frequency and loss rates with different P_y and different d_x. (a) Resonance frequency for P_y = 400 nm (b) Loss rates for P_y = 400 nm (c) Resonance frequency for P_y = 430 nm (d) Loss rates for P_y = 430 nm.

Solving the characteristic equation for the differential equations above gives two resonances $\widetilde{w_1}'$ and $\widetilde{w_2}'$

$$\widetilde{w'}_{1,2}{}^2 = \frac{1}{2}\left[\widetilde{w_1}^2 + \widetilde{w_2}^2\right] \pm \sqrt{\left(\frac{\widetilde{w_1}^2 - \widetilde{w_2}^2}{2}\right)^2 + \widetilde{w_1}^2\widetilde{w_2}^2 k^2} \quad (19)$$

Figure 5.7 shows the simulated frequency, and fitting results by the theory explained above. Figure 5.7 (a, b) presents the resonant frequency and loss rate for P_y = 400 nm, and Figure 5.7 (c, d) presents the same for P_y = 430 nm. We vary the d_x from 0 nm to 200 nm for both cases. One can observe that the resonance frequency is crossing, but the loss rate is avoided crossing for P_y = 400 nm while the resonance frequency is avoided crossing, and the loss rate is crossing for P_y = 430 nm. Hence, an EP unambiguously exists in this parameter range.

5.7 Residue Calculation

In order to identify the modes at the crossing or avoided crossing, we used an approach consisting of calculating the residues of the modes as it was demonstrated that the residues of the modes diverge at EP [99]. We calculated the residues of our system at the EP singularity, and it does diverge as expected and seen in Figure. 5.8 (a, b). The figure also shows that the real and imaginary parts of the residues diverge as the singularity is approached. At an EP singularity, both real and imaginary parts of the modes are the same, and the residues are very large. Please note that at this point, we did not label modes yet as crossing or avoiding each other (point of the same color).

As one approaches an EP, as discussed by varying one parameter (d_x) while the second parameter is kept constant (P_y), either the frequencies or loss rates should cross while the other parameter avoided cross. The attribute (frequency or loss rate) of the modes that cross can be arbitrarily close (they become degenerate), and thus have larger residues compared to the modes

that do not cross around an EP. Interestingly, the residues magnitude becomes even larger when one is closer to the singularity.

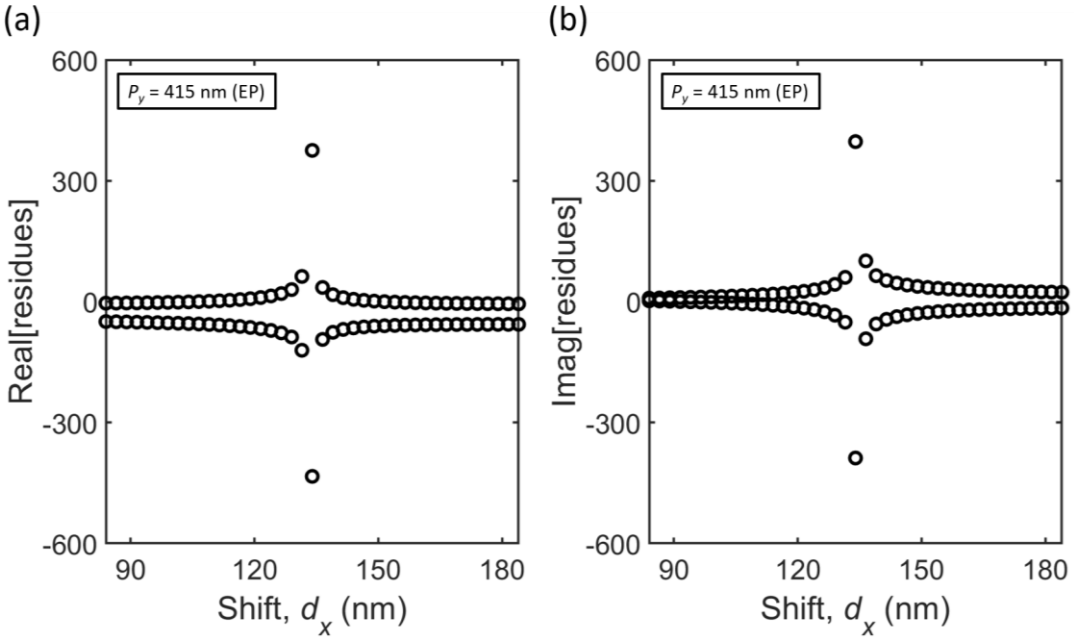

Figure 5.8 Residues are calculated for P_y = 415 nm as a function of the shift (d_x). (a) Real (b) Imaginary part of residues for the system at the EP singularity diverge as the singularity is approached.

For example, when the frequency of modes crosses, a larger separation should be observed on the real part of the residues around the EP. We plotted in Figure 5.8 (a-d) for P_y = 400 nm and P_y = 430 nm, the real and imaginary parts of the residues. We clearly observe that the separation of residues reaches a maximum on the real part for P_y = 400 nm as dx varies and reaches a maximum on the imaginary part for P_y = 430 nm. This does not occur for the mode undergoing avoided crossing. This is the rationale that we used to discriminate between crossing and avoided crossing in our experiments. Together with the branch cut singularity observed in Figure 5.8, we claim that an EP is unambiguously observed. It is worth noting that the ambiguity on whether

modes are crossing or avoiding each other as one approaches the singularity can be lifted using the numerical and experimental residues around the EP.

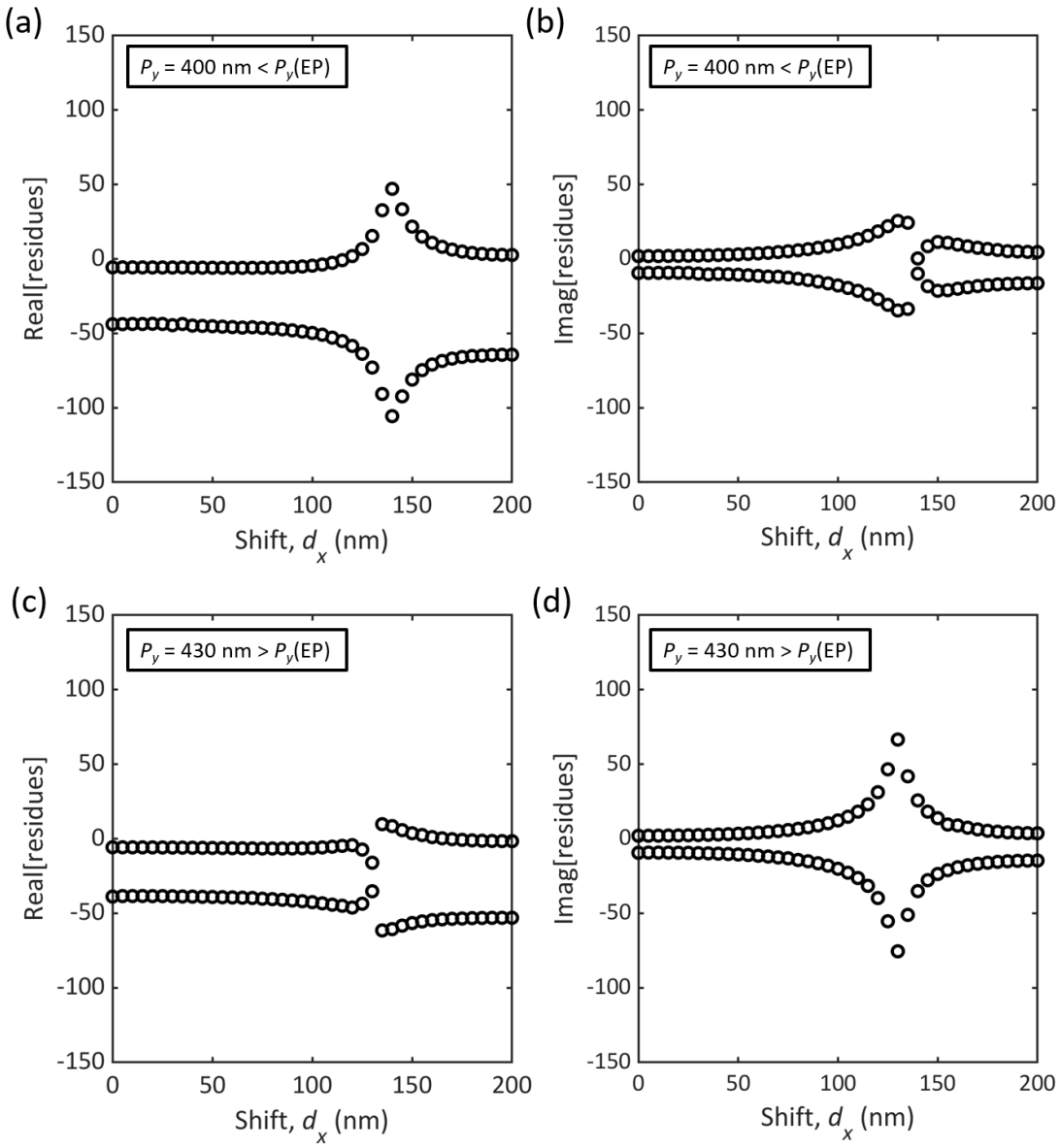

Figure 5.9 Residues are calculated for different P_y (400, 430 nm) as a function of d_x. (a) For P_y = 400 nm and d_x = 140 nm where resonance frequencies cross, the maximum separation is observed (b). (c) For P_y = 430 nm and d_x = 130 nm where resonance frequencies avoided while (d) Loss rate crossed, the maximum separation is observed in the imaginary part.

Furthermore, we calculate the spatial structure of modes around the EP, and it clearly shows that modes are distributed on both layers, making their mapping challenging. Figure 5.10 (a, b) shows the dispersion of resonance frequency as a function of lateral shift (d_x) for different

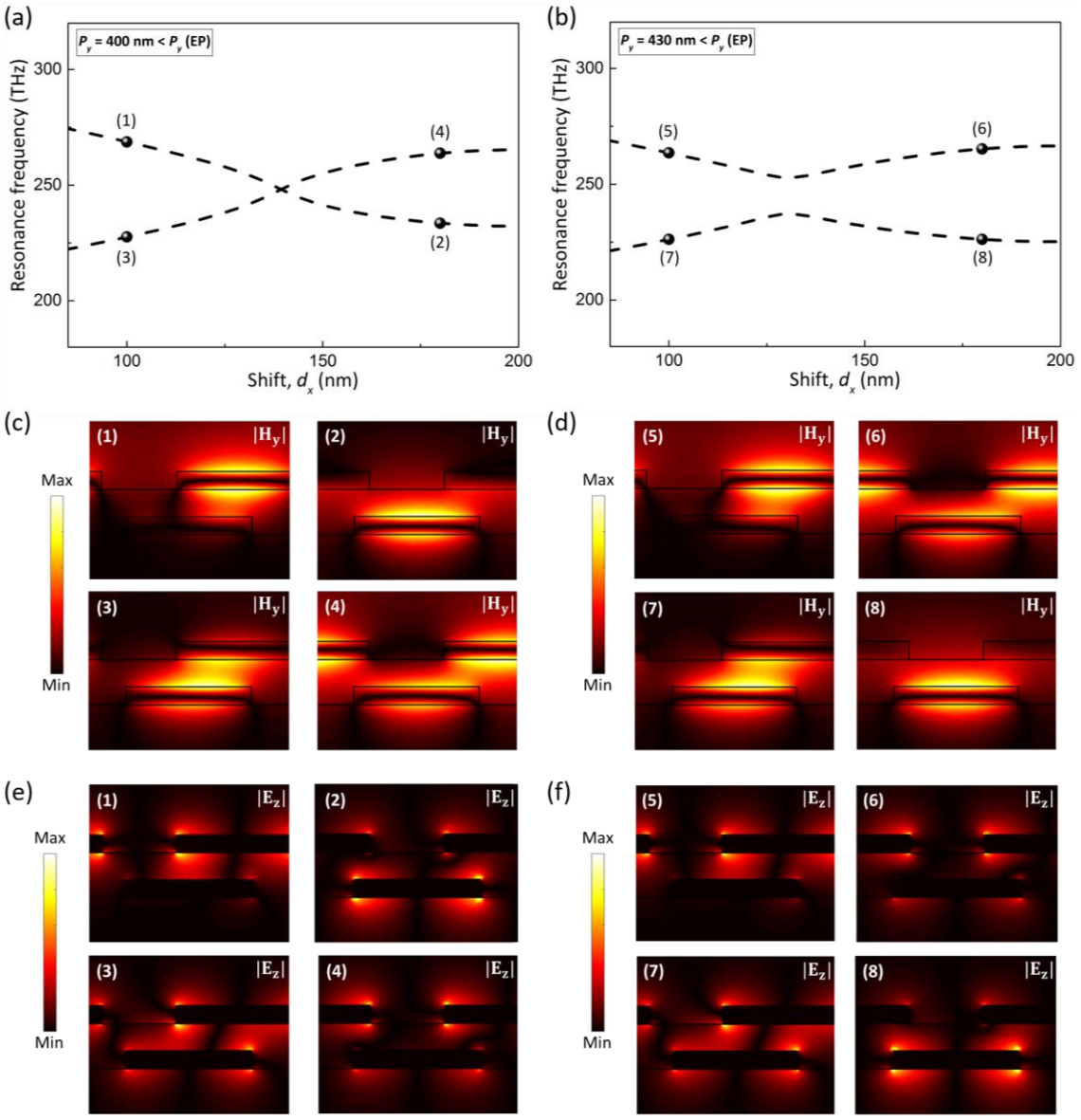

Figure 5.10 Dispersion of resonance frequency and the absolute value of magnetic and electric field distribution. (a, b) Resonance frequency as a function of lateral shift (d_x) for different P_y (400 and 430 nm, respectively). (c, d) The absolute value of the out-of-plane component of the magnetic field distribution ($|H_y|$). (e, f) The normal component of the electric field ($|E_z|$).

P_y (400 and 430 nm, respectively). The absolute value of the out-of-plane component of the magnetic field of the modes ($|H_y|$) is presented in Figure 5.10 (c, e) at indicated points on the resonance frequency dispersion plots. The out-of-plane magnetic field at points (1), (2) in Figure 5.10, and points (5), (8) in Figure 5.10 is mostly localized in one bar, corresponding to a dominating current flowing in that bar, and thus corresponding to an electric dipolar mode. Points (3), (4) in Figure 5.10 (c) and (6), (7) in Figure 5.10 (d) are dominated by a magnetic field in the spacer, i.e., an antisymmetric current flow in the bars, and thus corresponding to a magnetic dipole/ electric quadrupole moment. The multipolar identification of modes clearly shows that, as expected around an EP, modes are maintained as they resonances cross in Figure 5.10 (a) and switch as resonances avoid cross in Figure 5.10 (b). The localized nature of the plasmonic resonances is better seen from the normal component of the electric field ($|E_z|$) of the modes at the same points, as shown in Figure 5.10 (e, f).

5.8 Optical Loss of Hybridized System

EP singularities can be reached by sweeping two physical parameters (P_y, d_x) in a plasmonic hybridized system. As we discussed in Chapter 5, loss tuning is achieved by controlling the size of a unit-cell in Y-direction. The behavior of optical loss in the plasmonic hybridized system is investigated to understand EP in the non-Hermitian system. We calculated the optical loss behavior in the plasmonic hybridized system around EP. In Figure 5.11, the evolution of resonance frequency is plotted as a function of d_x for different P_y (400 and 430 nm). Figure 5.11 (c - f) shows the calculated optical loss for two different modes γ_A and γ_B respectively.

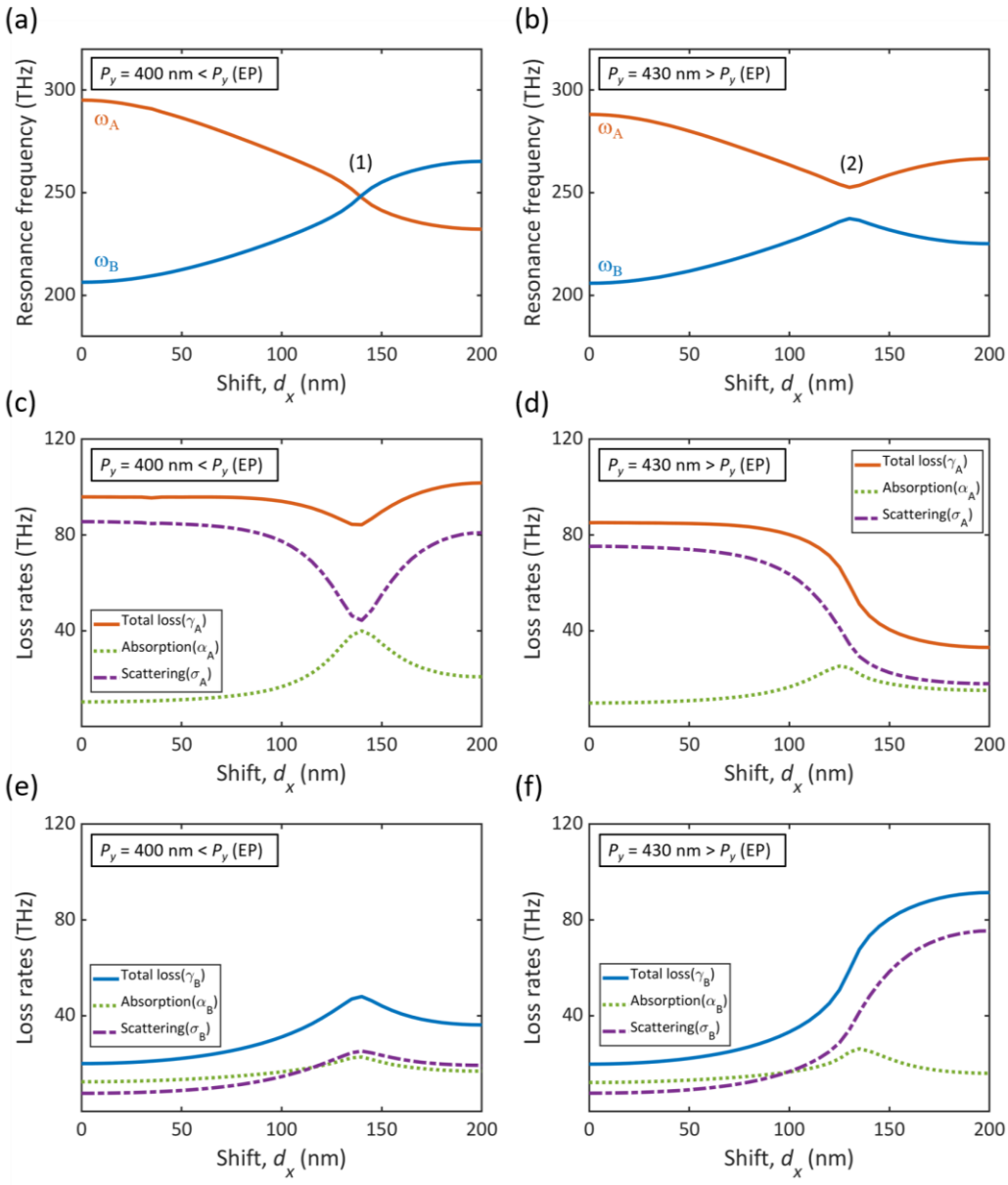

Figure 5.11 Complex eigenvalues for different P_y as a function of d_x and behavior of optical loss. (a, b) Resonance frequency for P_y (400, 430 nm). (c, e) Optical loss for P_y = 400 nm (d, f) Optical loss for P_y = 430 nm.

For P_y = 400 nm, resonance frequencies are crossed, whereas loss rates are avoided. The most optical loss is dominated by scattering γ_A due to the presence of electric dipolar mode, as seen in Figure 5.11 (c). Interestingly, scattering and absorption loss exhibit similar magnitude at d_x of 140 nm where resonance frequencies are crossing. This is because two resonances reside in

close in spectra, which results in strong absorption, as seen in Figure 5.12 (a). In contrast, scattering and absorption loss of γ_B equally contribute to optical loss in Figure 5.11 (c). Due to the maintaining of modes while resonance crossing, the loss rate of γ_A is always higher than γ_B for d_x from 0 to 200 nm.

Avoided cross of resonance frequencies are observed for P_y = 430 nm, as shown in Figure 5.12 (b). Two hybridized modes are switched at d_x of 130 nm, resulting in the cross of loss rates in Figure 5.11 (d, f). Unlike the crossing of the resonance case, absorption loss does not significantly contribute to total loss because resonances reside away from each other. The absorption peak is obtained, but it is broad compared with the resonance cross case in Figure 5.11 (b). Mostly scattering loss (σ) dominates than absorption loss (α) for d_x variation. The behavior of scattering loss follows the behavior of total loss closely.

Loss engineering in the plasmonic system plays an essential role in many applications such as sensors, spectroscopy, and imaging. These results will provide crucial insight to investigate optical loss behavior in a more complex structure to improve their performance.

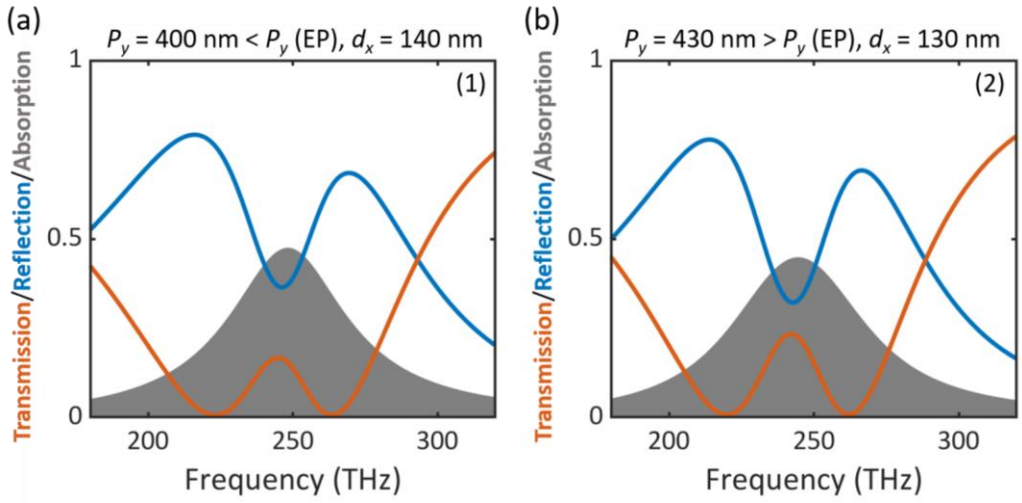

Figure 5.12 Transmission, reflection, and absorption for different P_y parameters. (a) P_y = 400 nm, d_x = 140 nm, point (1) in Figure 5.11 (a). (b) P_y = 430 nm, d_x = 130 nm, point (2) in Figure 5.11 (b).

5.9 Experimental Observation of Plasmonic EPs

For observation of the existence of a plasmonic EP in the experiment, the real and imaginary parts of eigenvalues should be extracted in experimental measurement. To implement this, we measure the amplitude and phase of transmitted light. The transmission light is measured using Fourier-transform infrared spectroscopy, while the phase is measured by using custom spatially and spectrally resolved broadband interferometer. These characterizations require optically the same area of the plasmonic array to obtain the correct amplitude and phase associated with the resonance system.

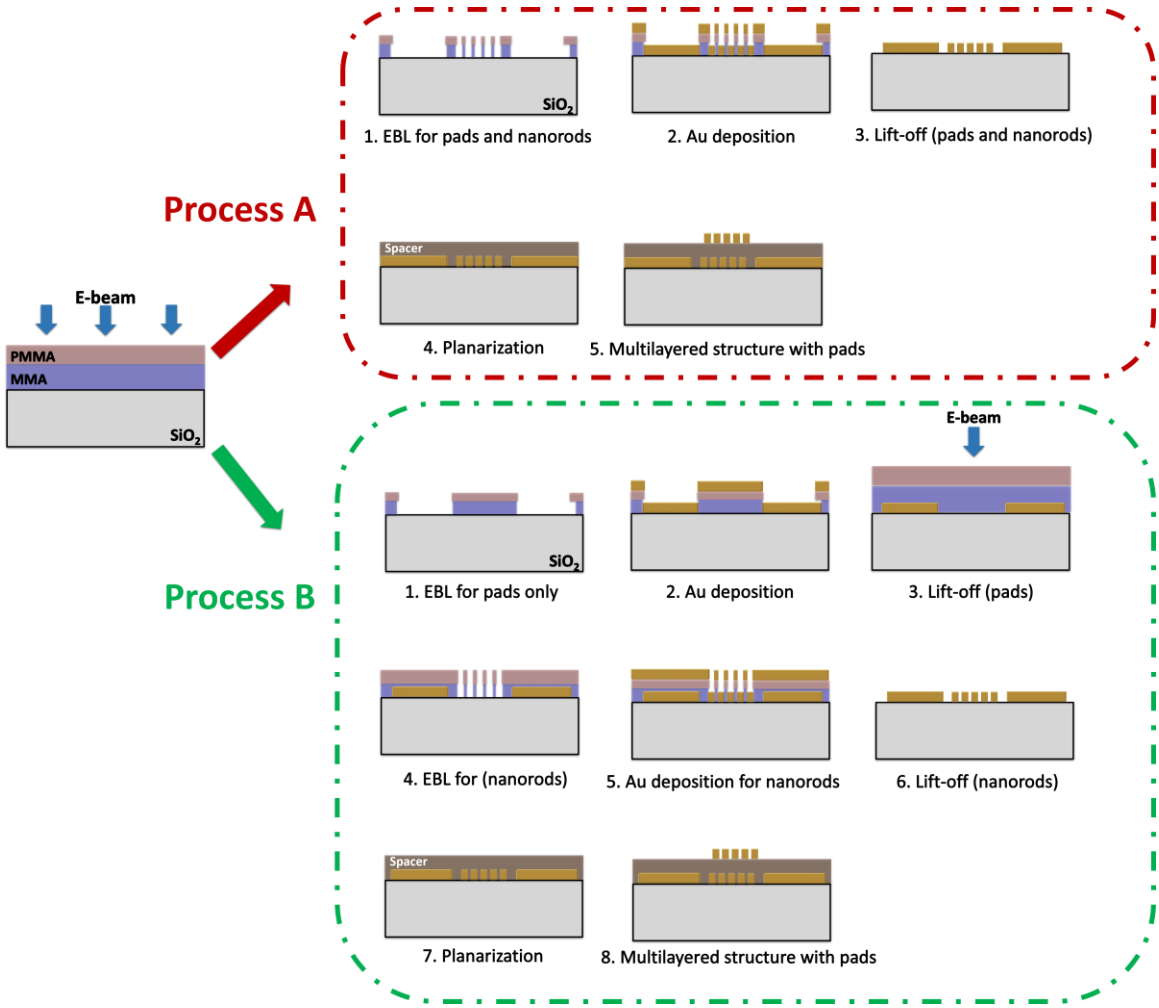

Figure 5.13 Fabrication process for plasmonic arrays with pads.

For the EBL fabrication, the metal pads are added to an additional step. Here, we suggest and test two different processes to make metal pads for optical characterization. Fabrication flow charts for two different processes are described in Figure 5.13. One proposed method (Process A) is to use the EBL step for plasmonic array and pad at the same time. Another suggested method (Process B) separates the pad and plasmonic array EBL step. Process A will reduce the time and cost of fabrication, while process B is an inefficient fabrication process due to the complexity.

However, the fabrication results are quite impressive. The EBL process for plasmonic array and pads at the same process fails to transfer patterns to substate. This is because the electron beam exposure to pads generates numerous scattered charges, which results in a surge in the dose of electron beam lithography.

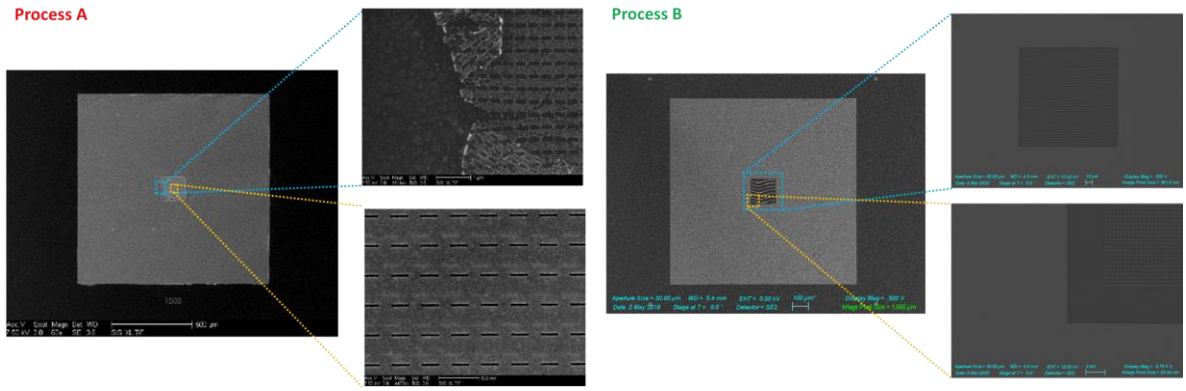

Figure 5.14 SEM images of the process A and B for plasmonic array and pads.

Consequently, positive-tone PMMA is converted to a negative-tone one. Figure 5.14 shows the results of the SEM image of Process A. The center of the plasmonic array (yellow area) become plasmonic nano slits, not nanorods. Due to the extensive area of pad compared to the plasmonic array, process A fails to transfer patterns on the substrate. Although process B increases the complexity of total steps, the fabricated structures prove the high quality of plasmonic array and pads, as shown in Figure 5.14. The fabrication test of the plasmonic array and pad test implies that

the achievement of high reliability and reproducibility of fabrication work induces cost, time, and complexity.

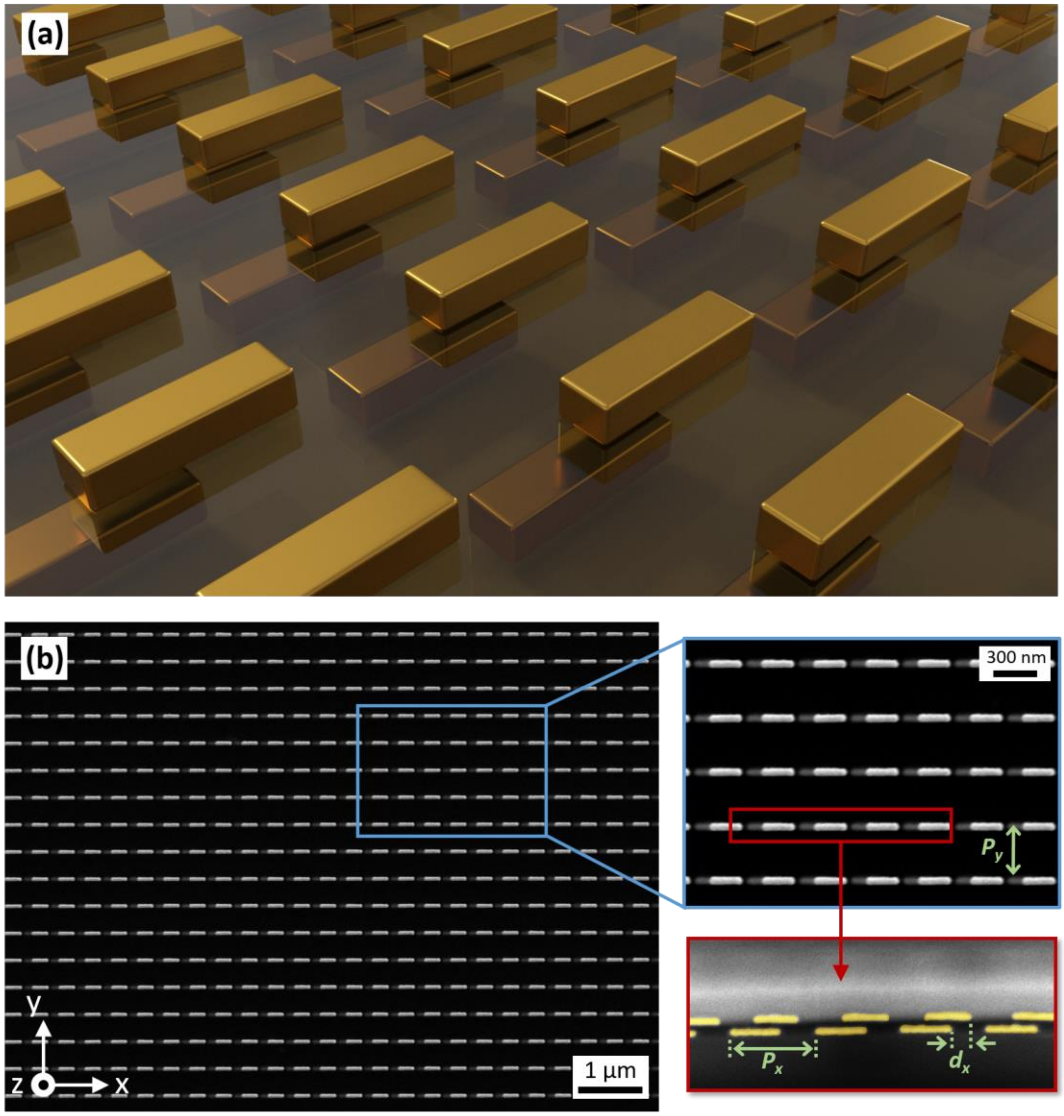

Figure 5.15 Multilayered periodic plasmonic structure supporting exceptional points. (a) Schematic of a multilayer periodic plasmonic structure. (b) Left: Top-view SEM of the fabricated multilayer structure. Right: Zoom-in top and side views. The side view image is obtained using a dual-beam focused ion beam (FIB)-SEM.

Figure 5.15 (a) shows the schematic of the multilayered plasmonic array. Figure 5.15 (b) (right) shows the zoom-in top (XY-plane) and side (XZ-plane) views of the plasmonic structure, clearly showing the top and bottom metallic bars and the quality of the fabrication and alignment

processes. The side view image is obtained using a dual-beam focused ion beam (FIB)-SEM that simultaneously enables the local sectioning (with the FIB) and imaging (with SEM) of the samples. P_x and P_y are in-plane periodicities, and d_x is the lateral shift between the center of the bars along the direction of their electric dipolar mode (X-direction). The period along the X-direction is fixed to P_x = 400 nm, while P_y and d_x are the two parameters used to tune the coupling between resonators array to reach an exceptional point. The proposed periodic platform makes for stronger output signals compared to single resonator approaches and is thus more suited for applications.

To experimentally demonstrate the existence of a plasmonic exceptional point, we characterize the fabricated samples as a function of the lateral shift d_x for two different values of the period in the Y-direction, P_y = 400 nm, and P_y = 430 nm. The experimental results are obtained by measuring both the amplitude and the phase of the transmitted light.

The transmission spectra were measured using a Fourier-transform infrared spectrometer with a tungsten halogen lamp as the light source (Bruker Vertex 70) combined with an infrared microscope (×15 Cassegrain objective, the numerical aperture NA = 0.4). The transmission spectra are measured at normal incidence and normalized by the transmission of an unpatterned SU-8 spacer layer on the glass substrate. All measurements are performed with light linearly polarized along the long axis of the metallic bars.

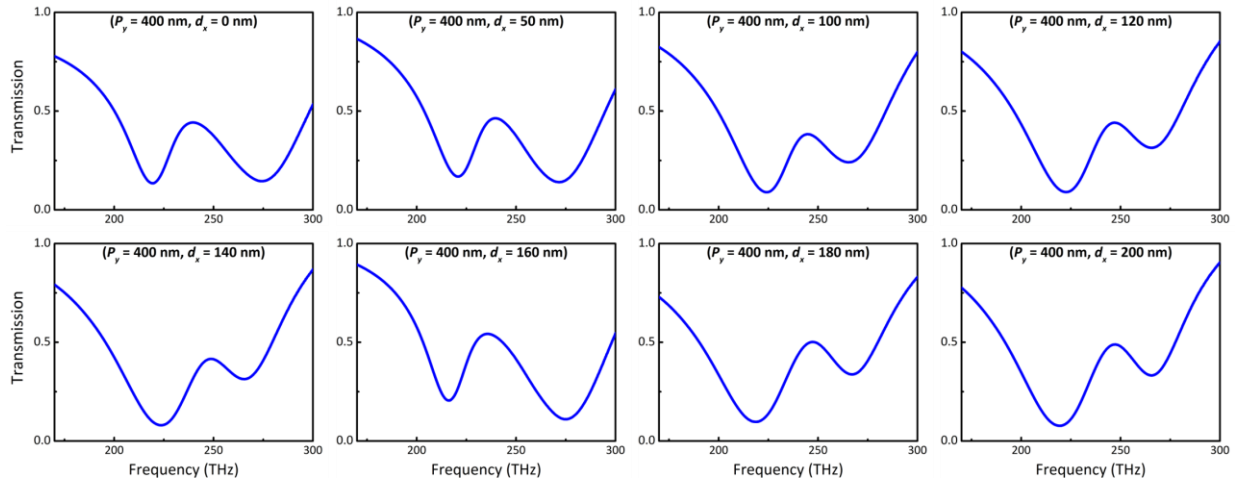

Figure 5.16 Transmission measurements of multilayered structures (P_x = 400 nm and P_y = 400 nm) with observable resonances (mode A and B) dispersing with the shift d_x varying from 0 nm to 200 nm.

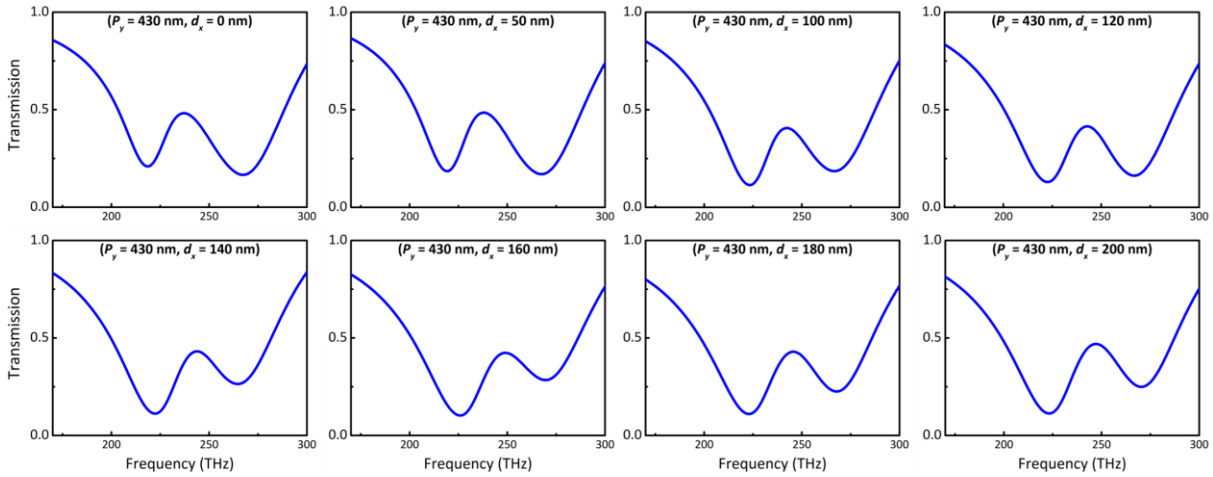

Figure 5.17 Transmission measurements of multilayered structures (P_x = 400 nm and P_y = 430 nm) with observable resonances (mode A and B) dispersing with the shift d_x varying from 0 nm to 200 nm.

To measure the phase of our structures, we constructed broadband spectrally and spatially resolved interferometer (SSRI). The SSRI technique allows a sensitive and precise real-time determination of the phase over a wide bandwidth. The experiment consists of a two-dimensional measurement of the spectral interference between a reference and a signal through the sample

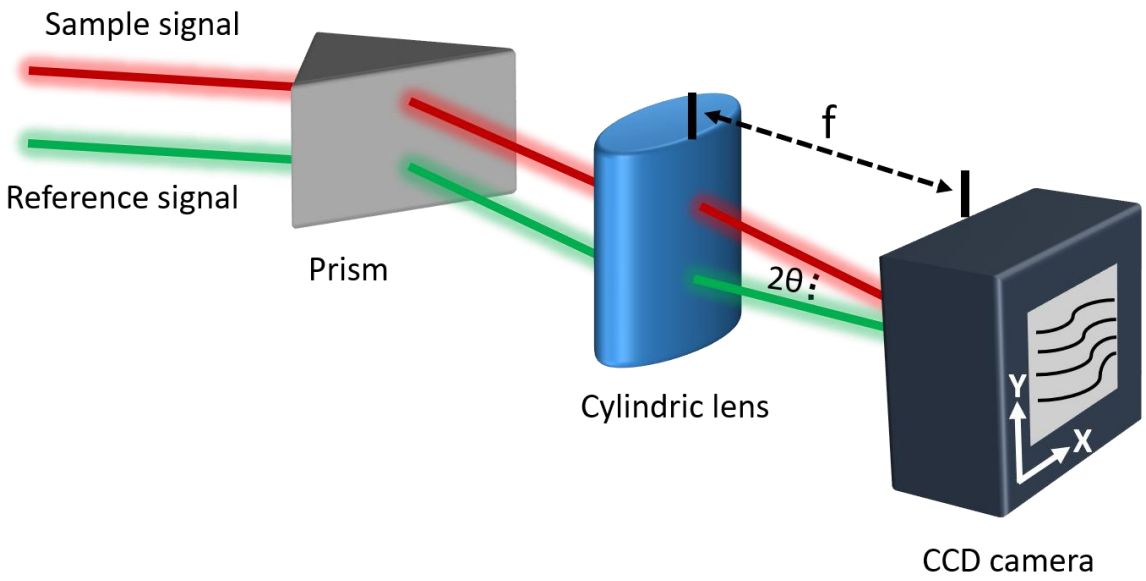

Figure 5.18 Experimental setup for broadband spatially and spectrally resolved phase measurement.

propagating at an angle [100]. As a light source, we use a supercontinuum laser (from NKT photonics) spanning the wavelength range of 400 to 2400 nm. The collimated white light beam was split into two by the un-polarized 50/50 wideband dielectric beam splitter for the reference and signal beams. The signal beam was reflected by a silver mirror, while the reference beam was reflected by a silver mirror angle reflector, so adjusted that the two beams, after passing through the separator again, propagate at an angle of $2\theta = 0.7°$ with respect to each other. The spectral intensities of the two beams are set to be approximately equal during the experiment in order to achieve a high fringe contrast of their interferogram and to reduce errors in the reconstruction process. The setup includes an integrated spatially resolved spectrometer consisting of a prism, a cylindrical lens (CL), and a camera (FLIR A6250sc). The spectral components of the two fields were spatially dispersed by an SF-18 prism, and the spectra of the two beams interfered with the focal plane of a 100 mm focal cylindrical lens, where the FLIR camera is located. The camera has

a resolution of 640 × 512 pixels with a detector pitch of 25 μm and a broadband detector from 400 to 1700 nm. The prism and the cylindrical lens were used to accommodate a bandwidth of the FLIR camera. To obtain the phase information from the interference pattern, we used the Fourier transform techniques [101].

To accurately measure the phase, many factors should be accounted for, such as beam uniformity, ambient air, mechanical vibration, spatial and spectral resolution, number of fringes, camera noise, smooth substrate, and large sample area for the beam waist [102]. Consider two plane waves, reference wave (U_{ref}) and signal wave (U_{sig}) with an angle 2θ, and the wave equations are given as

$$\begin{aligned} U_{ref} &= R_{(x_\lambda,y)} e^{i(\phi_R + k(f cos\theta + y sin\theta))}, U_{sig} \\ &= S_{(x_\lambda,y)} e^{i(\phi_s + k(f cos\theta - y sin\theta))} \end{aligned} \tag{20}$$

Hence, the two-dimensional interference intensity I is given by

$$\begin{aligned} I &= |U_{ref} + U_{sig}|^2 \\ &= {R_{(x_\lambda,y)}}^2 + {S_{(x_\lambda,y)}}^2 \\ &+ 2R_{(x_\lambda,y)} S_{(x_\lambda,y)} \cos\left[2ky sin\theta + (\phi_R - \phi_s)\right] \end{aligned} \tag{21}$$

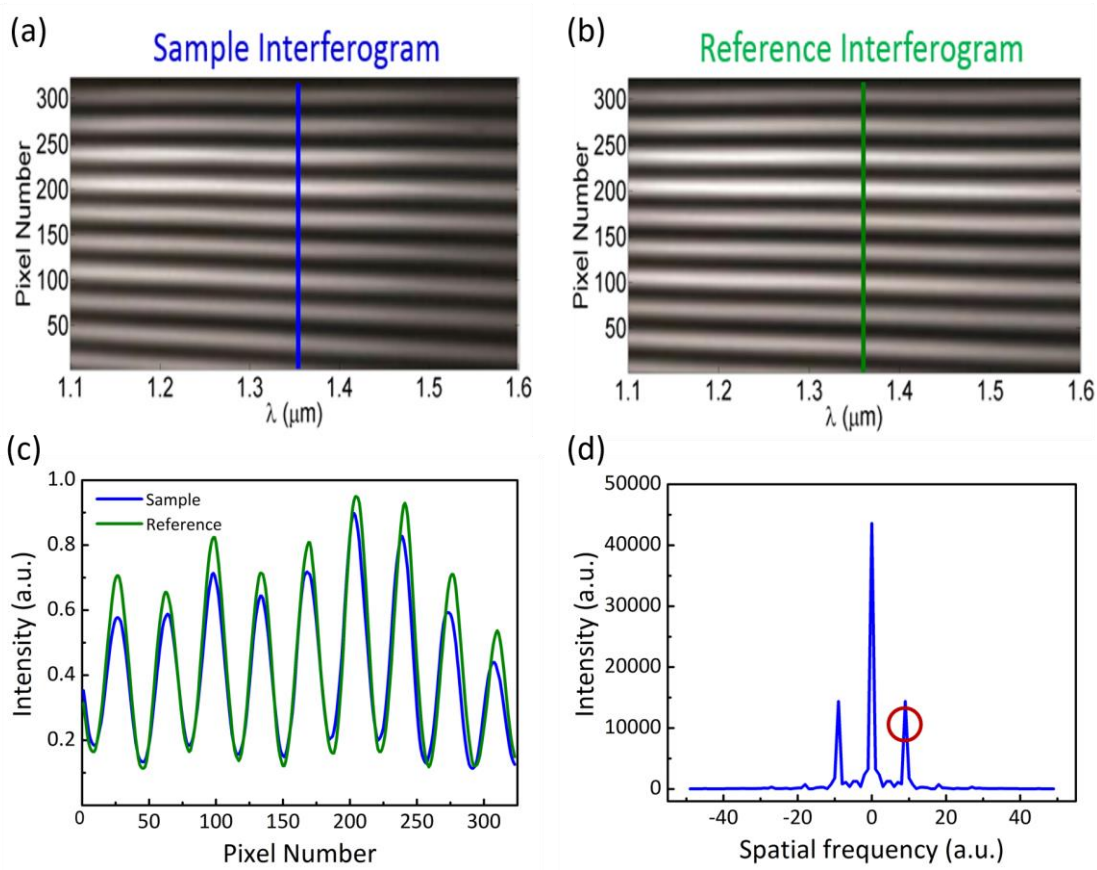

Figure 5.19 Example of interferograms obtained for the sample (a) and the reference (b). The cross-section (c) is shown for the same wavelength. (d) Fourier transform of a sample interferogram.

To extract the phase information, the Fourier transform at constant $\boldsymbol{\lambda}$ is calculated:

$$F(I) = {R_{(x_\lambda,y)}}^2\sqrt{2\pi}\delta(\omega) + {S_{(x_\lambda,y)}}^2\sqrt{2\pi}\delta(\omega) + R_{(x_\lambda,y)}S_{(x_\lambda,y)}e^{i\Delta\phi}\sqrt{2\pi} \times \delta\left(\left(ie^{-i\theta} - ie^{i\theta}\right)k + \omega\right) \quad (22)$$

$$\Delta\phi = \phi_R - \phi_s \quad (22)$$

The phase difference ($\Delta\phi$) information can be obtained by taking the phase of the complex value of the point circled in Figure 5. 19 (d).

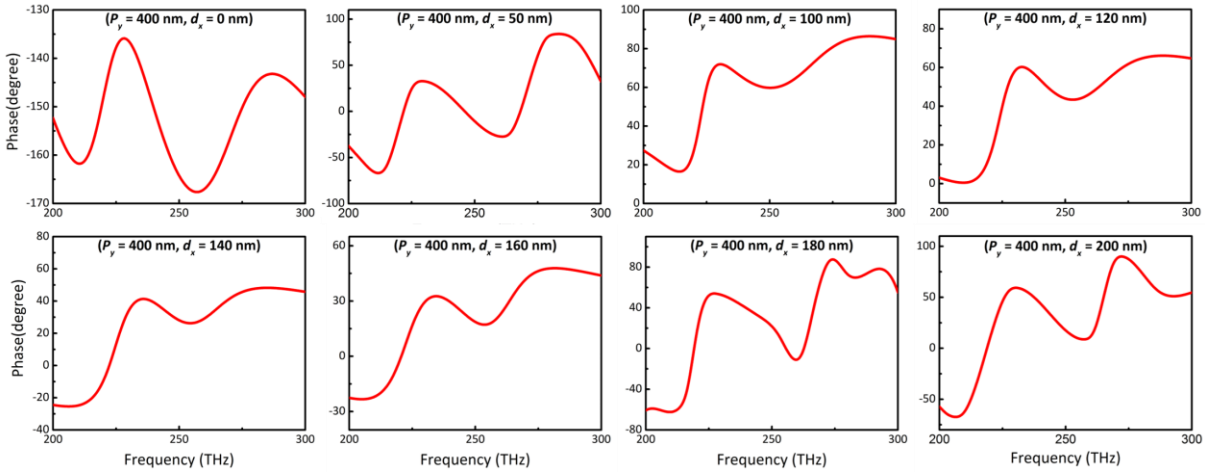

Figure 5.20 Measured phases for different shift d_x from 0 to 200 nm and for P_x = 400 nm and P_y = 400 nm.

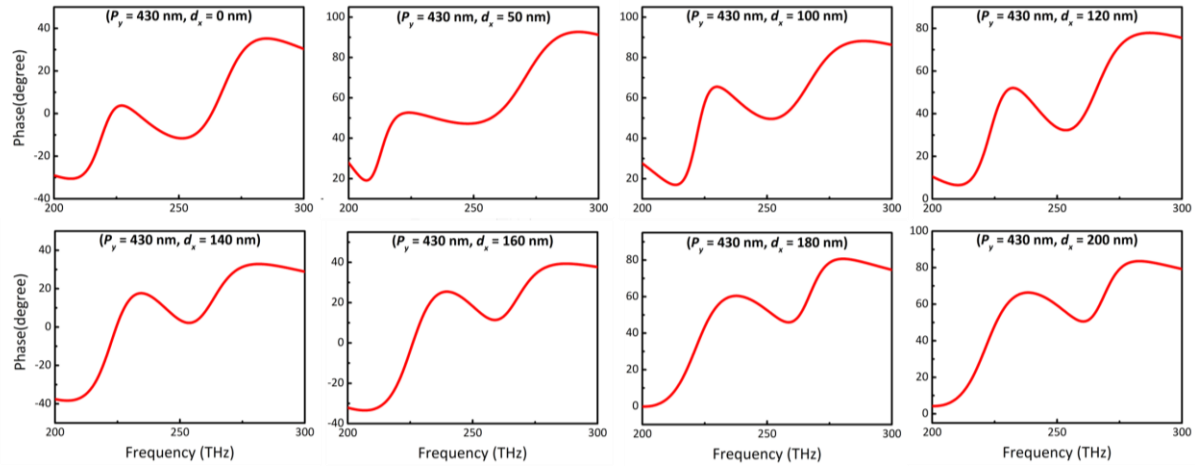

Figure 5.21 Measured phases for different shift d_x from 0 to 200 nm and for P_x = 400 nm and P_y = 430 nm.

To experimentally demonstrate the observation of a plasmonic exceptional point, we measure both the amplitude and the phase of the transmitted light. The transmission is measured using a Fourier-transform infrared spectrometer (Bruker Vertex 70) combined with an infrared microscope while the phase is measured using a custom spatially and spectrally resolved broadband interferometer as discussed. The amplitude and phase from optical characterization are

used for a rational fitting method to extract complex eigenvalues, real parts corresponding resonance frequency, and imaginary parts corresponding loss rate.

We characterize the fabricated structures as a function of the lateral shift d_x for two different values of the period in the Y-direction, P_y = 400 nm, and P_y = 430 nm. Figure 5.22 presents experimental (circles) and simulated (dashed curves) resonance frequencies (ω) and loss rates (γ). An excellent agreement is obtained. In Figure 5.22 (a, c, we observe a crossing of resonance frequencies (ω_A and ω_B) and an avoided crossing of loss rates (γ_A and γ_B) for P_y = 400 nm. In Figure 5.22 (b, d), an avoided crossing of resonance frequencies (ω_A and ω_B) and a crossing of loss rates (γ_A and γ_B) are observed for P_y = 430 nm. An EP singularity thus unambiguously occurs

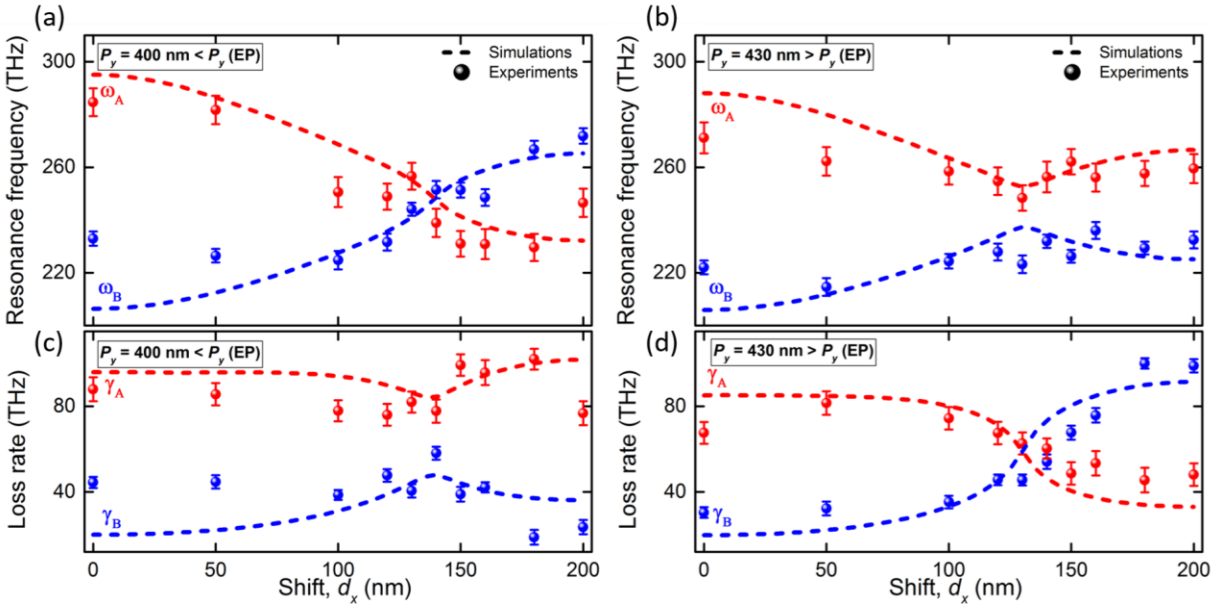

Figure 5.22 Experimental observation of plasmonic EP. Experimental (circles) and simulated (dashed) resonance frequencies and loss rates as a function of d_x for two different P_y (a, c) Crossing of the resonance frequencies and avoided crossing of the loss rates for P_y = 400 nm. (b, d) Avoided crossing of the resonance frequencies and crossing of the loss rates for P_y = 430 nm.

around ~ 243 THz for d_x of ~ 134 nm and for P_y between 400 nm and 430 nm. It is worth noting that the ambiguity on whether modes are crossing or avoiding each other as one approaches the singularity can be lifted using experimental residues around the EP.

Instead of the spatial structure of the mode, to identify the modes experimentally, we also plot the residues as in simulations. We plotted in Figure 5.23 (a-b) for P_y = 430 nm, the real and imaginary parts of the residues. We clearly observe that the separation of residues reaches a maximum on the imaginary part for P_y = 430 nm as dx varies and reaches a minimum on the imaginary part for the same P_y. By using the same rationale, we discriminated between crossing and avoided crossing in our experiments.

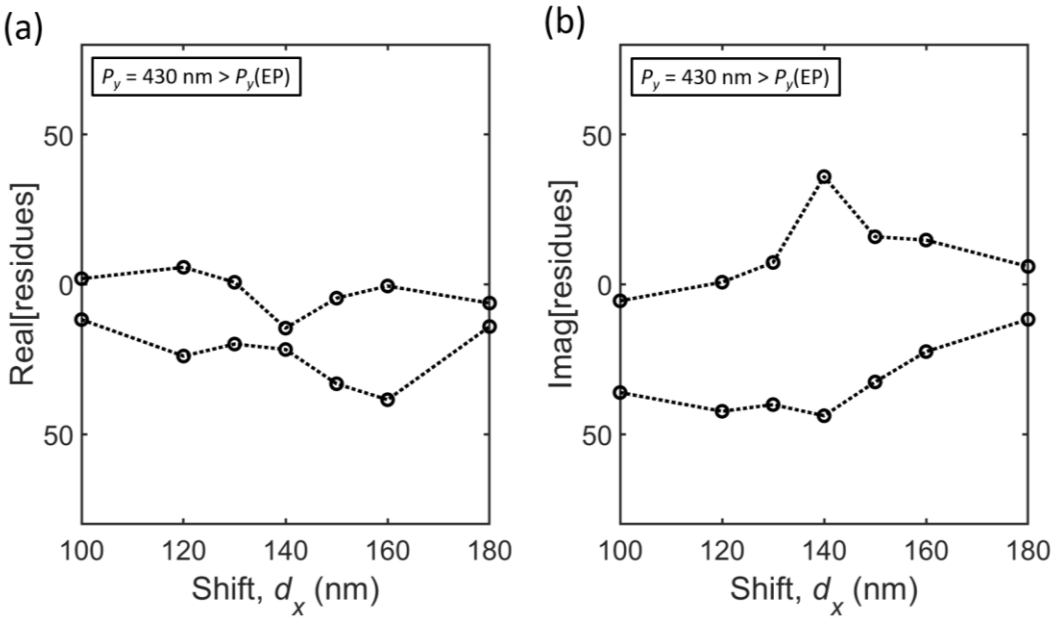

Figure 5.23 Experimental results of the residues for P_y = 430 nm as a function of the shift (d_x = 100, 120, 130, 140, 150, 160 and 180 nm). (a) For d_x = 140 nm where resonance frequencies avoided while (b) The loss rate crossed, the maximum separation is observed in the imaginary part of residues.

5.10 Conclusions

In this chapter, we introduce non-Hermitian singularities, exceptional points where eigenvalues and eigenstates coalesce simultaneously. EPs exist in open multimode systems, and the challenge of their observation resides in the identification of real physical parameters, that is, simple geometrical parameters that enable their implementation. We consider a plasmonic multilayer structure made of two optically dissimilar plasmonic resonator array with detuned resonances. Breaking the symmetry of a hybridized system makes it possible to interference via radiation. The interplay between near-field Coulomb interactions (mostly controlled by d_x) and radiative coupling via interference enables (mostly controlled by P_y) the coalescence of the hybrid modes. For the calculation of complex eigenvalues, we use the rational fitting method, and diverging residues of scattering matrix are found to prove the existence of plasmonic exceptional points in a hybridized system. The experimental observation of plasmonic EP is first demonstrated in plasmonic resonators array. The ability to drive plasmons to EPs will enable the exploration of their topological physics at small scales optoelectronic devices based on topological polaritonic effects. The realization of subwavelength non-Hermitian singularities will also shine new light on theoretical and experimental quantum theories of correlated systems.

Chapter 5, in part, is a reprinted of the materials as it appears in J.-H. Park, A. Ndao, W. Cai, L.Y. Hsu, A. Kodigala, T. Lepetit, Y.-H. Lo, and B. Kanté, "Symmetry-breaking-induced plasmonic exceptional points and nanoscale sensing", *Nat. Phys*, **16**, 462 (2020). This work was co-authored by the dissertation author was the primary researcher and author of this paper.

CHAPTER 6: Enhanced Sensitivity at EP Sensor

6.1 Introduction

Optical resonators are prime candidates for ideal optical sensors due to their ability to confine light waves in a small volume. These technologies are usually based on non-destructive probing utilizing enhanced wave-matter interaction at resonances. The interaction of waves with a sensor thus requires the latter to be an open system, i.e., a non-Hermitian system described by both radiative and absorptive processes. EPs singularities arise only in the non-Hermitian system, which modifies the topology of the system, and it appears skewed with reduced dimensionality but enhanced sensitivity [103], [104].

Plasmonic-based sensors are sensitive to the local refractive index changes that occur when target analyte binds to the surface, and thus, these sensors can transduce the binding event without labels, unlike conventional optical sensors. Owing to the capabilities of surface sensitive, label-free, and real-time measurement for binding events, a number of plasmon-based sensors have been developed, and further efforts for signal enhancement have been exerted by the enlargement of binding sites and promotion of molecular binding through suitable surface structuring within the evanescent field. In this regard, plasmon-based nanosensors have been extensively explored, in attempts to develop high-performance platforms for the detection of biological and chemical analytes. In most of the cases, plasmon band shifts caused by the specific binding of analyte molecules to ligand-modified nanoparticle surfaces are typically employed as optical sensing signals. However, the majority of studies on plasmon-based methods to date have been based on a linear shift, ie. Diabolic point configurations. In this perspective, we propose a new type of sensors based on EP that can enhance the sensitivity.

6.2 General Description of DP and EP Sensors

We assume that the sensor is a DP the unperturbed system which is described by a 2 x 2 Hamiltonian H_0 can be written as follows [89], [105]

$$H_0^{DP} = \begin{pmatrix} E_0 & 0 \\ 0 & E_0 \end{pmatrix} \tag{23}$$

with real eigenvalue E_0.

The signal to be detected is considered as a non-Hermitian perturbation εH_1 of the sensor and given by a general 2 x 2 Hamiltonian

$$H_1 = \begin{pmatrix} E_1 & A_1 \\ B_1 & E_1 \end{pmatrix} \tag{24}$$

where E_1, A_1, B_1 are complex numbers.

The full system is therefore described by the non-Hermitian matrix

$$\Delta E_{DP} = 2\varepsilon\sqrt{A_1 B_1} \tag{25}$$

The real and imaginary parts of ΔE_{DP} correspond to the conventional frequency splitting and linewidth splitting. When applying the same perturbation εH_1 to a Hamiltonian that is located at an EP where H_0 cannot be diagonalized, but it can be transformed into the form

$$H_0^{EP} = \begin{pmatrix} E_0 & A_0 \\ 0 & E_0 \end{pmatrix} \tag{26}$$

with complex eigenvalue E_0 and off-diagonal element $A_0 \neq 0$. After a straightforward calculation, we obtain the eigenvalue splitting of order $\sqrt{\varepsilon}$

$$\Delta E_{EP} = 2\sqrt{\varepsilon}\sqrt{A_0 B_1 + \varepsilon A_1 B_1} \tag{27}$$

For a sufficiently small perturbation (i.e., ε << 1), in particular, $|A_0|$ >> $|A_1|$, we find that the frequency splitting of order $\sqrt{\varepsilon}$ at an EP is larger than the splitting of order ε at a DP.

$$\Delta E_{EP} = \Delta E_{DP} \sqrt{\frac{A_0}{A_1}} \tag{28}$$

Thus, the sensitivity is enhanced at an EP if compared to a DP even though in both cases, the same perturbation H_1 is applied. For the absolute value of the frequency splitting, we obtain

$$|\Delta E_{EP}| = |\Delta E_{DP}| \sqrt{\frac{|A_0|}{|A_1|}} \tag{29}$$

The sensitivity enhancement $|\Delta E_{EP}|/|\Delta E_{DP}|$ is not dependent on the phases of the matrix elements. A_0, A_1, and B_1.

Figure 6.1 displays dramatic improvement in the scaling of EP sensors in comparison to DP (conventional) sensors. When a non-Hermitian matrix H_0 at an EP of order N (EP_N) where N eigenvalues coalesce, and their corresponding eigenvectors collapse on each other, the frequency

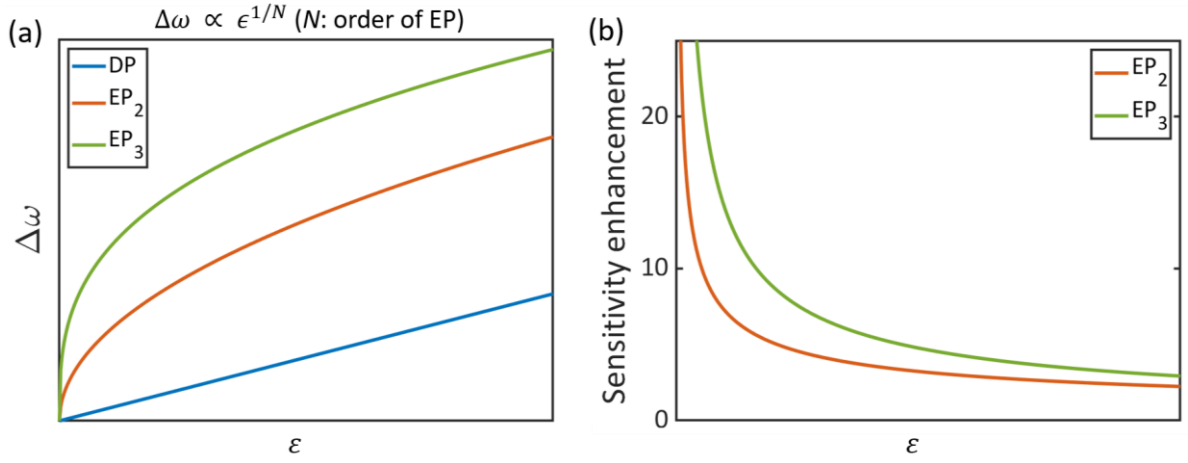

Figure 6.1 The comparison of the sensitivity of DP and EP sensors. (a) Improvement in the scaling of the sensitivity of EP sensors, (b) Dependence of the sensitivity enhancement on the perturbation strength (ε).

splitting to a perturbation of strength (ε) is expected to follow an Nth-root behavior ($\varepsilon^{1/N}$). In Figure 6.1 (a), for a sufficiently small perturbation, a system tuned a second-order EP (red line) and third-order EP (green line), respectively. In stark contrast, in DP sensors, the frequency splitting is proportional to the strength of the perturbation (blue line). The larger sensitivity enhancement can be obtained for small perturbation strength in Figure 6.1 (b). The third and second-order EP of sensitivity enhancement is significantly improved in comparison to conventional devices.

6.3 Refractive Index Sensing at EP

To further investigate the enhanced sensitivity of plasmonic EP, we evaluate the multilayered structure (configuration 3 in Chapter 5) supporting a plasmonic EP and DP with a cladding layer described by a varying refractive index constituting the perturbation δ for different thickness (h_c), 30, 40, 70 and 100 nm, respectively. Figure 6.2 displays the comparison of plasmonic EP and DP with a refractive variation. The dimensions are chosen to support either a plasmonic exceptional point (EP) [P_x = 400 nm, P_y = 415 nm, and d_x = 134 nm] or a diabolic point (DP) [P_x = 400 nm, P_y = 350 nm, and d_x = 161 nm]. As seen in Figure 6.2 (a, c, e, g), the nanosensor operating around an EP (red line) exhibits resonance splitting (Δω) proportional to the square-root of the perturbation $\Delta\omega_{EP} \sim\sqrt{\delta}$ whereas the DP nanosensor (blue line) exhibits resonance splitting that depends linearly on the perturbation $\Delta\omega_{DP} \sim\delta$. For h_c = 30 nm, the improvement in scaling of the sensitivity of EP sensor ranges over the cladding index of 1.20. This implies that those ranges of cladding index are small perturbations where EP sensors get enhanced sensitivity than DP sensors. However, for h_c = 100 nm, DP sensors surpass the EP sensor around the cladding index of 1.14. The strength of perturbation depends on not only the cladding index but also cladding layer thickness. The power laws are confirmed by log plot in Figure 6.2 (b, d, f, h) with slopes of

0.5 and 1.0 for EP (P_x = 400 nm, P_y = 415 nm, and d_x = 134 nm) and DP (P_x = 400 nm, P_y = 350 nm, and d_x = 161 nm) nanosensor respectively. The square root dependence on the perturbation constitutes additional evidence of the successful implementation of a plasmonic EP.

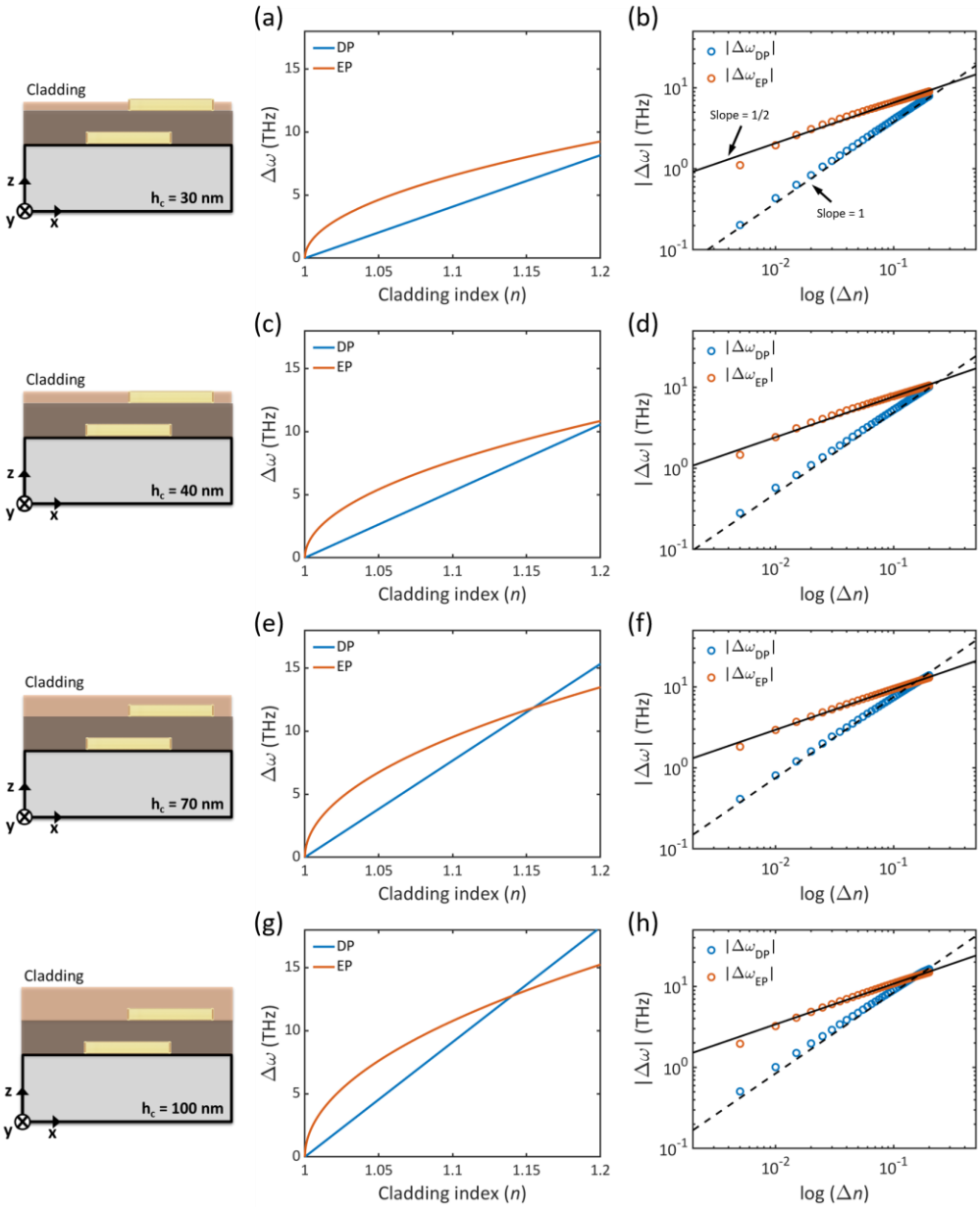

Figure 6.2 The dependence of resonance splitting on the perturbation (n). (a, c, e, g) Resonance splitting described by a refractive index varying from 1 to 1.2 for different cladding layer thickness (h_c), 30, 40, 70, 100 nm, respectively. (b, d, f, h) Dependence of the logarithm of resonance splitting for EP (red circle) and DP (blue circle) on the logarithm of Δn.

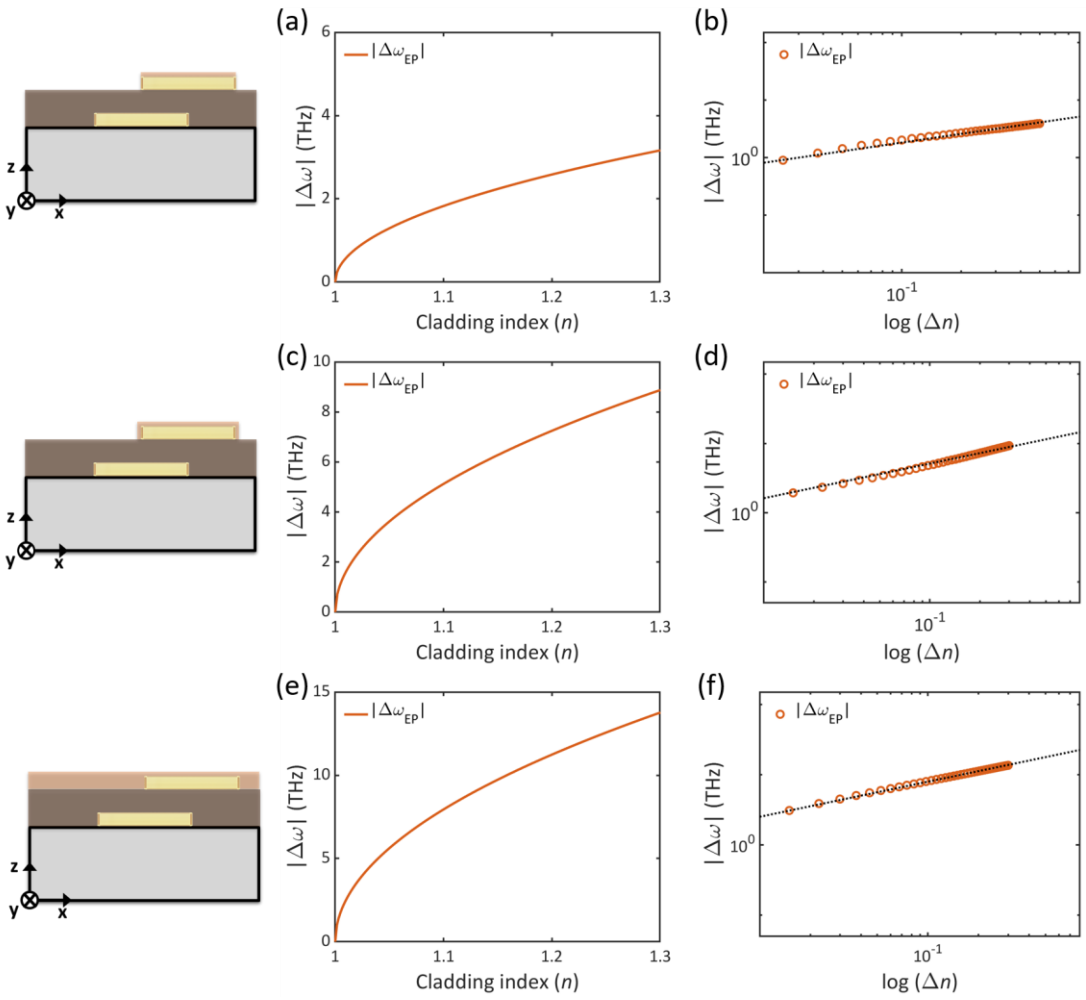

Figure 6.3 The calculated frequency splitting with three different configurations for refractive sensing. (a) The analyte is on the top of a gold bar. (b) The sensing analyte surrounds the gold bar. (c) The cladding layer covers whole structures. The three different configurations show square-root responses, and the power laws confirm the existence of an exceptional point.

We further analyzed the scaling of modes by localizing the index perturbation to the metallic bars with three different configurations (index perturbation just on top of the bars, index perturbation around the bars, and index perturbation on all substrate). In Figure 6.3, the nanosensor operating around an EP exhibits resonance splitting (Δω) proportional to the square-root of the perturbation, and the power laws are confirmed by log plot with slopes of 0.5. This is because, in

plasmonics, the field is concentrated on the plasmonic particle. The power laws confirm the evidence of the existence of EP in the plasmonic structure.

6.4 Plasmonic EP Sensor for Immuno-assay Nanosensing

Plasmons, the collective oscillation of free electrons coupled to photons, shrinks the wavelength of light to electronics and molecular length scales. Molecular nanosensing, i.e., the ability to detect extremely small quantities, enables the detection of threats at an early stage and will revolutionize security and medicine. We, therefore, evaluate immuno-assay nanosensing with a plasmonic EP. The sensing of anti-Immunoglobulin G (IgG), the most abundant immunoglobulin isotype in human serum. The measurement of IgG can be a diagnostic tool for certain conditions, such as autoimmune hepatitis [106]. Therefore, the development of EP sensing devices for the detection of proteins will have the potential to be adopted to daily life and field applications.

In order to demonstrate the immuno-assay nanosensing with a plasmonic EP, we first carry out chemical surface modification, which selectively binds the protein anti-IgG on the gold surface. The gold nanorods were first coated with a self-assembled monolayer (linker) by submerging a clean device in an ethanolic solution of 0.1M 8-Mercaptooctanoic acid (MOA) (Sigma Aldrich, 675075) overnight at 4°C. The device was then activated by standard EDC (Thermo Fisher, 22980)/NHS (Sigma Aldrich, 130672) (Ethyl-3-(3-dimethylaminopropyl)-carbodiimide/N-hydroxysuccinimide) chemistry. Briefly, the carboxyl ends of the MOA were activated by reaction with EDC (0.4M) and NHS (0.1M) in 4-morpholino ethane sulfonic acid (MES) buffer at pH 6.5 for 35 mins. After drying, the device was incubated with 100 µL/mL anti-CD63 antibodies (Ancell, 215-820) for one hour at room temperature. The surfaces were subsequently blocked with 5% bovine serum albumin (BSA) (Sigma Aldrich, A8531) in

phosphate-buffered salines (PBS) (Thermo Fisher, 10010023) for 30 mins. After rinsing with PBS, the device was immersed in anti-Mouse IgG (Sigma Aldrich, B7264) of a given concentration overnight at 4°C (Figure. 6.4).

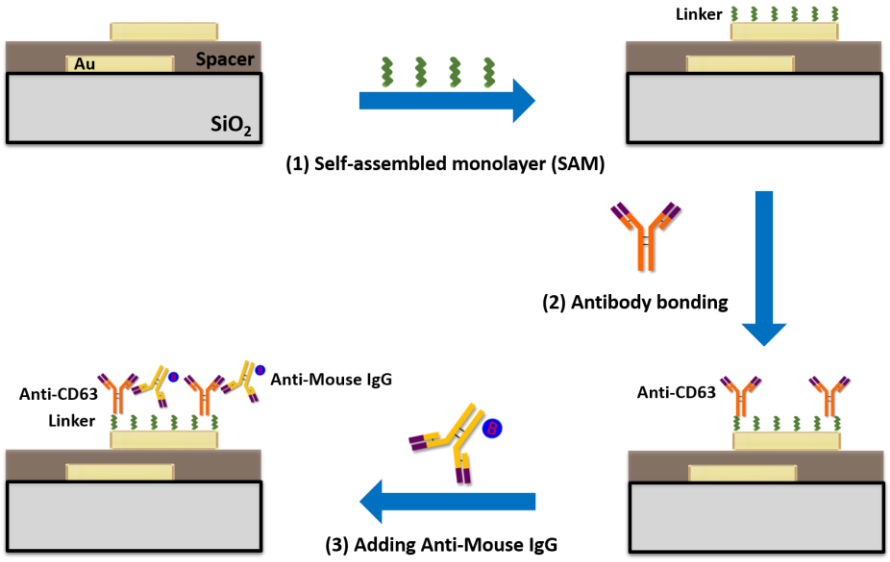

Figure 6.4 The nanosensors are functionalized using the following protocol. In step (1), the sensor was immersed in an ethanolic solution to form a self-assembled monolayer (SAM). In step (2), anti-CD63 was immobilized at room temperature on the sensor. After rinsing with phosphate-buffered salines (PBS), the sensor was immersed [step (3)] in anti-Mouse IgG overnight at 4 ºC.

The stock anti-IgG was diluted in PBS in a serial dilution (1.0 nM, 100 fM, 10 fM, 100 aM) to prepare the solution. The stock concentration is based on the datasheet from the supplier (Sigma Aldrich). To make this serial, we first added a 10 µL solution into 90 µL PBS. For 50 aM, we took 20 µL of 100 aM solution and then added it to 20 µL PBS.

To evaluate plasmonic DP and EP sensors with varying concentrations, we develop a systematic cleaning method. To clean the nanosensor after each functionalization for different concentrations, we used NH_4OH-H_2O_2-H_2O solution. The volume ratio of 1:1:5 of NH_4OH-H_2O_2-

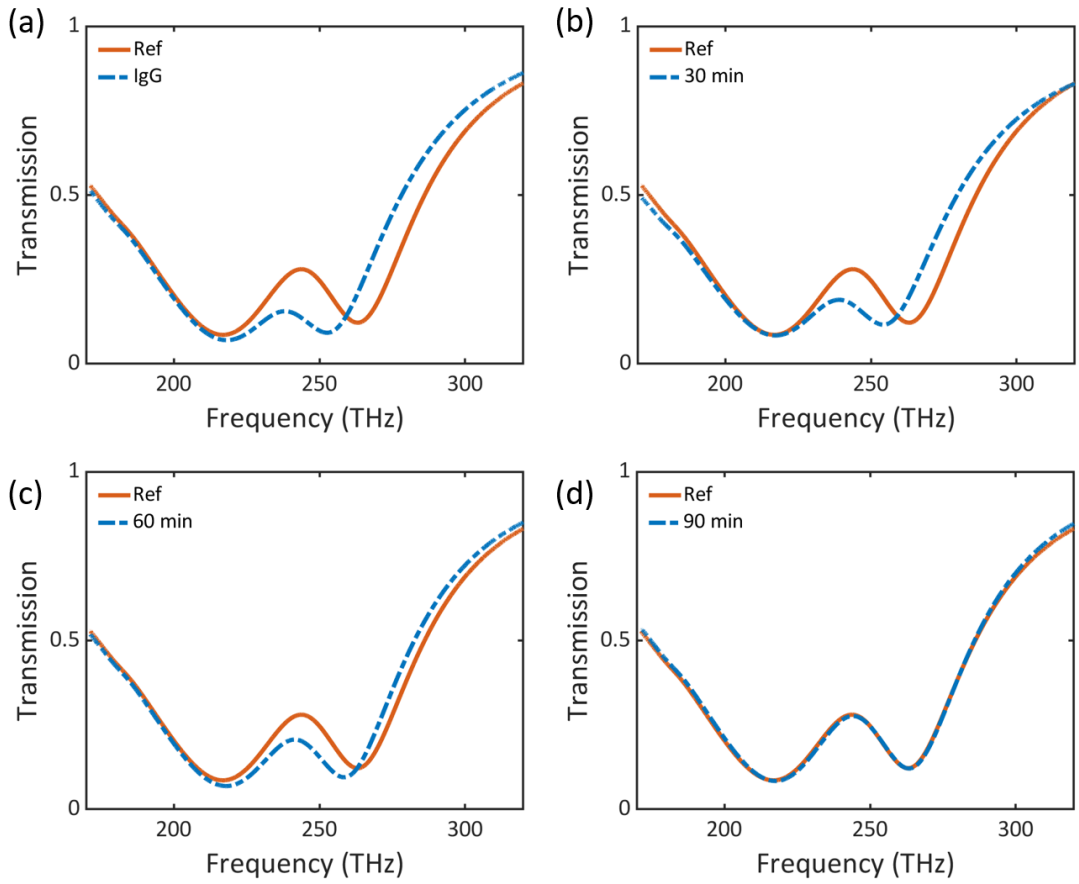

Figure 6.5 Transmission spectra as a function of SAM of anti-IgG soaking time in NH_4OH-H_2O_2-H_2O solution. (a) Transmission after functionalization (1000 aM). (b) Transmission after 30 min immersion. (c) Transmission after 60 min immersion. (d) Transmission after 90 min immersion.

H_2O is employed at room temperature for various fixed soaking times (30, 60, 90 min). The removal of the self-assembled monolayer (SAM) denoted linker on the sample was studied using Fourier-transform infrared spectroscopy (FTIR). With the FTIR, we first compare the Transmission after functionalization (Figure 6.5 (a)) to the nanosensor without functionalization as the reference. The second step consists of measuring the transmission spectra as a function of the soaking time of SAM with anti-Mouse IgG. Figure 6.5 (b-d) shows the transmission spectra of different time using NH_4OH-H_2O_2-H_2O solution. First, the device was immersed in the solution for 30 min (Figure 6.5 (b)) at room temperature, then washed using IPA and DI water, and dried

by N_2. The transmission spectra after the first 30 min and cleaning process show the transmission shifted to a higher frequency (blueshift in wavelength). We then repeat the process three times with 30 min steps (Figure 6.5 (b-d)). The transmission spectra gradually shifted toward the transmission before functionalization. After the third immersion process, the transmission spectra are well-matched with the initial nanosensor response without functionalization (Figure 6.5 (d)). This clearly shows that our structure is clean and can be functionalized again for different concentrations. The FTIR measurement ensures that the nanosensor is well cleaned and also that the sensor is still operational.

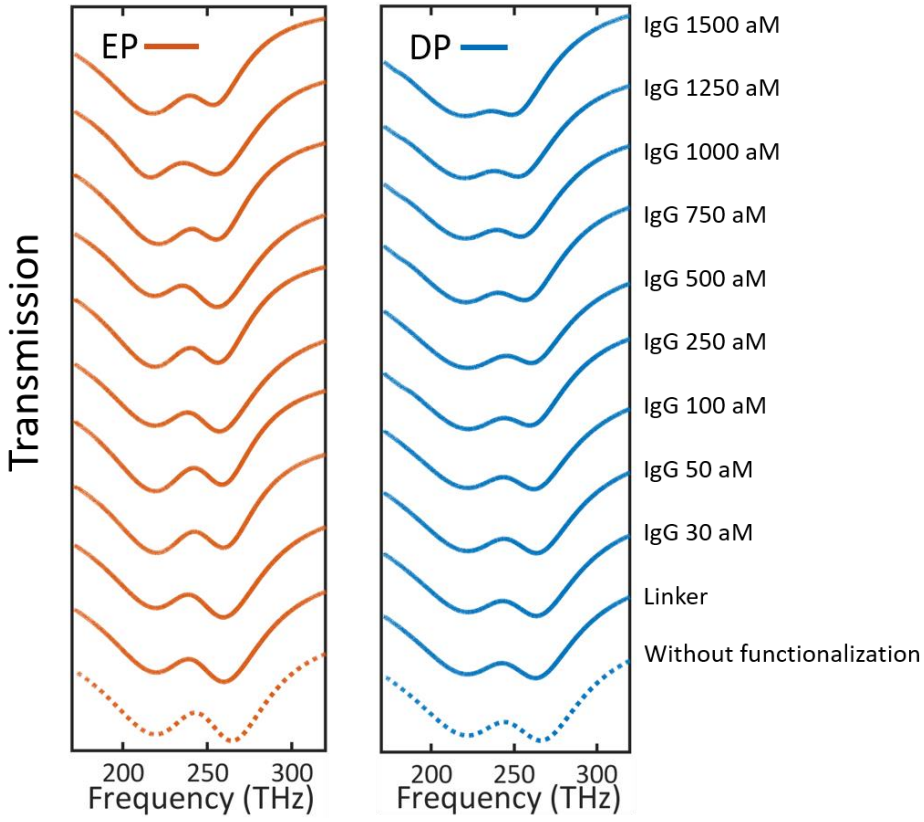

Figure 6.6 Raw data of measured transmission spectra without functionalization, with the linker and with various concentrations of Anti-IgG. (Left) Exceptional point (EP), (right) Diabolic point (DP) sensor, respectively.

Next, we measure the resonance splitting for DP and EP sensors with varying anti-IgG concentration (30 to 1500 aM). First, the FTIR spectra are measured using 128 scans and with a spectral resolution of $4cm^{-1}$. The measured transmission spectra are presented in Figure 6.6.

The raw data of phase measurements are also presented in Figure 6.7. The phases of the sample with varying concentrations are measured using broadband spectrally and spatially resolved interferometer (SSRI). The complex poles are extracted using the methods presented in chapter 5. The critical role of the phase-in recovering the poles, as previously discussed in chapter 5.

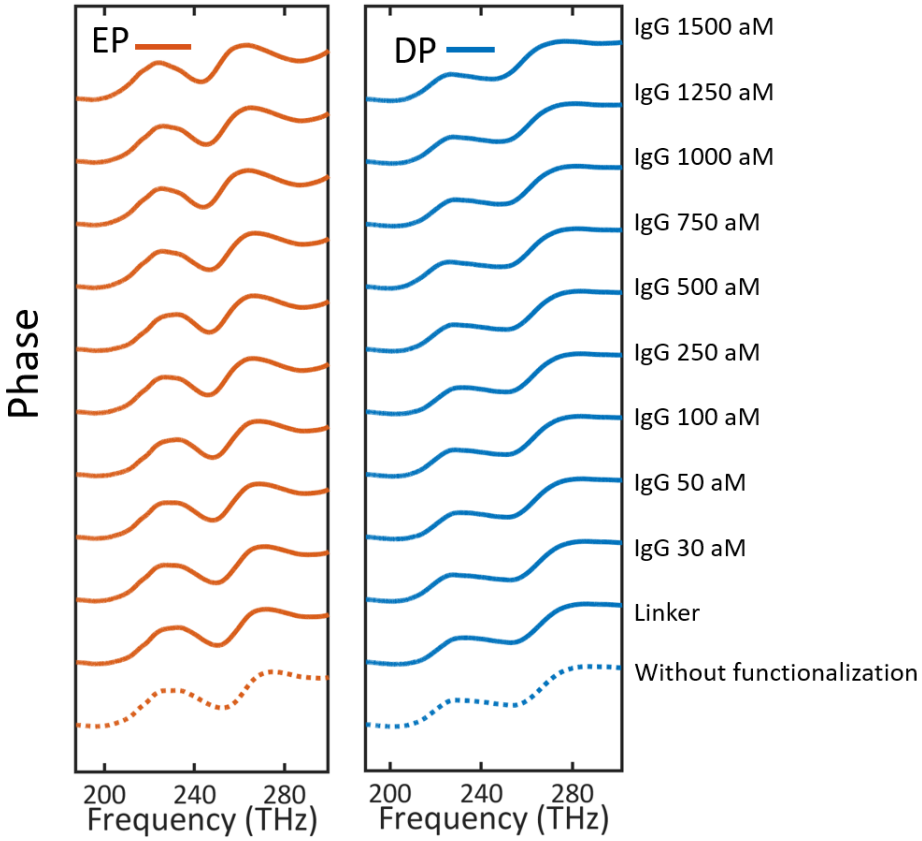

Figure 6.7 Raw data of measured phase of samples without functionalization, with the linker and with various concentrations of Anti-IgG. (Left) Exceptional point (EP), (right) Diabolic point (DP) sensor, respectively.

The periodicity in Y-direction for the EP sensor in Figure 6.8 is especially chosen to be P_y = 415 nm to bring the system closer to the singularity. According to Figure 6.2, larger resonance splitting is expected for the DP nanosensor for large perturbations, and the EP nanosensor should exhibit larger splitting for small enough perturbations. Resonance splitting for EP and DP sensors are presented in Figure 6.8 as histograms (red and blue, respectively). Using the same sample, that is functionalized, cleaned (see Figure 6.5), and functionalized again, various concentrations are

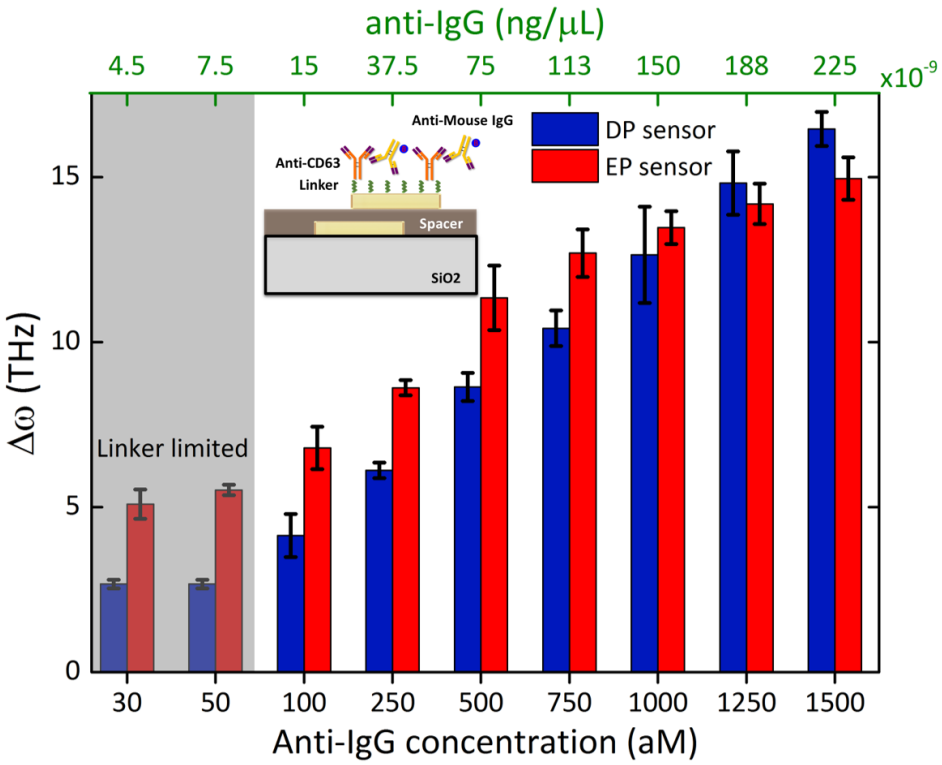

Figure 6.8 Immuno-assay nanosensing with a plasmonic exceptional point. Histograms are presenting the measured resonance splitting for different concentrations of Anti-Mouse IgG for the Diabolic Point (DP, blue histograms) and Exceptional Point (EP, red histograms) sensors.

compared. Starting with 1500 aM, larger splitting for the DP nanosensor is first observed ($\Delta\omega_{DP} > \Delta\omega_{EP}$). We then progressively decreased the concentration of IgG and observed a larger splitting of resonances for the EP nanosensor compared to the DP nanosensor for concentration smaller than 1 fM ($\Delta\omega_{EP} > \Delta\omega_{DP}$). This confirms that the EP indeed becomes slightly more sensitive when

the perturbation is small. We further reduced the concentration, and, noticed, interestingly, that when the concentration is decreased from 50 aM to 30 aM, the splitting of the DP nanosensor does not change anymore. At the same concentrations, the splitting of the EP nanosensor is still larger than that of the DP sensor, but, the change in the splitting from 50 aM to 30 aM is also small.

To understand this saturation, we measured the splitting for the sample solely covered with the linker. The measured splittings are about 2.4 THz for the DP sensor and about 5.1 THz for the EP sensor, coinciding with the minimum splitting measured with IgG concentrations of 50 aM and 30 aM. We thus concluded that the smallest concentration of IgG that can be measured with our system had been reached. At those concentrations, sensing is thus limited by the linker that itself constitutes a perturbation while 50 aM and 30 aM or smaller concentrations of IgG in the complex linker/IgG are similar perturbations dominated by the more perturbative linker as shown in Figure 6. 9.

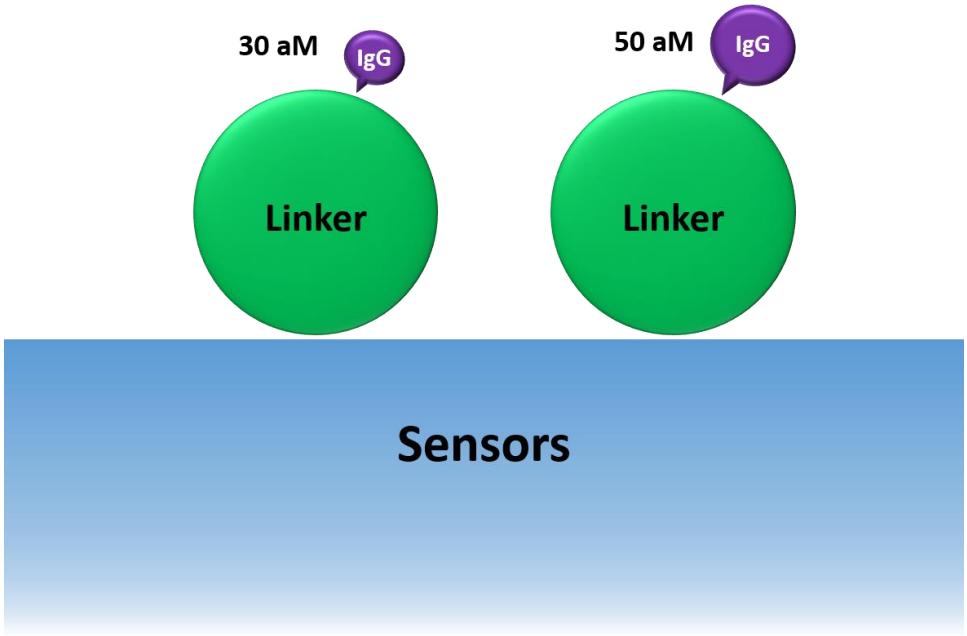

Figure 6.9 Schematic of the linker/IgG sensing with two different concentrations. The perturbation due to the linker is dominant compared to IgG for IgG concentration smaller than 50 aM.

There is always a finite difference between the resonance frequencies of the two modes that coalesce at the EP in fabricated samples. Therefore, we also investigate the effect of fabrication imperfections on the resonance splitting. The calculated fabrication error of 5 nm on d_x and P_y, for example (resolution of our fabrication), already induces a mode splitting of 6 THz. Figure 6.10 presents the shift due to the linker is thus smaller than the shift induced by fabrication errors. Fig 6.10 (b) shows the non-symmetric resonance splitting of fabrication imperfection of P_y. The smaller P_y from EP is the region where resonance frequencies cross, which gives rise to less sensitivity to the imperfection. In fact, P_y imperfection in fabrication is negligible, which is ± 1 nm in the experiment. Most of the fabrication errors originate from the imperfection of d_x. We can

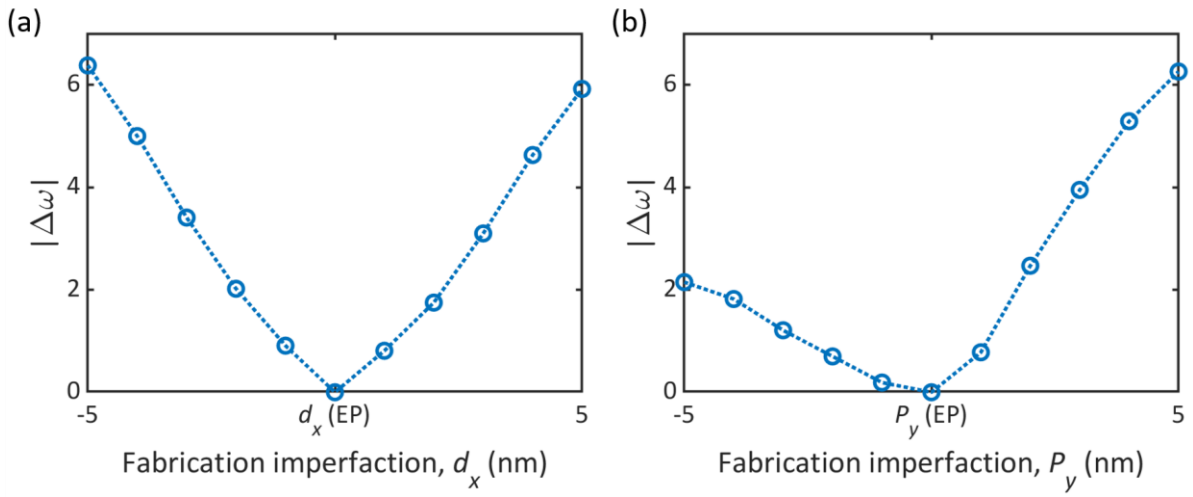

Figure 6.10 Calculated resonance splitting as a function of the deviation. (a) d_x (± 5 nm) from the perfect EP system (b) P_y (± 5 nm) from the perfect EP system.

thus not guarantee, with the fabrication method used, to bring the complex sensor+linker exactly at the EP point, and, we can only approach the singularity. It is worth noting that a fabrication error of ± 5 nm (resolution of our fabrication) on d_x, for example, for the sensor exactly at the EP, already induces a mode splitting of about 6 THz, comparable to the linker induced shift.

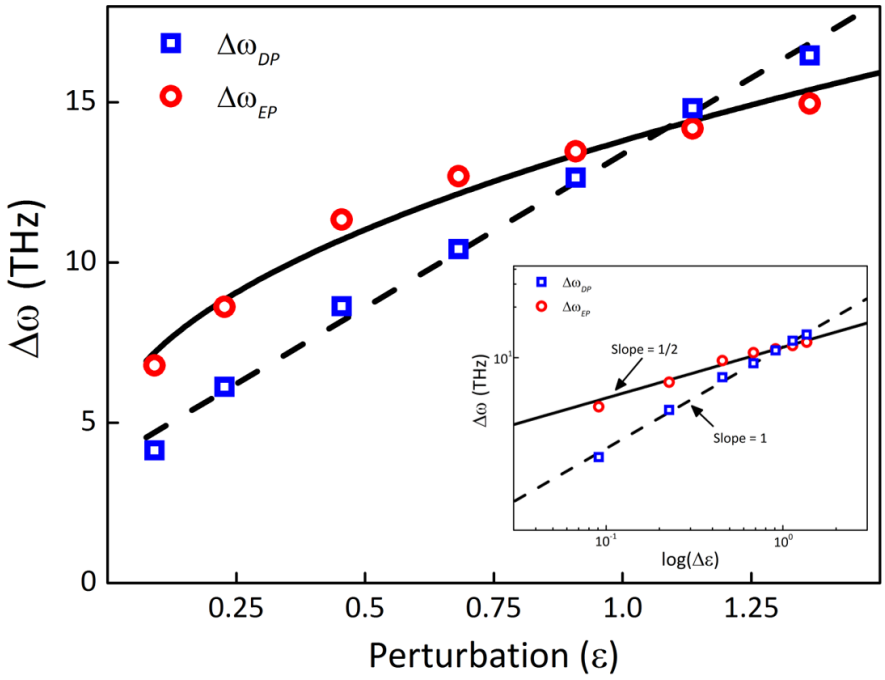

Figure 6.11 Scaling of resonance splitting for concentrations from 100 aM to 1500 aM as a function of the perturbation. ε = (Anti-IgG concentration aM)/(1100 aM) for the EP and DP sensors.

With this analysis, the power dependence can be analyzed as soon as IgG induces further mode splitting. The linker can thus be neglected for concentrations between 100 aM and 1500 aM, and we plotted, in Figure. 6.11, resonance splitting as a function of IgG concentration that can be regarded as index perturbation according to reference [107]. Very interestingly, the DP and EP mode splitting obey a linear and square-root law, respectively, constituting a direct demonstration of a plasmonic EP sensor. Plasmonic sensors are usually compared using their sensitivity per refractive index unit in various regimes determined by the minimum molecular weight they detect. The nanohole array was reported with a sensitivity of 671 nm/RIU and detected sub-10^{-6} g/L concentrations [108]. The hyperbolic metamaterial was reported with 30000 nm/RIU sensitivity for a minimum detection of 2440x10^{-12} g/L [109]. Our EP system has a sensitivity of 4821 nm/RIU

and detects $15x10^{-12}$ g/L and thus operates in a regime not reached by previous plasmonic array sensors. This mostly stems from the coherent detection technique used in our experiments.

6.5 Conclusions

We numerically and experimentally demonstrate the enhanced sensitivity of a plasmonic sensor operating at an EP where at least two eigenmodes of an open system coalesce to become degenerate both in their resonance frequencies and loss rates. EP and DP sensors with cladding layer described by a varying refractive index constituting the perturbation δ for different thickness is compared to demonstrate sensitivity enhancement. The resonance splitting of EP nanosensor is proportional to the square-root of the perturbation $\Delta\omega_{EP,}$ whereas the DP nanosensor exhibits resonance splitting that depends linearly on the perturbation. The power laws confirm the evidence of the existence of EP in the plasmonic structure.

The enhanced sensing of anti-Immunoglobulin G, the most common antibody found in blood circulation, is enabled using plasmonic EP sensors at attomolar concentrations. We evaluate immuno-assay nanosensing with a plasmonic EP. The DP and EP mode splittings obey a linear and square-root law, respectively, constituting a direct demonstration of a plasmonic EP sensor. The square-root topology of the eigenvalue is successfully proven in a hybridized plasmonic structure. Plasmonic EPs could open a new avenue toward engineering ultrasensitive compact nanoscale sensors for complex molecules, nanoparticles, and other targets of interest.

Chapter 6, in part, is a reprinted of the materials as it appears in J.-H. Park, A. Ndao, W. Cai, L.Y. Hsu, A. Kodigala, T. Lepetit, Y.-H. Lo, and B. Kanté, "Symmetry-breaking-induced plasmonic exceptional points and nanoscale sensing", *Nat. Phys*, **16**, 462 (2020). This work was co-authored by the dissertation author was the primary researcher and author of this paper.

CHAPTER 7: Summary and Outlook

In this dissertation, we have investigated plasmon coupling strength and range in multilayered structures and explored non-Hermitian singularities, Exceptional Points (EPs), where eigenmodes coalesce in plasmon hybridization system and their sensing capabilities both experimentally and numerically. A novel sensing platform based on the multilayered structures is proposed and exhibits enhanced sensitivity at exceptional points.

The first part of this dissertation deals with the detailed investigation of the optical properties of the plasmon hybridization system as well as nanorods array with different geometries. We have demonstrated that the plasmon hybridization method, which is generally applied to describe electric interaction in the multilayered plasmonic nanostructure. The hybridized system supports two modes: a symmetric and an antisymmetric. The lateral shift of the top nanorod leads to the inversion of the hybridization scheme. This inversion provides an intuitive of the near-field coupling between two nanorods. We have introduced nanofabrication procedures for manufacturing multilayer plasmonic nanostructures, which provides a general EBL recipe for the implementation of 3D nanodevices or even bulk plasmonic structure at optical frequencies in the future. We also proposed a novel sensing platform based on plasmon hybridize to get enhanced sensitivity. The sensing capability of a hybridized plasmonic system exhibits a superior sensor to a standard single plasmonic resonance system. The FOM is a factor of 4 greater in the hybridized case using the antisymmetric mode. Furthermore, the antisymmetric mode of the hybridized system has a higher sensitivity and FOM compared to the electric dipolar mode regardless of the lateral shift of the top nanorod.

The second part of this dissertation introduces non-Hermitian singularities, exceptional points where eigenvalues and eigenstates coalesce simultaneously. Because EPs exist in open

multimode systems, we propose a novel approach to EPs based on spatial symmetry breaking. The plasmonic EPs are based on the hybridization of detuned resonances in multilayered plasmonic structures to reach a critical complex coupling rate between nanoantenna arrays, resulting in the simultaneous coalescence of the resonances and loss rates. The hybridization of optically dissimilar resonators, however, led to two-hybrid modes with crossing and avoided crossing of both the resonances and loss rates, unambiguously demonstrating the existence of a plasmonic EP where resonances and loss rates become simultaneously degenerate. Breaking the symmetry of a hybridized system makes it possible to interference via radiation. The interplay between near-field Coulomb interactions (mostly controlled by d_x) and radiative coupling via interference enables (mostly controlled by P_y) the coalescence of the hybrid modes. To observe EP in the experiment, we measure the amplitude and phase of transmitted light by using a Fourier-transformed infrared spectrometer and custom spatially and spectrally resolved broadband interferometer, respectively, and extracted the complex eigenvalues. The experimental observation of plasmonic EP is first demonstrated in plasmonic resonators array by demonstrating crossing and avoided crossing of both the resonances and loss rates. The ability to drive plasmons to EPs will enable the exploration of their topological physics at small scales optoelectronic devices based on topological polaritonic effects. The realization of subwavelength non-Hermitian singularities will also shine new light on theoretical and experimental quantum theories of correlated systems.

The last part of this dissertation presents the enhanced sensitivity of a plasmonic sensor operating at an EP. DP and EP sensors with the cladding layer described by a varying refractive index constituting the perturbation δ for different thicknesses are compared. The resonance splitting of EP nanosensor is proportional to the square-root of the perturbation $\Delta\omega_{EP,}$ whereas the DP nanosensor exhibits resonance splitting that depends linearly on the perturbation. The power

laws confirm the evidence of the existence of EP in the plasmonic structure. The exceptional points are used as sensors of anti-immunoglobulin G, the most abundant immunoglobulin isotype in human serum. In this part, we demonstrate, for the first time, a new type of sensors that are 267 more sensitive than the current states of the art of nanosensors.

We numerically and experimentally demonstrate the enhanced sensitivity of a plasmonic sensor operating at an EP where at least two eigenmodes of an open system coalesce to become degenerate both in their resonance frequencies and loss rates. EP and DP sensors with cladding layer described by a varying refractive index constituting the perturbation δ for different thickness is compared to demonstrate sensitivity enhancement. The resonance splitting of EP nanosensor is proportional to the square-root of the perturbation $\Delta\omega_{EP,}$ whereas the DP nanosensor exhibits resonance splitting that depends linearly on the perturbation. The power laws confirm the evidence of the existence of EP in the plasmonic structure.

Plasmonic EPs offer the possibility to obtain enhanced sensitivity to small perturbation, which does not occur in conventional plasmonic sensors. The proposed EP sensing platform is suitable for biomedical sensing due to the ability to detect extremely low concentration. Recently, active researches have been developed the plasmonic platforms for manipulating the local field to enhance chiroptical signals [110], [111]. This plasmonic EP will offer new possibilities of chiral sensing with high sensitivity, such as the essential amino acids, protein, and DNA. The implementation of an exceptional point of order higher than two in plasmonic offers ultra-high sensitivity enhancement. The existence of second-order modes of magnetic resonance makes it possible to merge multiple eigenmodes. Further investigation is needed to determine geometrical parameters to control the near and far-field coupling.

REFERENCES

[1] R. W. Wood, "On a remarkable case of uneven distribution of light in a diffraction grating spectrum," *Proc. Phys. Soc. London*, vol. 18, no. 1, p. 269, 1902.

[2] R. W. Wood, "XXVII. Diffraction gratings with controlled groove form and abnormal distribution of intensity," *London, Edinburgh, Dublin Philos. Mag. J. Sci.*, vol. 23, no. 134, pp. 310–317, 1912.

[3] L. Rayleigh, "On the dynamical theory of gratings," *Proc. R. Soc. London. Ser. A, Contain. Pap. a Math. Phys. Character*, vol. 79, no. 532, pp. 399–416, 1907.

[4] E. Kretschmann, "Determination of optical constants of metals by excitation of surface plasmons," *Zeitschrift Fur Phys.*, vol. 241, no. 4, p. 313, 1971.

[5] A. Otto, "Excitation of nonradiative surface plasma waves in silver by the method of frustrated total reflection," *Zeitschrift für Phys. A Hadron. Nucl.*, vol. 216, no. 4, pp. 398–410, 1968.

[6] E. Prodan, C. Radloff, N. J. Halas, and P. Nordlander, "A hybridization model for the plasmon response of complex nanostructures," *Science (80-.).*, vol. 302, no. 5644, pp. 419–422, 2003.

[7] A. Christ, O. J. F. Martin, Y. Ekinci, N. A. Gippius, and S. G. Tikhodeev, "Symmetry breaking in a plasmonic metamaterial at optical wavelength," *Nano Lett.*, vol. 8, no. 8, pp. 2171–2175, 2008.

[8] B. Kanté, S. N. Burokur, A. Sellier, A. De Lustrac, and J.-M. Lourtioz, "Controlling plasmon hybridization for negative refraction metamaterials," *Phys. Rev. B*, vol. 79, no. 7, p. 75121, 2009.

[9] F. Hao, P. Nordlander, Y. Sonnefraud, P. Van Dorpe, and S. A. Maier, "Tunability of subradiant dipolar and Fano-type plasmon resonances in metallic ring/disk cavities: implications for nanoscale optical sensing," *ACS Nano*, vol. 3, no. 3, pp. 643–652, 2009.

[10] F. Hao, Y. Sonnefraud, P. Van Dorpe, S. A. Maier, N. J. Halas, and P. Nordlander, "Symmetry breaking in plasmonic nanocavities: subradiant LSPR sensing and a tunable Fano resonance," *Nano Lett.*, vol. 8, no. 11, pp. 3983–3988, 2008.

[11] Y. Sonnefraud, N. Verellen, H. Sobhani, G. Vandenbosch, V. Moshchalkov, P. Van Dorpe, P. Nordlander, and S. Maier, "Experimental realization of subradiant, superradiant, and Fano resonances in ring/disk plasmonic nanocavities," *ACS Nano*, vol. 4, no. 3, pp. 1664–1670, 2010.

[12] D. Dregely, M. Hentschel, and H. Giessen, "Excitation and tuning of higher-order Fano resonances in plasmonic oligomer clusters," *ACS Nano*, vol. 5, no. 10, pp. 8202–8211, 2011.

[13] M. Hentschel, D. Dregely, R. Vogelgesang, H. Giessen, and N. Liu, "Plasmonic oligomers: the role of individual particles in collective behavior," *ACS Nano*, vol. 5, no. 3, pp. 2042–2050, 2011.

[14] M. Hentschel, M. Saliba, R. Vogelgesang, H. Giessen, A. P. Alivisatos, and N. Liu, "Transition from isolated to collective modes in plasmonic oligomers," *Nano Lett.*, vol. 10, no. 7, pp. 2721–2726, 2010.

[15] G.Bachelier, I. Russier-Antoine, E. Benichou, C. Jonin, N. Del Fatti, F. Vallée, and P-F. Brevet, "Fano profiles induced by near-field coupling in heterogeneous dimers of gold and silver nanoparticles," *Phys. Rev. Lett.*, vol. 101, no. 19, p. 197401, 2008.

[16] C. S. T. MWS, "Computer Simulation Technology: Microwave Studio," *Comput. Simul. Technol. Std*, 2011.

[17] P. B. Johnson and R.-Wjp. Christy, "Optical constants of the noble metals," *Phys. Rev. B*, vol. 6, no. 12, p. 4370, 1972.

[18] G. V Hartland, "Optical studies of dynamics in noble metal nanostructures," *Chem. Rev.*, vol. 111, no. 6, pp. 3858–3887, 2011.

[19] J. Dorfmüller, R. Vogelgesang, R. Weitz, C. Rockstuhl, C. Etrich, T. Pertsch, F. Lederer, and K. Kern, "Fabry-Pérot resonances in one-dimensional plasmonic nanostructures," *Nano Lett.*, vol. 9, no. 6, pp. 2372–2377, 2009.

[20] R. Guo, T. K. Hakala, and P. Törmä, "Geometry dependence of surface lattice resonances in plasmonic nanoparticle arrays," *Phys. Rev. B*, vol. 95, no. 15, p. 155423, 2017.

[21] A. Ndao, A. Belkhir, R. Salut, and F. I. Baida, "Slanted annular aperture arrays as enhanced-transmission metamaterials: Excitation of the plasmonic transverse electromagnetic guided mode," *Appl. Phys. Lett.*, vol. 103, no. 21, p. 211901, 2013.

[22] P. Nordlander and E. Prodan, "Plasmon hybridization in nanoparticles near metallic surfaces," *Nano Lett.*, vol. 4, no. 11, pp. 2209–2213, 2004.

[23] B. Kanté, Y.-S. Park, K. O'Brien, D. Shuldman, N. Lanzillotti-Kimura, Z. Wong, X. Yin, and X. Zhang, "Symmetry breaking and optical negative index of closed nanorings," *Nat. Commun.*, vol. 3, no. 1, pp. 1–7, 2012.

[24] S.-C. Yang, H. Kobori, C.-L. He, M.-H. Lin, H.-Y. Chen, C. Li, M. Kanehara, T. Teranishi, and S. Gwo, "Plasmon hybridization in individual gold nanocrystal dimers: direct observation of bright and dark modes," *Nano Lett.*, vol. 10, no. 2, pp. 632–637, 2010.

[25] R. Ameling and H. Giessen, "Microcavity plasmonics: strong coupling of photonic cavities and plasmons," *Laser Photon. Rev.*, vol. 7, no. 2, pp. 141–169, 2013.

[26] N. Liu and H. Giessen, "Coupling effects in optical metamaterials," *Angew. Chemie Int. Ed.*, vol. 49, no. 51, pp. 9838–9852, 2010.

[27] H. Liu, D. Genov, D. Wu, Y. Liu, Z. Liu, C. Sun, S. Zhu, and X. Zhang, "Magnetic plasmon hybridization and optical activity at optical frequencies in metallic nanostructures," *Phys. Rev. B*, vol. 76, no. 7, p. 73101, 2007.

[28] R. Taubert, R. Ameling, T. Weiss, A. Christ, and H. Giessen, "From Near-Field to Far-Field

Coupling in the Third Dimension: Retarded Interaction of Particle Plasmons," *Nano Lett.*, vol. 11, no. 10, pp. 4421–4424, Oct. 2011, doi: 10.1021/nl202606g.

[29] N. Liu, M. Hentschel, T. Weiss, A. P. Alivisatos, and H. Giessen, "Three-Dimensional Plasmon Rulers," *Science (80-.).*, vol. 332, no. 6036, pp. 1407 LP – 1410, Jun. 2011, doi: 10.1126/science.1199958.

[30] A. Christ, O. J. F. Martin, Y. Ekinci, N. A. Gippius, and S. G. Tikhodeev, "Symmetry breaking in a plasmonic metamaterial at optical wavelength," *Nano Lett.*, vol. 8, no. 8, pp. 2171–2175, 2008, doi: 10.1021/nl0805559.

[31] W. (Walter) Hu, K. Sarveswaran, M. Lieberman, and G. H. Bernstein, "Sub-10 nm electron beam lithography using cold development of poly(methylmethacrylate)," *J. Vac. Sci. Technol. B Microelectron. Nanom. Struct. Process. Meas. Phenom.*, vol. 22, no. 4, pp. 1711–1716, Jun. 2004, doi: 10.1116/1.1763897.

[32] L. E. Ocola and A. Stein, "Effect of cold development on improvement in electron-beam nanopatterning resolution and line roughness," *J. Vac. Sci. Technol. B Microelectron. Nanom. Struct. Process. Meas. Phenom.*, vol. 24, no. 6, pp. 3061–3065, Nov. 2006, doi: 10.1116/1.2366698.

[33] F. J. Pantenburg, S. Achenbach, and J. Mohr, "Influence of developer temperature and resist material on the structure quality in deep x-ray lithography," *J. Vac. Sci. Technol. B Microelectron. Nanom. Struct. Process. Meas. Phenom.*, vol. 16, no. 6, pp. 3547–3551, Nov. 1998, doi: 10.1116/1.590494.

[34] B. Cord, J. Lutkenhaus, and K. K. Berggren, "Optimal temperature for development of poly(methylmethacrylate)," *J. Vac. Sci. Technol. B Microelectron. Nanom. Struct. Process. Meas. Phenom.*, vol. 25, no. 6, pp. 2013–2016, Nov. 2007, doi: 10.1116/1.2799978.

[35] S. Thoms, Y. Zhang, and J. M. R. Weaver, "Improved alignment algorithm for electron beam lithography," *J. Vac. Sci. Technol. B*, vol. 32, no. 6, p. 06F509, Nov. 2014, doi: 10.1116/1.4901015.

[36] J. G. Goodberlet, J. T. Hastings, and H. I. Smith, "Performance of the Raith 150 electron-beam lithography system," *J. Vac. Sci. Technol. B Microelectron. Nanom. Struct. Process. Meas. Phenom.*, vol. 19, no. 6, pp. 2499–2503, Nov. 2001, doi: 10.1116/1.1414018.

[37] S. Thoms, D. S. Macintyre, K. E. Docherty, and J. M. R. Weaver, "Alignment verification for electron beam lithography," *Microelectron. Eng.*, vol. 123, pp. 9–12, 2014, doi: https://doi.org/10.1016/j.mee.2014.02.005.

[38] M. Zhao, T. Xu, B. Chen, and J. Niu, "Technology of alignment mark in electron beam lithography," in *Proc.SPIE*, Aug. 2014, vol. 9285, doi: 10.1117/12.2068112.

[39] H. Itoh, K. Nakamura, and H. Hayakawa, "Charging effects on trilevel resist with an e-beam lithography system," *J. Vac. Sci. Technol. B Microelectron. Process. Phenom.*, vol. 8, no. 6, pp. 1893–1897, Nov. 1990, doi: 10.1116/1.585180.

[40] J. Moers, J. Gerharz, G. Rinke, G. Mussler, S. Trellenkamp, and D. Grützmacher, "Influence

of the epitaxial growth and device processing on the overlay accuracy during processing of the d-DotFET," *Thin Solid Films*, vol. 518, no. 9, pp. 2565–2568, 2010, doi: https://doi.org/10.1016/j.tsf.2009.09.155.

[41] R. Plontke, L. Bettin, D. Beyer, J. Butschke, M. Irmscher, C. Koepernik, B. Leibold, A. Vix, and P. Voehringer, "Avoidance/reduction of charging effects in case of partially insufficient substrate conductivity when using ESPACER 300Z," in *Proc.SPIE*, Jun. 2004, vol. 5504, doi: 10.1117/12.568033.

[42] T. Barwicz and H. I. Smith, "Evolution of line-edge roughness during fabrication of high-index-contrast microphotonic devices," *J. Vac. Sci. Technol. B Microelectron. Nanom. Struct. Process. Meas. Phenom.*, vol. 21, no. 6, pp. 2892–2896, Nov. 2003, doi: 10.1116/1.1625965.

[43] H. Lorenz, M. Despont, N. Fahrni, N. LaBianca, P. Renaud, and P. Vettiger, "{SU}-8: a low-cost negative resist for {MEMS}," *J. Micromechanics Microengineering*, vol. 7, no. 3, pp. 121–124, Sep. 1997, doi: 10.1088/0960-1317/7/3/010.

[44] A. del Campo and C. Greiner, "{SU}-8: a photoresist for high-aspect-ratio and 3D submicron lithography," *J. Micromechanics Microengineering*, vol. 17, no. 6, pp. R81--R95, May 2007, doi: 10.1088/0960-1317/17/6/r01.

[45] J. Carlier, S. Arscott, V. Thomy, J. Fourrier, F. Caron, J. Camart, C. Druon, and P. Tabourier, "Integrated microfluidics based on multi-layered {SU}-8 for mass spectrometry analysis," *J. Micromechanics Microengineering*, vol. 14, no. 4, pp. 619–624, Feb. 2004, doi: 10.1088/0960-1317/14/4/024.

[46] K. Kim, D. Park, H. Lu, W. Che, K. Kim, J.-B. Lee, and C. Ahn, "A tapered hollow metallic microneedle array using backside exposure of {SU}-8," *J. Micromechanics Microengineering*, vol. 14, no. 4, pp. 597–603, Feb. 2004, doi: 10.1088/0960-1317/14/4/021.

[47] N. E. S. Farrington and S. Iezekiel, "Accurate layer thickness control and planarization for multilayer SU-8 structures," *J. Micro/Nanolithography, MEMS, MOEMS*, vol. 10, no. 1, pp. 1–7, Jan. 2011, doi: 10.1117/1.3563599.

[48] A. Mata, A. J. Fleischman, and S. Roy, "Fabrication of multi-layer {SU}-8 microstructures," *J. Micromechanics Microengineering*, vol. 16, no. 2, pp. 276–284, Jan. 2006, doi: 10.1088/0960-1317/16/2/012.

[49] C. J. Robin and K. N. Jonnalagadda, "Effect of size and moisture on the mechanical behavior of {SU}-8 thin films," *J. Micromechanics Microengineering*, vol. 26, no. 2, p. 25020, Jan. 2016, doi: 10.1088/0960-1317/26/2/025020.

[50] Y. Tian, X. Shang, and M. J. Lancaster, "Fabrication of multilayered SU8 structure for terahertz waveguide with ultralow transmission loss," *J. Micro/Nanolithography, MEMS, MOEMS*, vol. 13, no. 1, pp. 1–7, Jan. 2014, doi: 10.1117/1.JMM.13.1.013002.

[51] S. Grist, J. N. Patel, M. Haq, B. L. Gray, and B. Kaminska, "Effect of surface

treatments/coatings and soft bake profile on surface uniformity and adhesion of SU-8 on a glass substrate," in *Proc.SPIE*, Feb. 2010, vol. 7593, doi: 10.1117/12.842957.

[52] N. Liu, H. Liu, S. Zhu, and H. Giessen, "Stereometamaterials," *Nat. Photonics*, vol. 3, no. 3, pp. 157–162, 2009, doi: 10.1038/nphoton.2009.4.

[53] N. Liu, H. Guo, L. Fu, S. Kaiser, H. Schweizer, and H. Giessen, "Three-dimensional photonic metamaterials at optical frequencies," *Nat. Mater.*, vol. 7, no. 1, pp. 31–37, 2008, doi: 10.1038/nmat2072.

[54] N. Liu, L. Langguth, T. Weiss, J. Kästel, M. Fleischhauer, T. Pfau, and H. Giessen, "Plasmonic analogue of electromagnetically induced transparency at the Drude damping limit," *Nat. Mater.*, vol. 8, no. 9, pp. 758–762, 2009, doi: 10.1038/nmat2495.

[55] A. Tittl, H. Giessen, and N. Liu, "Plasmonic gas and chemical sensing," *Nanophotonics*, vol. 3, no. 3, pp. 157–180, 2014, doi: https://doi.org/10.1515/nanoph-2014-0002.

[56] M. Li, S. K. Cushing, and N. Wu, "Plasmon-enhanced optical sensors: a review," *Analyst*, vol. 140, no. 2, pp. 386–406, 2015, doi: 10.1039/C4AN01079E.

[57] K. M. Mayer and J. H. Hafner, "Localized Surface Plasmon Resonance Sensors," *Chem. Rev.*, vol. 111, no. 6, pp. 3828–3857, Jun. 2011, doi: 10.1021/cr100313v.

[58] K. A. Willets and R. P. Van Duyne, "Localized Surface Plasmon Resonance Spectroscopy and Sensing," *Annu. Rev. Phys. Chem.*, vol. 58, no. 1, pp. 267–297, Apr. 2007, doi: 10.1146/annurev.physchem.58.032806.104607.

[59] J. N. Anker, W. P. Hall, O. Lyandres, N. C. Shah, J. Zhao, and R. P. Van Duyne, "Biosensing with plasmonic nanosensors," *Nat. Mater.*, vol. 7, no. 6, pp. 442–453, 2008, doi: 10.1038/nmat2162.

[60] O. Tokel, F. Inci, and U. Demirci, "Advances in Plasmonic Technologies for Point of Care Applications," *Chem. Rev.*, vol. 114, no. 11, pp. 5728–5752, Jun. 2014, doi: 10.1021/cr4000623.

[61] A. Cetin, A. Coskun, B. Galarreta, M. Huang, D. Herman, A. Ozcan, and H. Altug, "Handheld high-throughput plasmonic biosensor using computational on-chip imaging," *Light Sci. Appl.*, vol. 3, no. 1, pp. e122–e122, 2014, doi: 10.1038/lsa.2014.3.

[62] H. K. Hunt and A. M. Armani, "Label-free biological and chemical sensors," *Nanoscale*, vol. 2, no. 9, pp. 1544–1559, 2010, doi: 10.1039/C0NR00201A.

[63] J. S. Daniels and N. Pourmand, "Label-Free Impedance Biosensors: Opportunities and Challenges," *Electroanalysis*, vol. 19, no. 12, pp. 1239–1257, May 2007, doi: 10.1002/elan.200603855.

[64] A. Syahir, K. Usui, K.-Y. Tomizaki, K. Kajikawa, and H. Mihara, "Label and Label-Free Detection Techniques for Protein Microarrays," *Microarrays (Basel, Switzerland)*, vol. 4, no. 2, pp. 228–244, Apr. 2015, doi: 10.3390/microarrays4020228.

[65] M.-C. Estevez, M. A. Otte, B. Sepulveda, and L. M. Lechuga, “Trends and challenges of refractometric nanoplasmonic biosensors: A review,” *Anal. Chim. Acta*, vol. 806, pp. 55–73, 2014, doi: https://doi.org/10.1016/j.aca.2013.10.048.

[66] Y. Lee, S.-J. Kim, H. Park, and B. Lee, “Metamaterials and Metasurfaces for Sensor Applications,” *Sensors (Basel).*, vol. 17, no. 8, p. 1726, Jul. 2017, doi: 10.3390/s17081726.

[67] F. Neubrech, C. Huck, K. Weber, A. Pucci, and H. Giessen, “Surface-Enhanced Infrared Spectroscopy Using Resonant Nanoantennas,” *Chem. Rev.*, vol. 117, no. 7, pp. 5110–5145, Apr. 2017, doi: 10.1021/acs.chemrev.6b00743.

[68] N. Liu, T. Weiss, M. Mesch, L. Langguth, U. Eigenthaler, M. Hirscher, C. Sönnichsen, and H. Giessen, “Planar Metamaterial Analogue of Electromagnetically Induced Transparency for Plasmonic Sensing,” *Nano Lett.*, vol. 10, no. 4, pp. 1103–1107, Apr. 2010, doi: 10.1021/nl902621d.

[69] S. Lal, S. Link, and N. J. Halas, “Nano-optics from sensing to waveguiding,” *Nat. Photonics*, vol. 1, no. 11, pp. 641–648, 2007, doi: 10.1038/nphoton.2007.223.

[70] A. A. Maradudin, I. Simonsen, J. Polanco, and R. M. Fitzgerald, “Rayleigh and Wood anomalies in the diffraction of light from a perfectly conducting reflection grating,” *J. Opt.*, vol. 18, no. 2, p. 24004, Jan. 2016, doi: 10.1088/2040-8978/18/2/024004.

[71] J.-H. Park, A. Kodigala, A. Ndao, and B. Kanté, “Hybridized metamaterial platform for nano-scale sensing,” *Opt. Express*, vol. 25, no. 13, pp. 15590–15598, Jun. 2017, doi: 10.1364/OE.25.015590.

[72] W. D. Heiss, “Phases of wave functions and level repulsion,” *Eur. Phys. J. D - At. Mol. Opt. Plasma Phys.*, vol. 7, no. 1, pp. 1–4, 1999, doi: 10.1007/s100530050339.

[73] M. V Berry, “Physics of Nonhermitian Degeneracies,” *Czechoslov. J. Phys.*, vol. 54, no. 10, pp. 1039–1047, 2004, doi: 10.1023/B:CJOP.0000044002.05657.04.

[74] W. D. Heiss, “Exceptional points of non-Hermitian operators,” *J. Phys. A. Math. Gen.*, vol. 37, no. 6, pp. 2455–2464, Jan. 2004, doi: 10.1088/0305-4470/37/6/034.

[75] H.-Z. Chen, T. Liu, H.-Y. Luan, R.-J. Liu, X.-Y. Wang, X.-F. Zhu, Y.-B. Li, Z.-M. Gu, S.-J. Liang, and H. Gao, “Revealing the missing dimension at an exceptional point,” *Nat. Phys.*, vol. 16, no. 5, pp. 571–578, 2020, doi: 10.1038/s41567-020-0807-y.

[76] H. Hodaei, A. Hassan, S. Wittek, H. Garcia-Gracia, R. El-Ganainy, D. Christodoulides, M. Khajavikhan, “Enhanced sensitivity at higher-order exceptional points,” *Nature*, vol. 548, no. 7666, pp. 187–191, 2017, doi: 10.1038/nature23280.

[77] W. Chen, Ş. Kaya Özdemir, G. Zhao, J. Wiersig, and L. Yang, “Exceptional points enhance sensing in an optical microcavity,” *Nature*, vol. 548, no. 7666, pp. 192–196, 2017, doi: 10.1038/nature23281.

[78] M. P. Hokmabadi, A. Schumer, D. N. Christodoulides, and M. Khajavikhan, “Non-Hermitian ring laser gyroscopes with enhanced Sagnac sensitivity,” *Nature*, vol. 576, no.

7785, pp. 70–74, 2019, doi: 10.1038/s41586-019-1780-4.

[79] Y.-H. Lai, Y.-K. Lu, M.-G. Suh, Z. Yuan, and K. Vahala, “Observation of the exceptional-point-enhanced Sagnac effect,” *Nature*, vol. 576, no. 7785, pp. 65–69, 2019, doi: 10.1038/s41586-019-1777-z.

[80] J. Doppler, A. Mailybaev, J. Böhm, U. Kuhl, A. Girschik, F. Libisch, T. Milburn, P. Rabl, N. Moiseyev, and S. Rotter, “Dynamically encircling an exceptional point for asymmetric mode switching,” *Nature*, vol. 537, no. 7618, pp. 76–79, 2016, doi: 10.1038/nature18605.

[81] J. Yoon, Y. Choi, C. Hahn, G. Kim, S .Song, K.-Y. Yang, J. Lee, Y. Kim, C. Lee, J. Shin, H.-S. Lee, and P. Berini, “Time-asymmetric loop around an exceptional point over the full optical communications band,” *Nature*, vol. 562, no. 7725, pp. 86–90, 2018, doi: 10.1038/s41586-018-0523-2.

[82] C. Wang, X. Jiang, G. Zhao, M. Zhang, C. Hsu, B. Peng, A. Stone, L. Jiang, and L. Yang, “Electromagnetically induced transparency at a chiral exceptional point,” *Nat. Phys.*, vol. 16, no. 3, pp. 334–340, 2020, doi: 10.1038/s41567-019-0746-7.

[83] B. Peng, S. Özdemir, M. Liertzer, W. Chen, J. Kramer, H. Yilmaz, J. Wiersig, S. Rotter, and L. Yang, “Chiral modes and directional lasing at exceptional points,” *Proc. Natl. Acad. Sci.*, vol. 113, no. 25, pp. 6845–6850, 2016, doi: 10.1073/pnas.1603318113.

[84] Peng, Bo, S. Özdemir, F. Lei, F. Monifi, M. Gianfreda, G. Long, S. Fan, F. Nori, C. Bender, and L. Yang, “Parity–time-symmetric whispering-gallery microcavities,” *Nat. Phys.*, vol. 10, no. 5, pp. 394–398, 2014, doi: 10.1038/nphys2927.

[85] H. Zhao, Z. Chen, R. Zhao, and L. Feng, “Exceptional point engineered glass slide for microscopic thermal mapping,” *Nat. Commun.*, vol. 9, no. 1, p. 1764, 2018, doi: 10.1038/s41467-018-04251-3.

[86] Z. Dong, Z. Li, F. Yang, C.-W. Qiu, and J. S. Ho, “Sensitive readout of implantable microsensors using a wireless system locked to an exceptional point,” *Nat. Electron.*, vol. 2, no. 8, pp. 335–342, 2019, doi: 10.1038/s41928-019-0284-4.

[87] L. Feng, R. El-Ganainy, and L. Ge, “Non-Hermitian photonics based on parity–time symmetry,” *Nat. Photonics*, vol. 11, no. 12, pp. 752–762, 2017, doi: 10.1038/s41566-017-0031-1.

[88] R. El-Ganainy, K. G. Makris, M. Khajavikhan, Z. H. Musslimani, S. Rotter, and D. N. Christodoulides, “Non-Hermitian physics and PT symmetry,” *Nat. Phys.*, vol. 14, no. 1, pp. 11–19, 2018, doi: 10.1038/nphys4323.

[89] Ş. K. Özdemir, S. Rotter, F. Nori, and L. Yang, “Parity–time symmetry and exceptional points in photonics,” *Nat. Mater.*, vol. 18, no. 8, pp. 783–798, 2019, doi: 10.1038/s41563-019-0304-9.

[90] M.-A. Miri and A. Alù, “Exceptional points in optics and photonics,” *Science (80-.).*, vol. 363, no. 6422, 2019, doi: 10.1126/science.aar7709.

[91] M. L. Brongersma and V. M. Shalaev, “The Case for Plasmonics,” *Science (80-.).*, vol. 328, no. 5977, pp. 440–441, 2010, doi: 10.1126/science.1186905.

[92] H. Alaeian and J. A. Dionne, “Parity-time-symmetric plasmonic metamaterials,” *Phys. Rev. A*, vol. 89, no. 3, p. 33829, Mar. 2014, doi: 10.1103/PhysRevA.89.033829.

[93] A. Kodigala, T. Lepetit, and B. Kanté, “Exceptional points in three-dimensional plasmonic nanostructures,” *Phys. Rev. B*, vol. 94, no. 20, pp. 1–5, 2016, doi: 10.1103/PhysRevB.94.201103.

[94] B. Gustavsen, “Improving the pole relocating properties of vector fitting,” *IEEE Trans. Power Deliv.*, vol. 21, no. 3, pp. 1587–1592, Jul. 2006, doi: 10.1109/TPWRD.2005.860281.

[95] B. Gustavsen and A. Semlyen, “Rational approximation of frequency domain responses by vector fitting,” *IEEE Trans. Power Deliv.*, vol. 14, no. 3, pp. 1052–1061, Jul. 1999, doi: 10.1109/61.772353.

[96] S. Y. Elnaggar, R. J. Tervo, and S. M. Mattar, “Energy Coupled Mode Theory for Electromagnetic Resonators,” *IEEE Trans. Microw. Theory Tech.*, vol. 63, no. 7, pp. 2115–2123, Jul. 2015, doi: 10.1109/TMTT.2015.2434377.

[97] I. Awai and Y. Zhang, “Overlap integral calculation of resonator coupling,” in *2006 12th International Symposium on Antenna Technology and Applied Electromagnetics and Canadian Radio Sciences Conference*, Jul. 2006, pp. 1–4.

[98] I. Awai and Y. Zhang, “Separation of Coupling Coefficient Between Resonators into Magnetic and Electric Components Toward Its Application to BPF Development,” in *2008 China-Japan Joint Microwave Conference*, 2008, pp. 61–65, doi: 10.1109/CJMW.2008.4772375.

[99] J. Fuchs, J. Main, H. Cartarius, and G. Wunner, “Harmonic inversion analysis of exceptional points in resonance spectra,” *J. Phys. A Math. Theor.*, vol. 47, no. 12, p. 125304, Mar. 2014, doi: 10.1088/1751-8113/47/12/125304.

[100] D. Meshulach, D. Yelin, and Y. Silberberg, “Real-time spatial--spectral interference measurements of ultrashort optical pulses,” *J. Opt. Soc. Am. B*, vol. 14, no. 8, pp. 2095–2098, Aug. 1997, doi: 10.1364/JOSAB.14.002095.

[101] M. Takeda, H. Ina, and S. Kobayashi, “Fourier-transform method of fringe-pattern analysis for computer-based topography and interferometry,” *J. Opt. Soc. Am.*, vol. 72, no. 1, pp. 156–160, Jan. 1982, doi: 10.1364/JOSA.72.000156.

[102] A. Börzsönyi, A. P. Kovács, M. Görbe, and K. Osvay, “Advances and limitations of phase dispersion measurement by spectrally and spatially resolved interferometry,” *Opt. Commun.*, vol. 281, no. 11, pp. 3051–3061, 2008, doi: https://doi.org/10.1016/j.optcom.2008.02.002.

[103] J. Wiersig, “Prospects and fundamental limits in exceptional point-based sensing,” *Nat. Commun.*, vol. 11, no. 1, p. 2454, 2020, doi: 10.1038/s41467-020-16373-8.

[104] C. Chen, L. Jin, and R.-B. Liu, “Sensitivity of parameter estimation near the exceptional point of a non-Hermitian system,” *New J. Phys.*, vol. 21, no. 8, p. 83002, Aug. 2019, doi: 10.1088/1367-2630/ab32ab.

[105] J. Wiersig, “Sensors operating at exceptional points: General theory,” *Phys. Rev. A*, vol. 93, no. 3, pp. 1–9, 2016, doi: 10.1103/PhysRevA.93.033809.

[106] P. Dremsek, J. Wenzel, R. Johne, M. Ziller, J. Hofmann, M. Groschup, S. Werdermann, U. Mohn, S. Dorn, M. Motz, M. Mertens, W. Jilg, and R. Ulrich, “Seroprevalence study in forestry workers from eastern Germany using novel genotype 3- and rat hepatitis E virus-specific immunoglobulin G ELISAs,” *Med. Microbiol. Immunol.*, vol. 201, no. 2, pp. 189–200, 2012, doi: 10.1007/s00430-011-0221-2.

[107] F. A. Glover and J. D. S. Goulden, “Relationship between Refractive Index and Concentration of Solutions,” *Nature*, vol. 200, no. 4912, pp. 1165–1166, 1963, doi: 10.1038/2001165a0.

[108] A. E. Cetin, D. Etezadi, B. C. Galarreta, M. P. Busson, Y. Eksioglu, and H. Altug, “Plasmonic Nanohole Arrays on a Robust Hybrid Substrate for Highly Sensitive Label-Free Biosensing,” *ACS Photonics*, vol. 2, no. 8, pp. 1167–1174, Aug. 2015, doi: 10.1021/acsphotonics.5b00242.

[109] K. Sreekanth, Y. Alapan, M. Elkabbash, E. Ilker, M. Hinczewski, U. Gurkan, A. De Luca, and G. Strangi, “Extreme sensitivity biosensing platform based on hyperbolic metamaterials,” *Nat. Mater.*, vol. 15, no. 6, pp. 621–627, 2016, doi: 10.1038/nmat4609.

[110] M. Hentschel, M. Schäferling, X. Duan, H. Giessen, and N. Liu, “Chiral plasmonics,” *Sci. Adv.*, vol. 3, no. 5, 2017, doi: 10.1126/sciadv.1602735.

[111] W. Du, X. Wen, D. Gérard, C.-W. Qiu, and Q. Xiong, “Chiral plasmonics and enhanced chiral light-matter interactions,” *Sci. China Physics, Mech. Astron.*, vol. 63, no. 4, p. 244201, 2019, doi: 10.1007/s11433-019-1436-4.